Investigation of spin polarization-shifts in electron beams produced by GaAs-based photocathodes under different surface activation conditions

Dissertation submitted for the award of the title „Doctor of Natural Sciences“ to the Faculty of Physics, Mathematics and Computer Science of the Johannes Gutenberg-University Mainz

Jennifer Trieb
born in Berlin

Mainz, 11th March, 2025

JOHANNES GUTENBERG
UNIVERSITÄT MAINZ

Supervisor:

Date of defense: 19.02.2025

La vie n'est facile pour aucun de nous. Mais quoi, il faut avoir de la persévérance, et surtout de la confiance en soi. Il faut croire que l'on est doué pour quelque chose, et que, cette chose, il faut l'atteindre coûte que coûte.

(E. Curie, Madame Curie : A Biography *(Bermann-Fischer, 1937))*

Zusammenfassung

Diese Arbeit untersucht die Mechanismen, die die Elektronenspinpolarisation (ESP) von photoemittierten Elektronenstrahlen aus GaAs Photokathoden im Rahmen von Experimenten mit spinpolarisierten Elektronenstrahlen beeinflussen. Ziel ist es, die Beziehung zwischen Polarisation und Quanteneffizienz (QE) zu analysieren. Diese Erkenntnisse sind besonders relevant für hochpräzise Experimente zur Paritätsverletzung wie das P2 Experiment an der Mainzer Energierückgewinnenden Supraleitenden BeschleunigerAnlage (MESA), bei dem longitudinal polarisierte Elektronenstrahlen für die Untersuchung fundamentaler Wechselwirkungen von entscheidender Bedeutung sind.

Die Emission spinpolarisierter Elektronen aus GaAs Photokathoden wird durch intrinsische Faktoren wie Kristalldotierung und Depolarisationsmechanismen beeinflusst. Die Oberflächenvorbereitung von Halbleitern wie GaAs mit Submonoschichten aus Cäsium und einem Oxidationsmittel induziert eine negative Elektronenaffinität (NEA), wodurch die Wahrscheinlichkeit des Elektronenaustritts erhöht wird. Diese Arbeit untersucht und modelliert die Polarisationsentwicklung in Bezug auf die Austrittswahrscheinlichkeit. Die experimentellen Daten wurden mithilfe eines Aufbaus gesammelt, der eine präzise Messung der Polarisationsänderungen gewährleisten soll. Ein longitudinal polarisierter Elektronenstrahl bei 100 keV wurde von einer bulk GaAs Photokathode sowie einer Übergitter-Photokathode erzeugt, die eine höhere Polarisation als die bulk Kathode bietet.

Die Diskussion behandelt die im Halbleiter vorherrschenden Depolarisationsmechanismen, insbesondere den Bir-Aronov-Pikus- (BAP) und D'yakonov-Perel- (DP) Mechanismus. Es wurde festgestellt, dass bei signifikant niedriger QE der depolarisierende Effekt von DP zu verschwinden scheint, womit eine Stabilisierung der Polarisation erreicht wird. Es wird angenommen, dass Einfangzustände in der Bandbiegezone keine Elektronen mehr emittieren können, wenn die QE niedrig genug ist.

Diese Arbeit zielt darauf ab, das Polarisationsverhalten in Experimenten mit spinpolarisierten Elektronenstrahlen zu verstehen und dabei die Rolle der Einfangzustände in der Bandbiegungszone aufzuzeigen. Die Erkenntnisse liefern einen Rahmen für die kommenden hochpräzisen, paritätsverletzenden Experimente von MESA.

Abstract

This thesis explores the mechanisms influencing the electron spin polarization (ESP) of photo emitted electron beams from GaAs photocathodes in the context of spin-polarized electron beam experiments. The aim is to analyze the relationship between the polarization and quantum efficiency (QE). These findings hold particular relevance for high-precision parity-violation experiments such as the P2 experiment at the new Mainz Energy-recovering Superconducting Accelerator (MESA). Therefore longitudinally polarized electron beams are essential for probing fundamental interactions.

The emission of spin-polarized electrons from GaAs photocathodes is influenced by intrinsic factors, such as doping of the GaAs crystal and depolarizing mechanisms. To extract the electrons from the crystal, the surface preparation of semiconductors like GaAs with sub-mono layers of caesium and an oxidizing agent induces a negative electron affinity (NEA), enhancing electron escape probability. This thesis examines and models the polarization evolution in respect to escape probability. Experimental data were collected using a setup designed to ensure precise measurement of the polarization changes. A longitudinally polarized electron beam at 100 keV was generated from bulk GaAs photocathode as well as a superlattice photocathode which provides higher polarization as the bulk cathode.

The discussion explores the depolarizing mechanisms that dominate within the semiconductor, particular the Bir-Aronov-Pikus (BAP) and D'yakonov-Perel (DP) mechanisms. It was found that for low QE the depolarizing effect of DP seems to vanish as a stabilization of the polarization is reached. It is hypothesized that trapping states in the band bending zone cannot emit electrons anymore if the QE is low enough.

In conclusion, this thesis aims to understand the polarization behavior in spin polarized electron beam experiments, emphasizing the role of trapping states in the band bending zone which are sensitive to changes in the QE. The findings provide a framework for the upcoming high-precision parity-violating experiments of MESA.

Contents

List of Figures

Chapter 1

Introduction

1.1. Background and motivation

With the advent of quantum mechanics in the early 1920s and subsequent experiments by Stern and Gerlach, the concept of electron spin was introduced [2]. The utilization of polarized electron beams has become particularly significant in parity-violating experiments, aimed at uncovering physics beyond the Standard Model of Particle Physics [3].

The new Mainz Energy-recovering Superconducting Accelerator (MESA) at the Johannes Gutenberg-University is designed for high-precision experiments, utilizing state-of-the-art energy recovery linear (ERL) accelerator technology with superconducting acceleration sections, called MEEC (MESA Enhanced Elbe Cryomodule) [4]. The layout is shown in fig. 1.1.

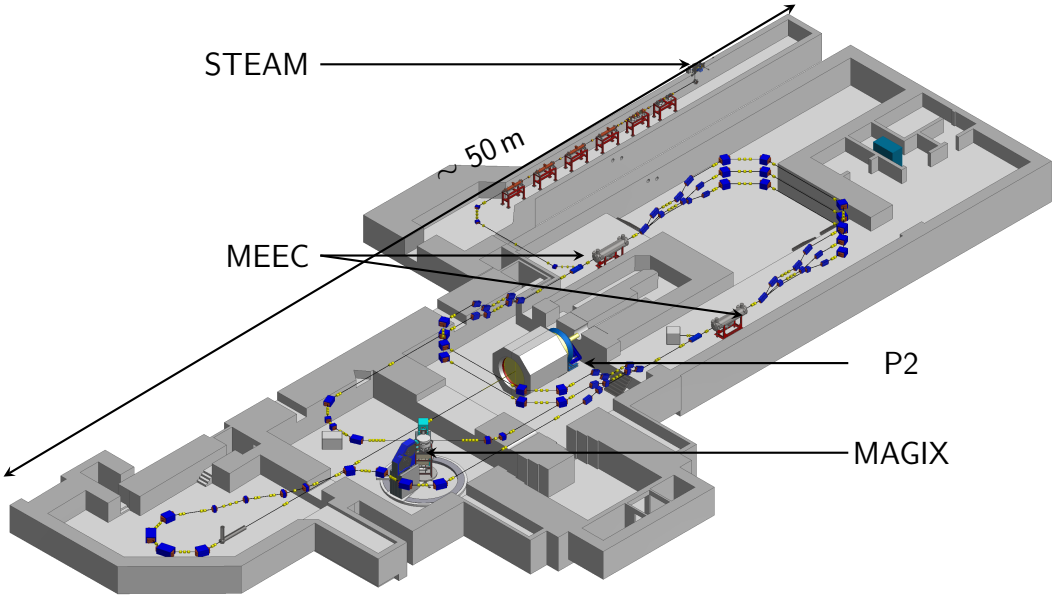

Figure 1.1.: *Layout of the accelerator MESA. The source STEAM and the low energy beam line are separated from the energy recovering linac ring. The blue dots and rectangle represent bending magnets which define the electron beam path. The experiments P2 and MAGIX are indicated as well as the superconducting accelerator sections MEEC.*

MESA will operate in two different modes: the energy recovery mode (ERL) and the external beam mode (EB) [5]. In EB mode, MESA works like a conventional linear accelerator (LINAC) after recirculating, with the electron beam being dumped after the P2 experiment. Recirculation is achieved if the orbit length of the electron beam path is a full integer of the radio frequency used for acceleration [6]. For the ERL mode this is only the half integer since the electrons need to experience the decelerating field [7].

Due to the low energy of 105 MeV used for the Mainz Gas Injection Target Experiment (MAGIX) in combination with a thin target the electron beam will still fit within the acceptance of the accelerator [5]. At low beam energies the scattering rates of the electrons places outside of the acceptance scale with $1/E^2$ but the low interactions with the thin targets compensate that effect. Therefore, after the interaction with the experiment, the beam is collected by quadrupole lenses and directed back into the accelerator with a phase shift of 180°. With such a phase shift the electron beam after the interaction experience a decelerating field within the acceleration section. The energy from the electron beam is transferred into the cavities of the section and can be used to accelerate other electron bunches, which need to gain in energy [7]. Therefore, significantly higher intensities can be achieved in the internal experiment. Switching between the two modes makes MESA a versatile machine that can be used for a wide variety of experiments.

Key features of MESA include high luminosity and polarized electron beams, leveraging decades of expertise in polarized electron beams at the institute, which is crucial for the success of the P2 experiment [3].

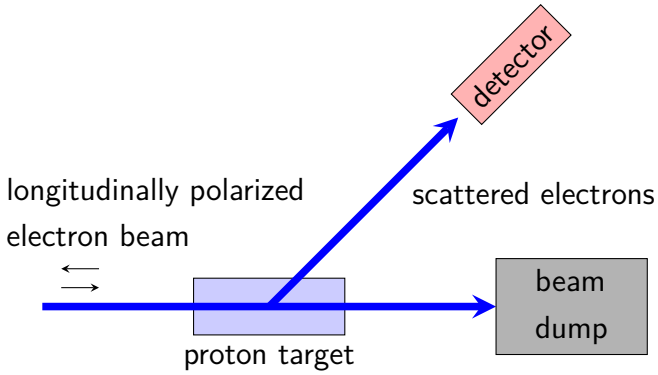

Figure 1.2.: *The measuring principle of P2 is displayed: a longitudinally polarized electron beam interacts with a proton target. The scattered electrons will be measured by a detector while the non scattered electrons are transported into a beam dump.*

P2 aims to measure the weak mixing angle ($\sin^2(\theta_w)$) with a precision of 0.15 % [3]. This

will involve parity-violating electron scattering at a hydrogen target to provide an important test of the Standard Model. A schematic of the experiment is shown in fig. 1.2 where a longitudinal polarized electron beam collides with a proton target. The scattered electrons hit a detector that can measure asymmetries that occur when an interaction has a preferred direction. The measured asymmetries are proportional to the polarization degree according to eq. (1.1)[5]:

$$A_{PV,exp} = C \cdot P_{long} \cdot (1 - 4\sin^2(\theta_w)) \tag{1.1}$$

where

$A_{PV,exp}$: experimental measured, parity violating asymmetry
C : summarized constants
P_{long} : longitudinal polarization
θ_w : Weinberg angle.

This shows that the polarization degree of the electron beam, or electron spin polarisation (ESP), needs close monitoring, especially if the polarization drifts. The measured asymmetries in P2 are in the case of longitudinal ESP parity violating because the weak force couples to the left-handed particles but not to the right-handed ones [8, 9]. An observation of an asymmetry in elastic scattering is in agreement with parity conservation only if a spin component vertical to the scattering plane is involved.

The weak mixing angle helps understand the interaction between the electromagnetic force and the weak force in the realm of subatomic particles. Parity-violating experiments have shown that the weak force does not obey parity conservation, and measuring the strength of this violation provides clues to possible new physics.

P2 uses the full capability of photocathodes delivering a spin polarized electron beam up to 85 % of polarization with the full energy of MESA of 155 MeV. This study reveals that asymmetry, and thus polarization, will significantly change during long-term operation with high current extraction. The investigation explores the sources of these changes and how to describe them in a model for further evaluation.

The goal is to develop a model that not only explains these changes but also serves as a cornerstone for optimizing experiments, including the P2 experiment conducted with MESA. This research not only fills a critical gap in current knowledge but also lays the groundwork for advancements in accelerator technologies with tangible applications in experimental physics

Chapter 2

Theoretical Framework

Spin polarized electrons are a main requirement for the P2 experiment in order to provide the demanded precision for the measurement of the Weinberg angle. In this chapter the basics for electron spin polarization (ESP) and electron emission from gallium arsenide (GaAs) is explained, followed by a fundamental description of Mott polarimetry. An explanation of potential depolarizing effects within the crystal, such as the Bir-Aronov-Pikus (BAP) or D'yakonov-Perel (DP) mechanisms, is provided, along with a discussion of unresolved questions and areas of uncertainty related to spin polarization in this work.

2.1. The theoretical foundations for electron spin polarization

Conservation laws in quantum physics dictate that intrinsic angular momentum must be a basic characteristic of elementary particles [10]. This conserved angular momentum called spin, along with mass and charge, is a fundamental property that serves as a defining characteristic for particles in the standard model [11, 12]. For electrons the spin is $\frac{1}{2}$ in units of Planck´s reduced constant ($\hbar$) and thus makes it a fermion [13, p.228]. Those particles obey Pauli's exclusion principle in atoms and molecules, preventing that even two electrons have the exact same quantum numbers [13, p.230].

To find a better description of the electronic properties of solids some assumptions are needed: (a) the periodicity is not broken and (b) the solutions of Schrödinger´s equation are translational invariant. Investigating the one dimensional atomic chain the tight binding model finds a solution for the Schrödinger equation by a Fourier transformation into the reciprocal space or $\vec{k}$ space [14, p.102]. The periodicity, or repeatability of a set of atoms, leads to the usage of Bloch function in the $\vec{k}$ space, which are periodic solutions to the Schrödinger equation and will result in a dispersion relation $E(k)$. This dispersion relation give a band, a range of energy eigenstates for electrons.

These bands are filled up with electrons starting with the band with the lowest energy. The energetically highest band, which is occupied is called valance band and the lowest unoccupied band is called conduction band [14, p.174]. With the energy difference between these two bands, solids can be sorted into three categories: insulators, semiconductors and metals. In this work the focus will be on semiconductors since the used material for electron emission is based on the III-V semiconductor GaAs, whose crystal structure along with its first Brillouin zone is shown in fig. 2.1. From that reciprocal representation a dispersion relation can be calculated which in turn will provide the band structure of the GaAs crystal.

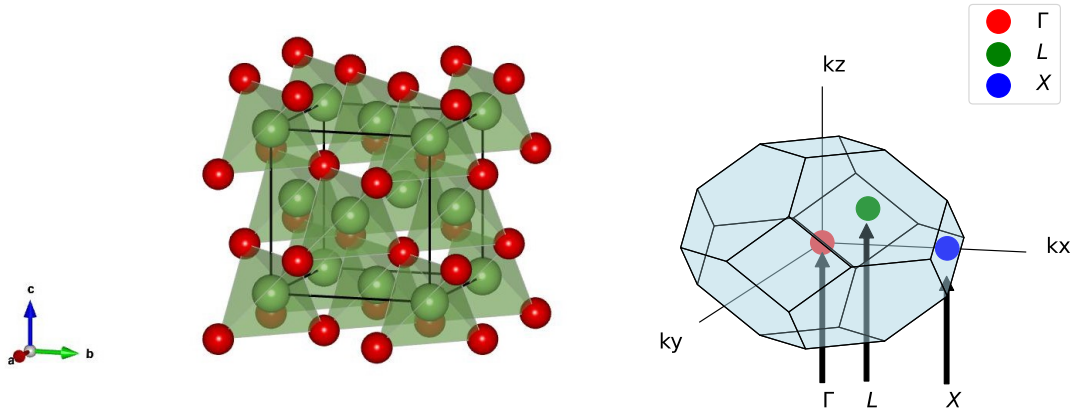

Figure 2.1.: *Gallium (Ga, green balls) and arsenic (As, red balls) forming the crystal structure of zinc blende-type. Here the Ga atoms fill in the tetrahedral sites and vice versa for As which are cubic-closed packed [15]. Next to the real space picture of the crystal structure the first Brillouin zone, the Wigner-Seitz cell of the reciprocal space is shown along with the symmetry points* Γ, L *and* X*.*

In the realm of semiconductors, the interaction between the intrinsic spin of electrons and their orbital motion plays a crucial role, known as spin-orbit coupling. This interaction arises because, in the electron's frame of reference, its motion through the electric field of the nucleus creates a magnetic field, which then interacts with the electron's spin [13, p.58]. In GaAs this interaction leads to the splitting of the valence band, creating distinct light and heavy hole bands due to the different angular momenta associated with the electron's spin and motion as seen in fig. 2.2.

The particular band structure of GaAs in between the L and X points is shown, contains the minimum of the conduction band and the maximum of the valence band at the Γ point. Both are separated by an energy band gap (E_{Gap}) of 1.42 eV [16] at 300 K. This point is the point of highest symmetry in the GaAs crystal structure. To the left of the Γ point the L point and to the right the X point can be found. There are possibilities that exited

electrons can be scattered into those valleys of the conduction band but these processes are not considered in the scope of this work [17]. The main reason for that is the larger energy required (1.7 eV for the L and 1.9 eV for the X minimum), while the photon energy in this work used is between 1.5 eV to 1.6 eV.

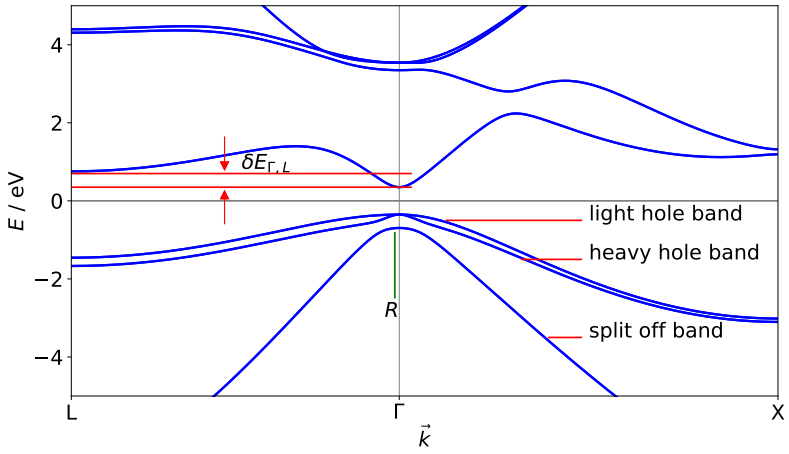

Figure 2.2.: *The calculated band structure of GaAs with spin-orbit coupling centered around the Γ point of symmetry [18, 19]. The valence band is forming a maximum there whereas the conduction band is presenting a minimum at this point thus making GaAs a direct band gap semiconductor. The energy E is given and the wave vector $\vec{k}$ with the points of symmetry L, Γ and X. The most important band features of the valence band level are labeled. The radius R is indicated too, as one can approximate the effective electron mass from that.*

The maximum of the valence band and the minimum of the conduction band can be approximated with a parabolic function, if assumed the solid is isotropic (i.e. uniform in space), with respect to the wave vector $\vec{k}$ and the energy at a point of the $\vec{k}$ in units of $\hbar$ according to eq. (2.1) [20, p.23]:

$$E(\vec{k}) = E_0 + \frac{\hbar^2 \vec{k}^2}{2m^*}. \tag{2.1}$$

The symbol m^* represents an effective mass of the electrons that seems to appear if they are interacting with forces in the lattice. The effective mass can be approximated by the radius R as indicated in fig. 2.2 as $m^* \propto \frac{1}{R}$.

2.1.1. Generation of polarized electrons

The solid state material cannot have an inversion center in order to break the symmetry of the wave function and be used to produce a polarized electron beam. In GaAs this is

the case at the point of highest symmetry, the gamma point (Γ). Since GaAs is a direct semiconductor electrons can be exited from the valence band into the conduction band with photon-electron interaction [14, p.180]. It is important to note that after photon absorption, the ESP aligns longitudinally along the light propagation direction, due to the conservation of angular momentum. The source generates a polarization vector from the photocathode that is initially oriented longitudinally. The ESP must be rotated into a transverse configuration in order to measure asymmetries because the asymmetries are sufficiently large in that orientation to be measured quickly and precisely [8, p.53]. As a result of spin-orbit coupling, the valence band experiences a splitting, resulting in a distinction between light and heavy hole bands and the split-off band.

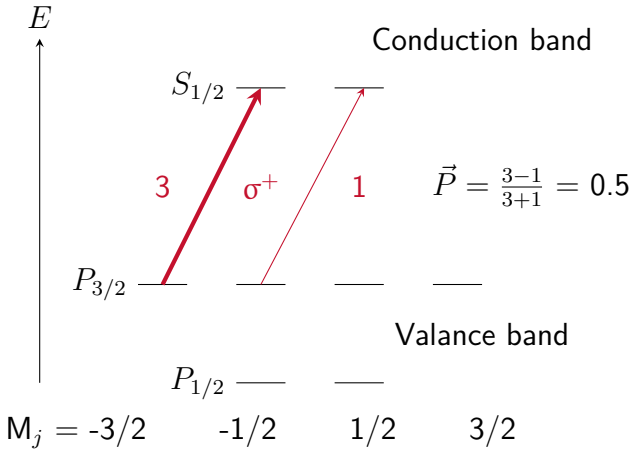

Figure 2.3.: *Absorption of circular polarised light (denoted as σ^+ for right handed) and the excitation of electrons from valence band into the conduction band. The transition probability from the $P_{3/2}$ into the $S_{1/2}$ state is about three times higher than the other transitions [21, 22]. Since the band gap of GaAs is 1.42 eV at room temperature the usage of infrared light is most suitable for the electron excitation [23].*

The helicity-bearing photons can transfer their angular momentum to the interacting electron. The quantum mechanical transition rules dictate that electrons can only transition to the conduction band in integral multiples of the angular momentum [13, p.124]. Additionally, the transition probability from the $P_{3/2}$ into the $S_{1/2}$ is three times higher than the other indicated transition in fig. 2.3. Therefore the theoretical maximum polarization is according to the quantum mechanical calculations 50 % [24]. By controlling the helicity of the photons it is possible to switch between the two states of electron spin of plus or minus one half.

Since in this work the used laser wavelength is 808 nm the excitation of the electrons is higher than the band gap. The energy of the photons is 1.53 eV while at 300 K the band

gap of GaAs is 1.42 eV, which provides an excess of energy for the excitation process of 110 meV. Therefore it is to be noted that thermalization processes will take place and those electrons which do not thermalize in the lattice will play a more important role if the quantum efficiency is low (refer to eq. (2.2) and section 2.2).

In this work two different cathode types have been examined: the bulk GaAs cathodes which have been experimentally characterized in certain parameters by us [25]. In those cathodes thermalization effects can play a role since the photon energy is about 110 meV larger than the band gap. The superlattice cathode discussed in the next section are not as much influenced by thermalization effects as the measurements are at the edge of the band gap.

2.1.2. Generation of high polarization

The symmetry breaking at the gamma point provides a foundation for achieving this polarization. In order to maximize the ESP the degeneracy of the $P_{3/2}$ needs to be broken down. The epitaxial growth of semiconductor materials with different lattice constants was a promising path [26]. In such strained lattice GaAs semiconductors, the crystal lattice is grown epitaxially on GaAsP, impacting the electronic band structure and therefore reach polarization degrees between 50 % to 80 % [27]. The main change of the structure is shown in fig. 2.4. The lifting of the degeneracy on the $P_{3/2}$ and $P_{1/2}$ is responsible for the higher polarization.

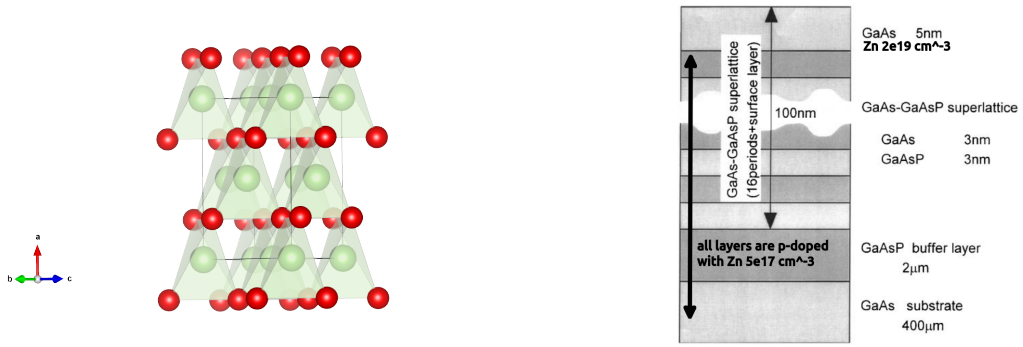

Figure 2.4.: *The main features of strained lattice variants of GaAs are shown in the left and superlattice variant is shown on the right. The strain is build by epitaxially growing the GaAs crystal with different lattice constants, thus deforming the original structure. For reference see fig. 2.1 for the unstrained crystal. The exemplary image of a superlattice shown has an active zone composed of GaAs (dark gray stripes) and GaAsP (lighter gray stripes). Left figure made with [15] and right figure taken from [28]. It is important to note that the surface layer has the same doping concentration as the bulk cathodes.*

It is worth mentioning that the doping concentration of the bulk cathode used in this work and the superlattices cathodes in their surface layer have the same doping concentration of $10^{19}\,\mathrm{cm}^{-3}$.

Even higher polarization can be achieves by GaAs bases superlattice cathodes. These have been developed in 2004 in a cooperation between the Stanford linear accelerator center (SLAC) and a semiconductor company and are widely used in electron accelerators also at Mainz Microtron (MAMI) [29]. The important parameters quantum efficiency (QE) and ESP as a function of photon energy are shown in fig. 2.5 on the right. Band structures of such GaAs based hetereostructures are strictly dependent of the directionality. The used superlattice structures are two dimensional and an exemplary band structure is shown in fig. 2.5. The main feature is the development of minibands or subbands which correspond to the layers within the structure [20].

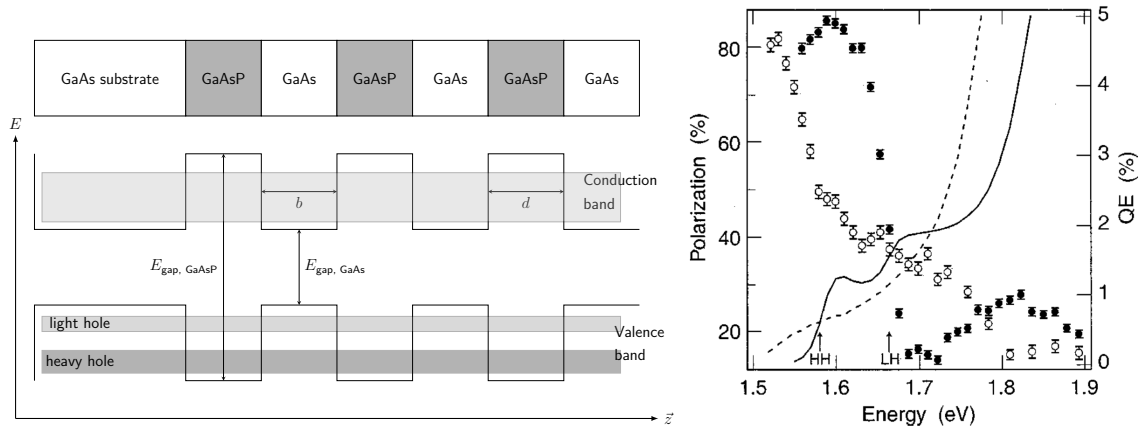

Figure 2.5.: *Schematic band structure of a superlattice with the mini band formation on the left according to [30, p.1023-1024] and on the right is the polarization and quantum efficiency (QE) (both solid circles/ lines) plotted versus the excitation energy from a GaAs/$GaAs_{1-x}P_x$ superlattice structure from [29]. On the left the different band gap energies are given for each layer and their respective thicknesses b and d are influencing the thickness of the wells formed. The band gap of $GaAs_{0.7}P_{0.3}$ as main used material for photocathodes is between 1.5 eV to 1.7 eV [31], while the GaAs has a band gap of 1.4 eV.*

Similarly, superlattice structures of GaAs, composed of alternating layers of different materials like GaAsP, enhance the polarization beyond 80 % with QE as high as 1 % [29]. Such cathodes, especially those used in the MAMI are relevant to this work, present intriguing possibilities for achieving high polarization levels [32].

Quantum efficiency

Although fig. 2.5 implies that a QE close to zero should be anticipated at a photon energy of 1.53 eV, the operation has proven to be successful. In this work it could be shown that the superlattice wafer produced a QE of 0.07 % at 808 nm and a QE of 0.21 % at 785 nm (1.58 eV). The measurement of the QE in fig. 2.5 did not include any correction for surface and window reflections and therefore define the quantum efficiency as described in eq. (2.2) [33] as does this work. A reason to the factor three lower measured QE in this work than in the referenced samples (QE $\approx$ 0.6 %) can be attributed to slight differences in the exact lattice structure of the cathode material. As seen in [29] the QE is sensitive to the quantum well thickness, number of periods in the superlattice and on the phosphorus fraction. The in fig. 2.5 right described wafer is not the exact same wafer used in this work, this factor of three in QE can be explained by the above mentioned differences.

Band tailing provides electronic states within the band gap which in turn will cause a smudging of the absorption edges. This leads to quantum efficiencies even if the photon energy is not sufficient [34]. Additionally high doping concentrations cause a shrinking in the band gap, which is in the order of 100 meV for doping concentrations of $10^{19}\,\mathrm{cm}^{-3}$ [35].

But those cathodes tend to have lower quantum efficiency (QE), i.e. the quotient of emitted electrons (N_e) and incident photons (N_p) as shown in eq. (2.2), then bulk cathodes.

$$QE = \frac{N_e}{N_p} \tag{2.2}$$

It is known the QE can be in the order of 20 % [36] while the MAMI accelerator application the 1 % is just enough. The stark difference is probably due to the specific GaAs wafers used: it is believed that epitaxial grown wafers have higher crystal qualities and therefore provide more QE as non-epitaxial grown wafers [36].

The QE is a measure to evaluate the performance of a photocathode besides the polarization. As photocathodes there are metal photocathodes known with QE in the region of 10^{-4} % to 10^{-1} % while semiconductor photocathodes like GaAs cathodes reach between 1 % to 10 % in quantum efficiency [37]. The QE is heavily dependent on the surface since the manipulation towards negative electron affinity as described in section 2.2 is very sensitive to disturbances. Spicer and Herrera-Gomez developed in 1993 a model based on Spicer's three step model of photo emission (refer to section 2.2). They derived the quantum efficiency as

a function of the absorption coefficient α, the electron diffusion length l, the reflectivity R and the escape probability P_{esc} in eq. (2.3):

$$QE(h\nu) = \left(\frac{1}{1+\frac{1}{\alpha l}}\right) \cdot (1-R) P_{\text{esc}} \tag{2.3}$$

where all parameters are functions of the photon energy $h\nu$. The reflectivity was taken from literature [39] as 0.324 and assumed to be equal for both cathode materials as the top most layer is heavy p-doped GaAs in both cases. The electron diffusion length l can be calculated with the square root of the product of the diffusion constant D (see eq. (2.4)) and the recombination time τ_{rec}. The diffusion constant is heavily dependent on the doping concentration of the semiconductor and varies from the used bulk GaAs to the superlattice GaAs with a factor of 2 to 3 following Einsteins relation of semiconductors [40]. Therefore the electron diffusion length for the bulk material is in the order of 400 nm while the situation in the superlattice material is a bit more complex.

The superlattice materials are typically designed in a way that the contribution of polarisation losses due to diffusion of the electrons is as low as reasonable possible. Therefore for calculation of the escape probability of the superlattice GaAs the electron diffusion length was fixed at 100 nm and is four times smaller than the diffusion length of bulk GaAs. Also the recombination time of the superlattices is in the region of 40 ns [41], due to the doping concentration being two orders of magnitude smaller in superlattice. These differences in electron diffusion length are main difference in the description in terms of escape probability (P_{esc}).

The main contributor to systematic uncertainty of the escape probability (P_{esc}) is the measurement of the absorption coefficient $\alpha = (20\,501 \pm 7456)\,\text{cm}^{-1}$ from [25], which is in reasonable magnitude as reported in [41]. The error is about 30 % as given by [25]. For bulk cathodes there are dedicated measurements that reveal the diffusion length by using the values found in the same work for the recombination time τ_{rec} as (160.3 ± 144.1) ps and as diffusion constant $D = (13.6 \pm 9.9)\,\text{cm}^2\,\text{s}^{-1}$. The measured value of D is in reason with from literature estimated values [20]. With that and eq. (2.4) the diffusion length (l) of electrons in the bulk material can be calculated to:

$$l = \sqrt{D \cdot \tau_{\text{rec}}} = (466 \pm 90)\,\text{nm}. \tag{2.4}$$

These measurements for the bulk cathodes are from the same cathode type; the bulk cathode of [25] and the bulk cathode in this work used are both from Wafer Technology Ltd. [42].

For the superlattice material only estimates from literature regarding the diffusion constant and the recombination time can be incorporated into the analysis. These estimates, in lack of experimental data, solely base on the difference in doping concentration will lead to a recombination time of around 40 ns [41] and a diffusion constant of 7.7 $cm^2\,s^{-1}$ [40]. This will lead to an estimated electron diffusion length of roughly 5.5 µm, which is a factor ten longer than in the higher doped bulk GaAs. But the superlattice cathodes active zone is only 100 nm thick, so that confines the electron diffusion length.

Using the values discussed above and rearrangement of eq. (2.3) to solve for the P_{esc} will result in the formula as used in eq. (6.3). The P_{esc} will be in the same magnitude as the QE which is in agreement to Spicer's derivation [38].

2.2. The working principle of a photocathode using the negative electron affinity property

Spicer described in 1958 his tree step model of photo emission from photocathodes [43]. In fig. 2.6 the model is illustrated.

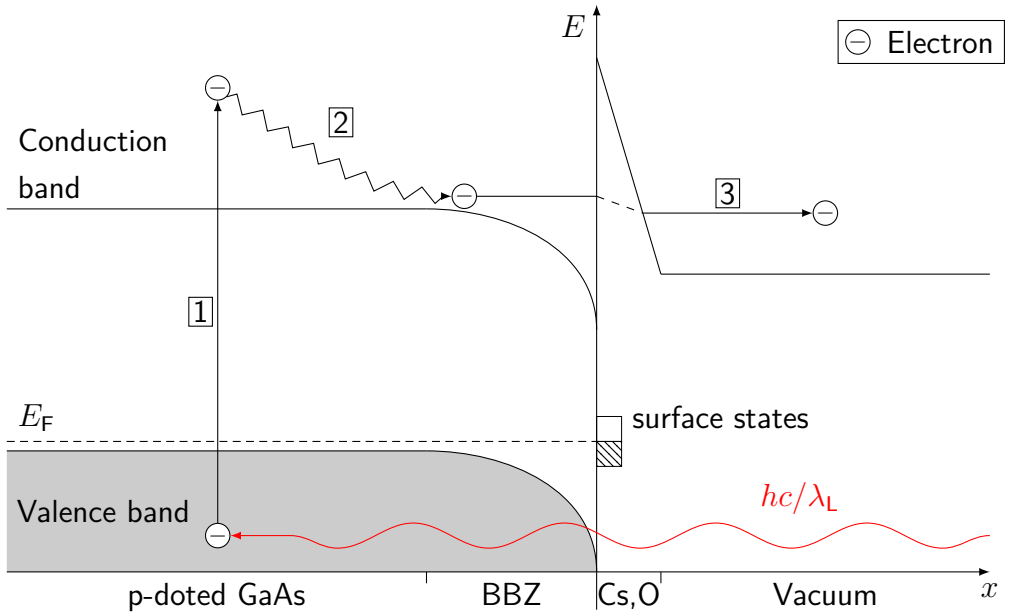

Figure 2.6.: *Spicers three step model is visualised here. The emission from the p-doted semiconductor material through the band bending zone (BBZ) into the vacuum is explained in the text. The numbers represent the steps in order: (1) photo excitation, (2) thermalization and diffusion and (3) tunneling through the potential barrier of the surface. Taken from [44].*

The first step is the excitation of the electron from the valence band into the conduction band due to the incident photon. For the materials used in this work, the selection rules lead to spin polarized electrons as discussed in section 2.1.1. Secondly, the excited electron now travels through the semiconductor to the surface. During this time the electron magnetic moment and the electron charge can interact with the crystal lattice in different ways, thermalization and ESP losses are occurring. The final step regards to the emission that provides the accelerator with the required electron beam.

Electrons cannot be extracted easily out of a semiconductor surface. The way to go is to lower the work function with caesium and an oxidizing agent. Examining the states of the semiconductor energy levels in bulk-GaAs help to understand how lowering the work function facilitate the extraction of electrons. The detailed explanation of the band structure is already given in section 2.1.

The energy needed to excite an electron from the conduction band into the vacuum energy level (E_{vac}) is called the electron affinity χ. In the bulk of a semiconductor the electron affinity is always positive for GaAs, therefore they will not cross the surface without being given the extra energy χ. The difference in the energy level of the vacuum and the conduction band defines the electron affinity, as seen in eq. (2.5). This state is called positive electron affinity and visible in the solid state side of the fig. 2.7.

$$\chi = E_{\text{vac}} - E_{\text{CB}} \tag{2.5}$$

with:

χ : electron affinity
E_{vac} : energy level of the vacuum
E_{CB} : energy level of the conduction band

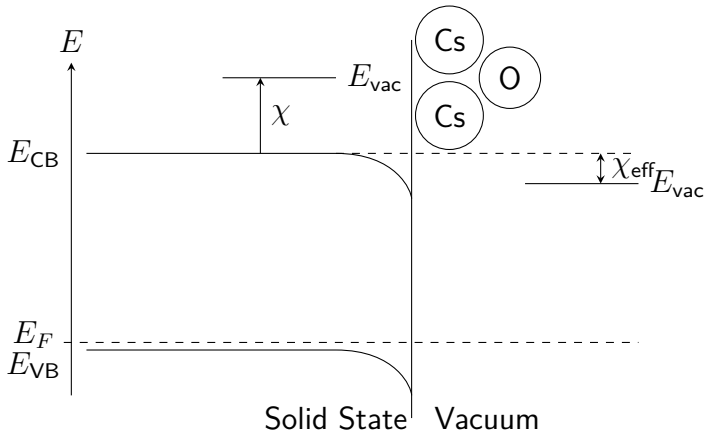

Figure 2.7.: *The scheme showcasing how the effective negative electron affinity χ_{eff} is created at the surface due to band bending by adsorption of Cs and O. Gap energy E_{Gap} separates the conduction band and the valence band. Since the used GaAs is heavily p-doped, the Fermi level is near the valence band, which is also true for the weaker doped superlattice crystal [20, p.37]. In order to excite an electron from the conduction band into the energy level of the vacuum in a semiconductor, additional energy χ is needed, which is defined as the electron affinity. Sketch adapted from [21].*

Doping the surface with a sub-mono layer of caesium and the oxidizing agent the Fermi level gets pinned and the bands on the surface will be bend down even more down. This leads to an effective negative electron affinity (NEA) $\chi_{\text{eff}} < 0$ and facilitates the transport of the electrons into the vacuum. Since these changes in electron affinity are around -200 meV, every disturbance on the surface will result in a loss of quantum efficiency [45]. Therefore it is important to keep and operate such photocathodes under very high vacuum conditions like 10^{-11} mbar in the PKA2 source (see section 3.1.2). The residual gas within the vacuum can be composed of H_2O,O_2,CO_2 and other species. Those mentioned are the most studied in their effects on the QE of a photocathode [46, 47]. Oxygen has been shown to have a particularly strong effect, lowering the QE to $1/e$ within 10 min [47]. Therefore in order to achieve a lifetime of 20 d it was concluded that the partial pressure of oxygen needs to be lower than 9×10^{-13} mbar [21].

2.2.1. Preparation of photocathodes

It is common to use oxygen (O_2) as oxidizing agent in the activation process but since its high reactivity other agents such as nitrogen trifluoride (NF_3) can be used [21, 22, 48]. The main advantage of NF_3 is its lower reactivity at temperatures below 200 °C [49]. In

temperature regions between 200 °C to 400 °C NF_3 is as reactive as oxygen and at even higher temperatures up to 1200 °C it becomes as reactive as fluorine [49]. Since the preparation of photocathodes takes place at room temperature the reactivity is lower than oxygen´s reactivity.

The dipole moment of NF_3 is with 0.234 D larger than the dipole moment of O_2 with 0 D [50]. The main theory of stability of an NEA surface explains the effect of emitting electrons with dipole momenta on the surface [51]. Since NF_3 has a larger dipole moment it is suspected that it will provide better or at least more stable QE over a longer period of time than with oxygen [52, 53].

Another option is to look at the polarizability of NF_3 and O_2. The polarizability refers to the degree of distortion of the electron cloud around a molecule by an external electric field. This deformation can induce a dipole moment that is non permanent. Looking at NF_3 the polarizability is 2.810 $Å^3$ [54] while for oxygen it is 0.802 $Å^3$ [55] for the mono atomic case and the diatomic case has a polarizability of 1.562 $Å^3$ [55]. This enhances the hints towards a higher NEA stability if NF_3 is being used.

In order to refresh cathodes, heat is applied to remove surface adsobate. This process of heat cleaning can be repeated but with O_2 it was found that those heat cleaning and activation cycles are not as extendable as with NF_3. It was found that with oxygen one could refresh the same cathode three times before the initial QE drops significantly whereas with NF_3 refreshing cycles up to eight times have been achieved [56].

2.3. Theory of Mott scattering as a tool for electron spin polarization measurement

Mott scattering is the solution of the scattering problem of spin ½ particles in Coulomb fields of atomic nuclei using a relativistic correct description by solving the Dirac equation [57]. In other terms: Mott scattering is similar to Rutherford scattering, where electrons weakly interact with the nucleus with electromagnetism instead of alpha particles wich strongly interact with the target nucleus [57, 58]. Particles carrying spin, when encountering a spinless nucleus, will be scattered. For Mott scattering this will be an electron hitting a (most commonly) thin gold foil when the polarization vector of the beam is perpendicular to the scattering plane. A sketch of this principle is shown in fig. 2.8.

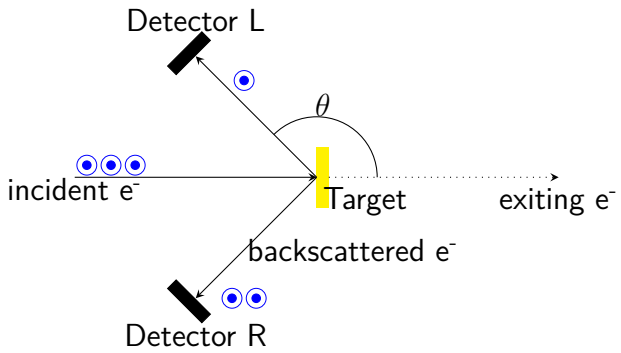

Figure 2.8.: *The schematic representation of Mott scattering process is shown. A fraction of the electron beam with its polarized electron ensemble scatters at the gold target. The electrons are backscattered at an angle θ into the detectors, which are used to calculate an asymmetry in the signals, the transmitted electrons are dumped in a Faraday cup.*

With its first theoretical description by Mott [59] and its numerical solution by Sherman [60] it is found that that the scattering angle of electrons depend on the energy of the electron, the atomic number of the target and many more detailed parameters. The atomic number Z is the most important parameter since it determines the magnitude of the spin interaction, which favours larger atomic nuclei. For a gold ($Z = 79$) nucleus at 100 keV, the angle measures 120° with a theoretical analyzing power, known as the Sherman function, of 0.39 [61]. The term "theoretical" is used because Sherman based his calculations on scattering with a single nucleus, which proves to be practically quite difficult, as illustrated by the variations in maximum sensitivity noted in [61] and shown in fig. 2.9. A numerical solution to the Sherman function (S) calculated with point nuclei is shown in fig. 2.9 with its energy and angle dependence.

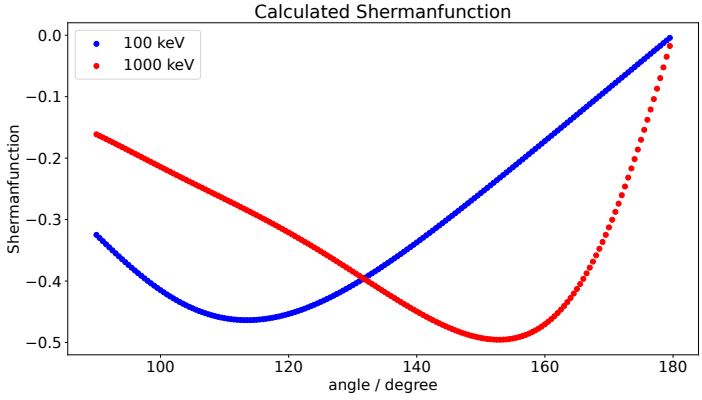

Figure 2.9.: *A numerical solution to the Sherman function calculated exemplary for electron energies at 100 keV and 1000 keV. Taken from private communication V. Tyukin, 2022*

One of the reasons for the difficulties is the lack of an appropriate model for the structure of the electron system in gold at 100 keV. On the one hand there are theoretical uncertainties in the calculation of the Sherman function S_0 and on the other hand experimental uncertainties are existent due to multiple scattering as reported in [57]. This will lead to smaller experimentally measured asymmetries with finite thicknesses of the targets. Additionally, background signals which have no asymmetry can influcence the experimental values. Therefore the eq. (2.6) with the effective Sherman function S_{eff} is associated with at least the same systematic uncertainties as that of the theoretical Sherman function S_0. Typically the accuracy of the Sherman function will be in the region of 1 % and thus makes the energy region of 100 keV not suitable for the high accuracy demands of the P2 experiment. However relative changes in the asymmetry and hence the ESP can be measured precisely. Since the detectors are permanently installed, i.e. do not move their angle, the Sherman function is fixed.

$$A = S_{\text{eff}} \cdot \vec{P} \tag{2.6}$$

If regarding the eq. (2.6) one finds that in order to observe long term dependent changes of polarization it is sufficient to only look at asymmetries (A) measured.

Since the polarization vector ($\vec{P}$) can be expressed as an asymmetry in detection rate if one considers the rate on the detector is proportional to the number of electrons N with arrows indicating up or down for their respective spin direction:

$$P = \frac{N_\uparrow - N_\downarrow}{N_\uparrow + N_\downarrow}. \tag{2.7}$$

Due to the measurement geometry one can justify the change of P from vectorial to scalar. Only the ESP component orthogonal to the scattering plane can be measured with a non vanishing asymmetry since it is not parity violating [8, p.53].

The number of electrons can be defined as $N_\uparrow = \sqrt{R^+L^-}$ and $N_\downarrow = \sqrt{R^-L^+}$ with R and L denoting the detectors as in fig. 2.8 with $+$ or $-$ defining the helicity of the light. The introduction of a factor $Q = \frac{R^-L^+}{R^+L^-}$ one finds the asymmetry as:

$$A = \frac{1 - \sqrt{Q}}{1 + \sqrt{Q}}. \tag{2.8}$$

The Q factor provides the additional advantage that helicity-correlated current and position fluctuations cancel out in a first order approximation. Although the asymmetry A is still dependent on the Sherman function, the transformation into eq. (2.8) expresses A in terms of measurable detector count rates, removing the need for immediate knowledge of the

Sherman function for the purposes of experimental measurement. Therefore, this formula will serve as the primary observable in analyzing polarization changes throughout this study. For easier distinctiveness, the asymmetry percentage will be denoted as $\%_A$ in this work.

2.4. Theories and gaps in the context of this research

Spin depolarizing effects play a crucial role not only in accelerator physics but also in spintronics and its related fields. While accelerators use the ESP as a tool to examine for example parity violation, spintronics are investigating for faster information storage and computing [62–64]. Fortunately, the literature has extensively documented the three major contributors in GaAs: D'yakonov-Perel (DP), Elliot-Yafet (EY) and Bir-Aronov-Pikus (BAP) mechanism [65–68]. The mechanisms are briefly described in table 2.1 with their respective spin relaxation times for bulk-GaAs at high doping concentrations of $10^{19}\,\mathrm{cm}^{-3}$.

Table 2.1.: *Summary of spin relaxation mechanisms in bulk GaAs as representative of semiconductors.*

Mechanism	**Description**	**Spin relaxation time estimated from [69]**
Elliot-Yafet (EY)	Scattering of electrons on atoms and phonons, particularly in band-bending zones where electrons gain enough energy for significant scattering.	$1 \times 10^{-9}\,\mathrm{s}$
D'yakonov-Perel (DP)	Spin precession due to an effective magnetic field within the band structure, arising from spin-orbit coupling.	$1 \times 10^{-10}\,\mathrm{s}$
Bir-Aronov-Pikus (BAP)	Scattering of electrons with holes, involving interactions with impurities in the crystal lattice.	$1 \times 10^{-11}\,\mathrm{s}$

Within the semiconductor the BAP mechanism is the fastest depolarization mechanism. It involves the scattering of electrons with holes, which are present in especially p-doped materials. That makes the BAP mechanism dependent on the doping concentration of the semiconductor. The heavy p-doped GaAs is discussed in table 2.1 while the superlattices

typically are doped with $10^{17}\,\mathrm{cm}^{-3}$ in the active layers [28, 29]. This lower doping concentration in the active layer significantly reduces the BAP mechanism towards negligible magnitudes [70].

The next important depolarization mechanism is the DP. If electrons are excited into the conduction band they will momentarily induce an effective magnetic field. This magnetic field induce spin precession in a way that the spin polarization can be lost.

The slowest in respect to extraction time versus spin relaxation time is the EY mechanism. There electrons scatter with atoms in the band bending region. In the band bending region the electrons are accelerated and gain enough energy to make such scattering feasible.

Other effects like hyperfine interaction with e.g. Overhauser fields do not play a crucial role due to their long spin relaxation times in the order of $10^{-5}\,\mathrm{s}$ [71]. Typical electrons arrive with thermal velocity the surface of the semiconductor which will gain additional kinetic energy due to band bending. The thermal velocity can be estimated at 25.8 meV and the kinetic energy can be estimated as 250 meV [72]. With those numbers one finds the DP and BAP mechanism as the most prominent contributor to ESP losses using the figure 1 [69]. Furthermore using bulk-GaAs with high doping density ($10^{19}\,\mathrm{cm}^{-3}$ Zn) the BAP mechanism seems to dominate, where as with superlattice GaAs and two orders of magnitude lower doping in the active zone ($10^{17}\,\mathrm{cm}^{-3}$) the depolarisation can be attributed to the DP mechanism [69].

Gasteyer claimed in his work that no surface adsorbate influences the electron spin polarization [22]. However one finds that with decreasing QE the asymmetry changes significantly as seen in fig. 2.10. In the work of Gasteyer it is explained that the surface adsorbent does not have an influence on the ESP, however he noted that it correlates with the absolute value of NEA and hence the work function of the semiconductor [22]. Similar asymmetry changes have been observed at the MAMI accelerator [73].

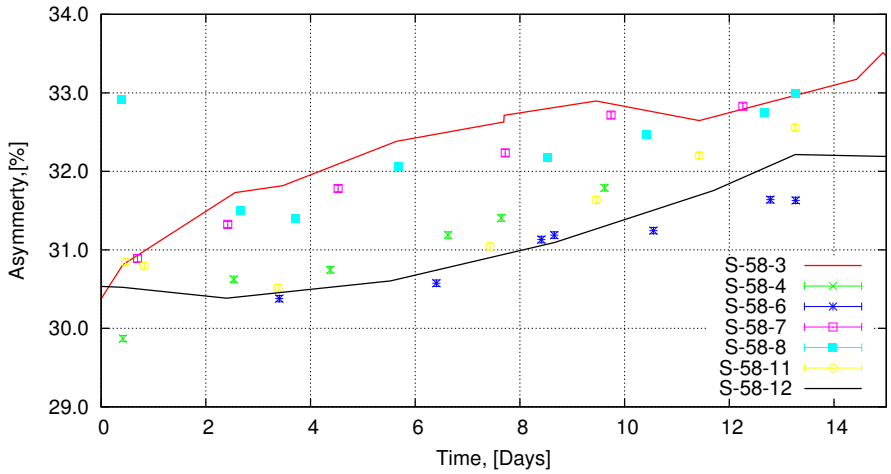

Figure 2.10.: *Time dependence of the measured asymmetry at MAMI[73]. One cathode (S-58) was prepared (numbers 3 to 12) and used in several experiments. The general trend towards higher asymmetry at the end of an experimental time of 14 d is consistent throughout the different activation cycles. The cathode was used with a QE, from 1 % down to 0.1 %.*

Despite the lack of dedicated studies of polarization behavior in particle accelerators such as MAMI, which primarily serve as user facilities, and a lack of models that explain the observed changes in asymmetry, this thesis attempts to understand the complicated evolution of electron spin polarization over long periods of time. The evolution of the ESP from excitation until extraction can be interpreted similar to the Spicer three step model as depicted in fig. 2.6. In the excitation step it is assumed that the wave functions match perfectly, but the doping disturbs the translational invariance of the crystal. Therefore the polarization is decreased already after the absorption of the photon. The transport to the surface is characterized by the different depolarization mechanisms before mentioned and an even larger decrease of the measured ESP has to be expected. Finally the band bending zone and the interaction with the surface will additionally disturb the ESP so all contributions can be summarized as in eq. (2.9):

$$P_{\text{exp}} = P_{\text{abs}} \cdot P_{\text{trans}} \cdot P_{\text{BBZ}} \cdot P_{\text{theo}} \tag{2.9}$$

where:

P_{exp} : experimentally measured polarization
P_{abs} : polarization losses due to absorption
P_{trans} : polarization losses due to the transport
P_{BBZ} : polarization losses due to interaction in the band bending zone
P_{theo} : theoretically expected polarization.

At low QE the term P_{BBZ} approaches unity as the the band bending zone plays a diminishing role in the depolarization due to the degradation of the NEA surface. The leaves only two primary sources of polarization loss: those associated with photon absorption (P_{abs}) and electron transport (P_{trans}).

By investigating the mechanisms behind the changes in polarization of photocathodes, this thesis aims to provide insights into the behavior of polarized electron beams.

Chapter 3

Experimental Setup

For this work, a fully equipped system for generating and measuring the asymmetry of spin-polarized electron beams was already available, enabling precision measurements. This apparatus is called Polarisierte Kanone 2, engl. polarized electron gun 2 (PKA2) and consist of a 100 keV electron source, a beam transport line with correction magnets, a Wien filter and a Mott polarimeter which will be discussed in this chapter.

3.1. Detailed description of the apparatus and its components

This setup exists since the 1990s [24] and has served for nearly three decades in several different experiments and studies. The original setup was modified in 2007 [74] and in 2018 [75]. Starting with the configuration established in 2018, the subsequent chapter outlines the setup along with the modifications that have been implemented up to the present time.

3.1.1. Overview

The laboratory houses the 100 keV photo electron source which is equipped with a preparation chamber and a load-lock system. The beam line transports the electron beam though the apparatus to the Mott polarimeter. At first an alpha magnet deflect the beam on an 270° angle onto the horizontal beam line, in which remnants of in depth beam diagnostics had been located. A second alpha magnet transports the electron beam on the path towards the Mott polarimeter. In fig. 3.1 a rough sketch of the whole apparatus is depicted.

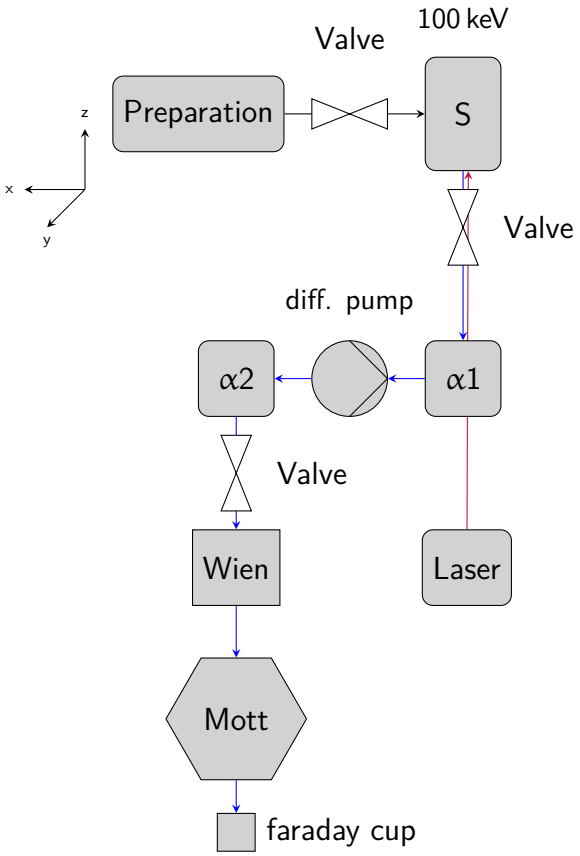

Figure 3.1.: *An overview of the PKA2. Photocathodes are introduced and activated in the preparation chamber (Preparation). A valve divides the preparation chamber from the source chamber (S) and another valve separates the source from the beam line in order to maintain high vacuum conditions. A laser illuminates the cathode from below the source through a window. The produced electrons (blue arrows) are transported through the first alpha magnet (α1) which projects the beam into the horizontal plane. To make sure that the vacuum conditions from the experiments do not interfere with the source the electrons pass through a differential pumping stage (diff. pump). After that they are deflected by a second alpha magnet (α2), passing another valve, into the the spin rotation system (Wien) for the Mott scattering experiment (Mott). After the scattering experiment the electron beam is captured in a Faraday cup.*

The electron beam will travel a distance of 5 m until it reaches the polarimeter and is stopped in a Faraday cup behind the Mott targets. The differences of the setup in the previous works and this work is the reduction in beam diagnostics like the pulse length measurement [75]. The remaining extensive beam diagnosis was not necessary to activate as checking the beam position at various screen positions was sufficient. The polarimetry was changed into a single Mott polarimeter of [76] where a double scattering Mott polarimeter had been

previously installed in [75].

3.1.2. Source

The photo electron gun used in this work was designed and build in 1994 and is in usage until this day [24]. For high current application the gun was equipped with extra non evaporatable getter (NEG) modules to achieve even longer lifetimes of photocathodes [74].

The source operates at 100 keV and has vacuum conditions better than 1×10^{-11} mbar. These ultra high vacuum conditions are important since any disturbance of the NEA surface will result in lower QE (refer to section 2.2). An illustration of the source design is shown in fig. 3.2 while a photograph of it is shown in fig. 3.3.

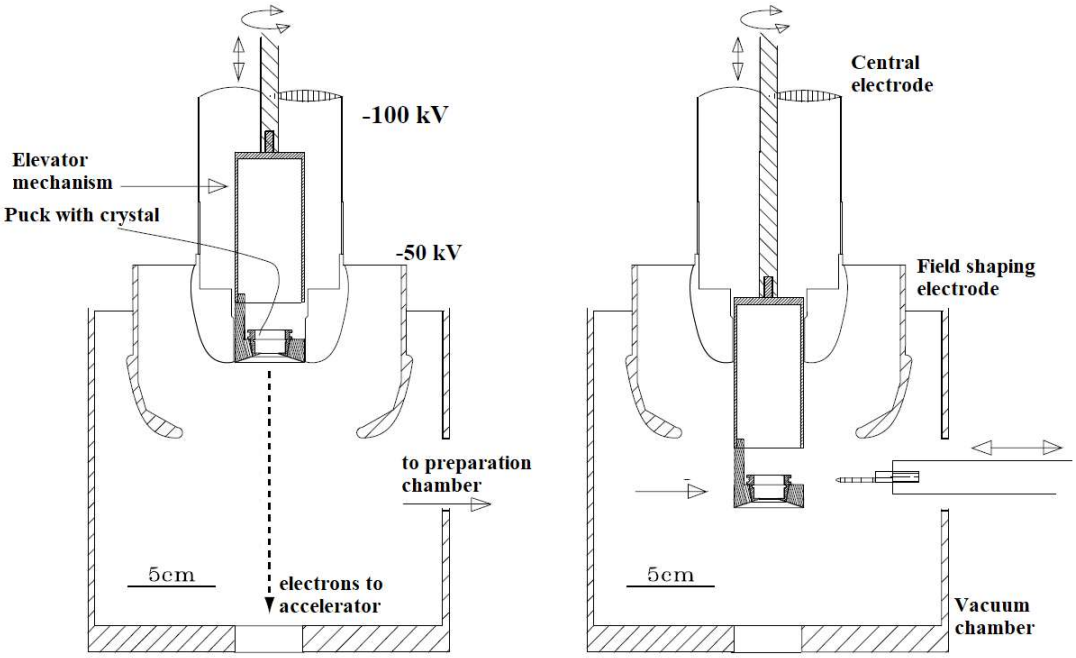

Figure 3.2.: *A technical sketch of the PKA2 photo gun source chamber [77, 78]. On the left the elevator position for operation is shown while on the right the position of the elevator for cathode exchange is shown.*

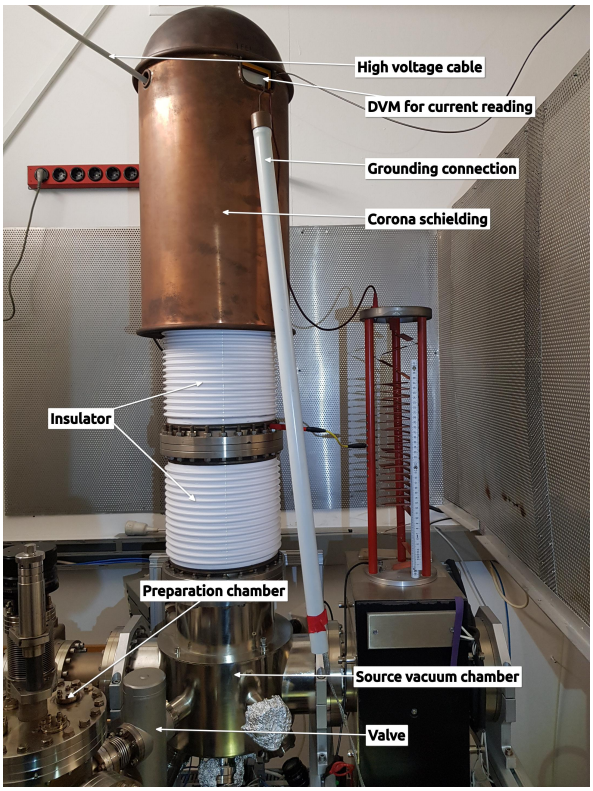

Figure 3.3.: *A photograph of the source including the insulators and corona shield is shown.*

3.1.3. Beamline

The electron beam exits the source if a valve between the source chamber and the beam line is opened. It is transported in a vacuum system to the Mott polarimeter. Since the electrons are charged particles the usage of the Lorentz force can be applied in order to force them onto a certain trajectory as described in eq. (3.1) [6, p.4]:

$$\vec{F_L} = q\vec{E} + q\vec{v} \times \vec{B} \tag{3.1}$$

with:

$\vec{F_L}$: Lorentz force
q : charge
$\vec{E}$: electric field
$\vec{v}$: velocity
$\vec{B}$: magnetic field.

This is also true for relativistic particles and their optical properties like focusing can be described by using the known transport matrices if only linear beam dynamics are applied. This implies that dipole magnets can be used to steer an electron beam while quadrupoles will focus/ defocus such a beam [6, p.53ff]. Parts of the beam line are shown in fig. 3.4.

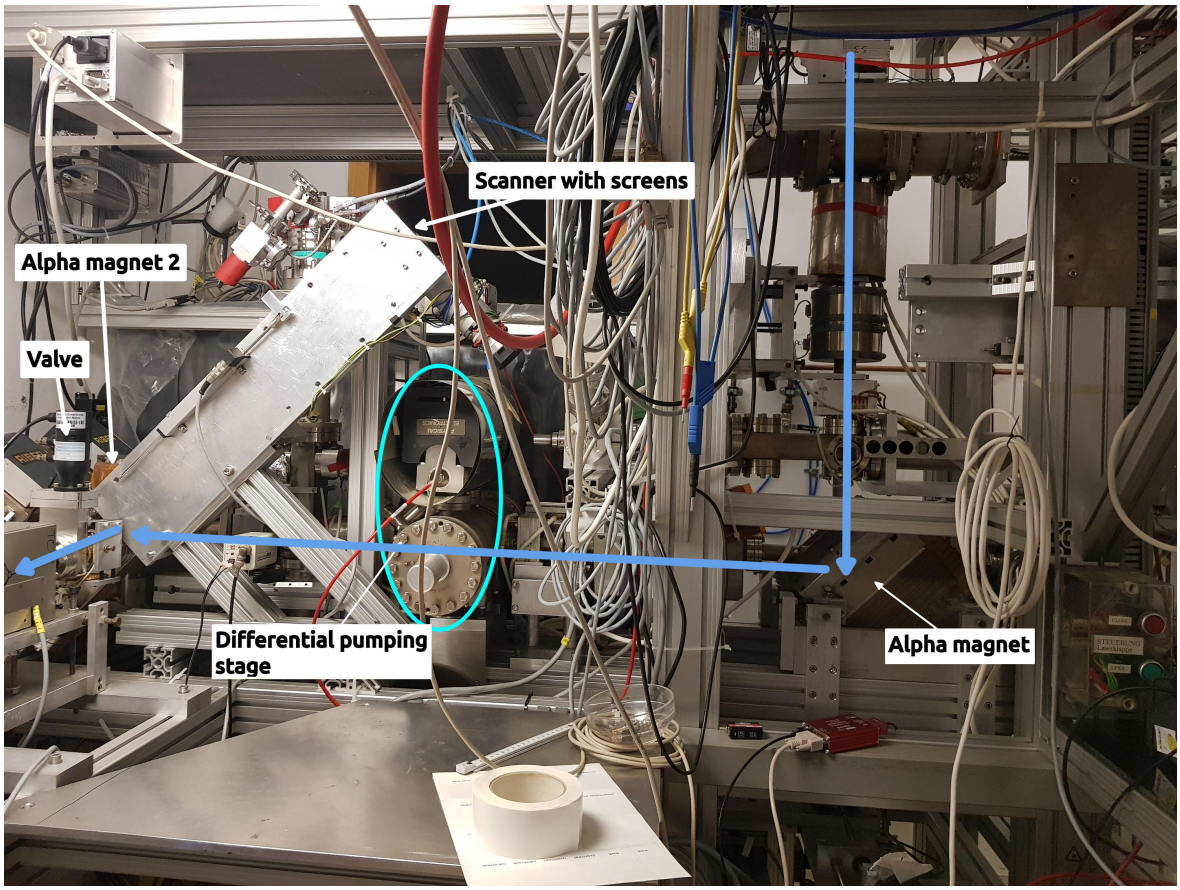

Figure 3.4.: *A photograph of the beam line. The blue arrows roughly sketch out the electron beam path. The electrons are produced in the source and travel downwards to the first alpha magnet. The red ellipse enclose the differential pumping stage.*

An alpha magnet deflects the electrons in an 270° angle into the horizontal plane. In order to maintain a high quality vacuum the source is extra protected by a differential pumping stage which the electrons have to pass through after the first alpha magnet.

A differential pumping stage is an aperture with low gas conductivity with high pumping speeds at either side of this stage. This will prevent that residual gases from the experimental sites will cause harm to the source´s vacuum. In past works especially the double scattering Mott polarimeter had vacuum levels in the order of 10^{-6} mbar [79]. Unprotected this could cause the photocathode inside the source to degrade within hours of operation. The pressure

in the single Mott polarimeter used in this work as described in section 3.1.5, is 10^{-8} mbar while upstream towards the source the pressure in the beam line is 5×10^{-10} mbar, which shows the work of the differential pumping stage.

A second alpha magnet will bend the electron beam again in an 270° angle into the Wien filter and towards the Mott polarimeter. In fig. 3.5 the final parts of the beam line are shown which include the Wien filter and the Mott polarimeter.

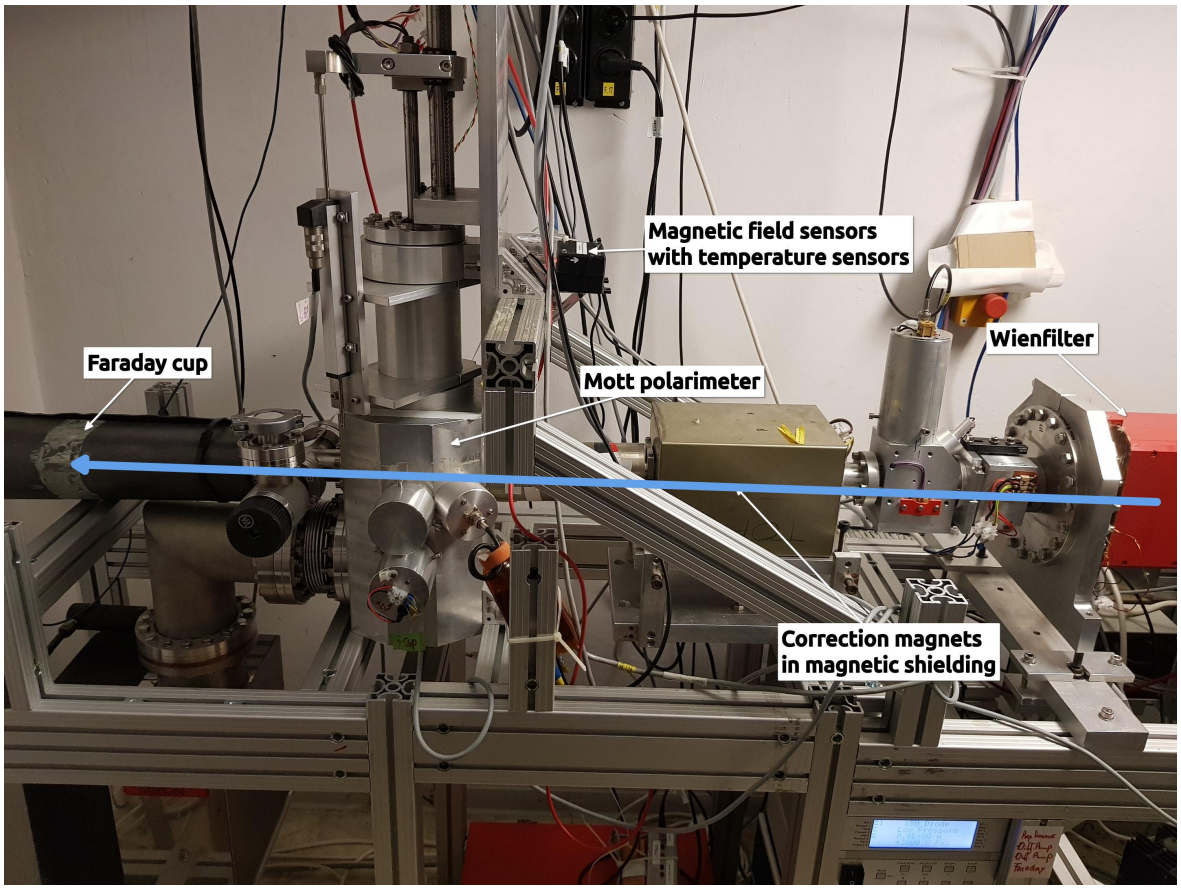

Figure 3.5.: *A photograph of the beamline with the Wien filter and the Mott polarimeter. The blue line indicate the path of the electrons through the vacuum. The correction magnets are housed in magnetic shielding, while the Faraday cup is covered by lead shielding.*

3.1.4. Wien filter

Within the Thomas-BTM formula it is described that magnetic fields in combination with electrical fields will influence the relative angle of the spin vector with respect to the transport vector [80]. This is feasible in the low energy regions of 100 keV since the rotation

is proportional to $\frac{1}{\beta\gamma^2}$, the inverse of the product of the factional speed of light times the Lorentz factor squared [81]. The application is e.g. a Wien filter that will turn the ESP and therefore the polarization vector perpendicular to the plane of detection. As explained in section 2.3 it is necessary to rotate the ESP orthogonal to the scattering plane of the detection plane. In this setup a Wien filter is used for that task as it had been a well proven method for this application [81]. The working principle of such a device is illustrated in fig. 3.6 with the different acting forces.

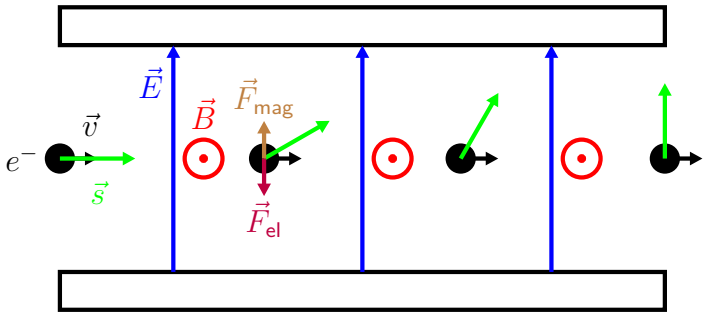

Figure 3.6.: *Sketch of the fields, forces and precession of the spin $\vec{s}$ (green) within of a Wienfilter while an electron flies through with a velocity $\vec{v}$. Courtesy: C. Matejcek*

The magnetic fields ($\vec{B}$, in red) are orthogonal with respect to the electric fields ($\vec{E}$, in blue). The Wien filter is designed in such a way that the velocity filtering effect is negligible, as the magnetic and electric forces ($\vec{F}_{\text{mag}}$ & $\vec{F}_{\text{el}}$) are equal for a 100 keV electron beam. If the electrons would be significantly faster or slower they would hit the walls of the vacuum chamber and not leave the Wien filter.

The Wien filter used is depicted in fig. 3.7 with its components. The orientation of the electron beam path is flipped in respect to fig. 3.6 but the orientation of the magnetic field and the electric field remains the same.

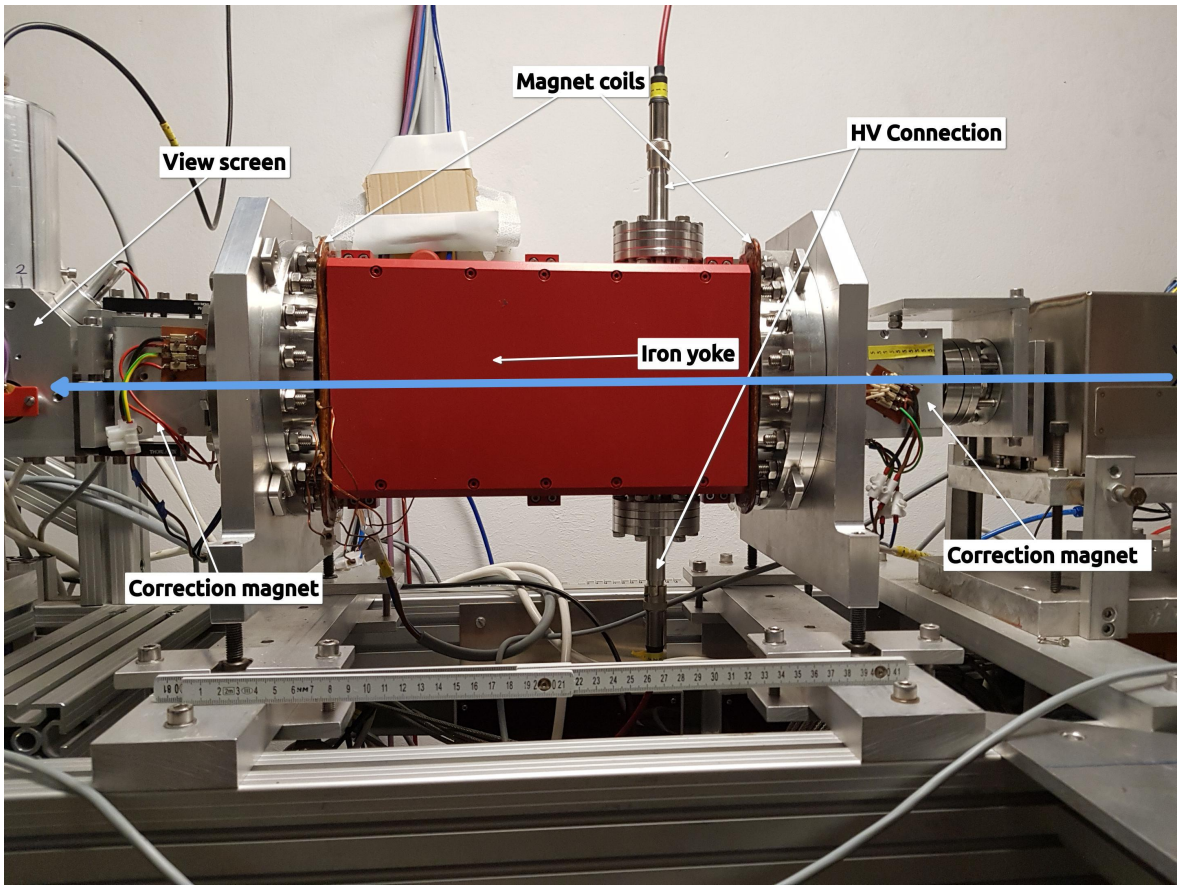

Figure 3.7.: *A photograph of the used Wien filter. In blue the electron beam path through the vacuum is indicated.*

In order to verify the rotation of the ESP vector out of the scattering plane a calibration of the Wien filter has been performed. In fig. 3.8 the measured asymmetry is plotted against the Wien filter dipole current. After each change of the Wien filter dipole current, the strength of the electric field and quadrupoles following the Wien filter had to be matched in such a way, that the electron beam was a round spot again with sizes smaller than 3 mm on a view screen at the Mott polarimeter. The Wien filter itself acts rotation angle dependently as a strong quadrupole which can significantly change the shape of the electron beam. On those data points a sine fit was applied since the movement of the ESP is a rotation. The applied fit is written in eq. (3.2) and is characterized by the first maximum of the sine:

$$f(I) = A_{\text{max}} \cdot \sin\left(\frac{I}{C}\right) \tag{3.2}$$

with:

A_{max} : maximum asymmetry measured
I : Wien filter dipole current in A
C : the first maximum of the fitted sine.

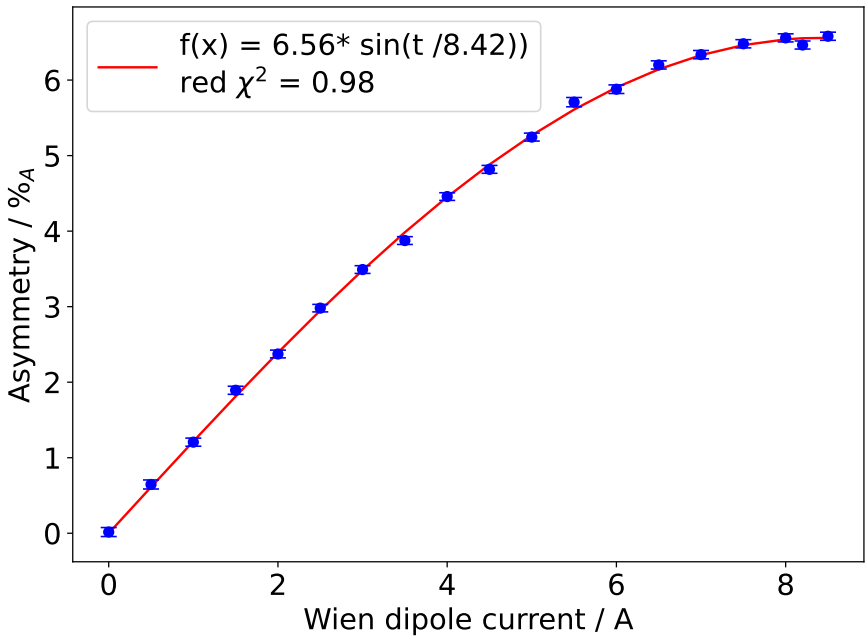

Figure 3.8.: *The Wien filter calibration curve is shown with a sine fit. The maximum asymmetry is reached at 8.42 A for the Wien dipole current. The sine fit was chosen because the movement of the ESP is a rotation.*

Figure 3.8 demonstrates the asymmetry with respect to the Wien dipole current. The maximum asymmetry is reached if the ESP is orthogonal to the detection plane and minimum if the ESP is parallel or within to the detection plane. A sine fit gives the first maximum current as 8.42 A which would translate to a 90° rotation of the spin.

3.1.5. Mott polarimeter

In this work a Mott polarimeter designed and build by Hartmann in 1997 was used [76]. Since its inception modifications and adjustments regarding the gold targets and the detector pin holes have been made [82]. A scheme of the Mott polarimeter is shown in fig. 3.9 together with a photograpth in fig. 3.10.

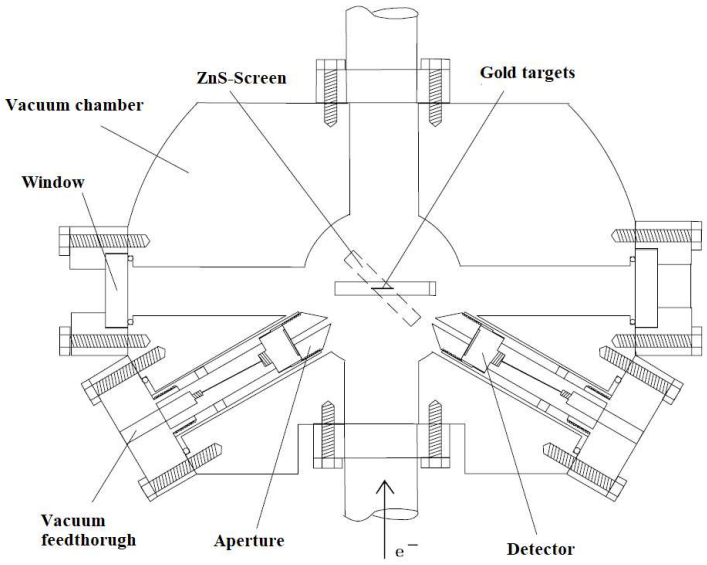

Figure 3.9.: *A scheme of the Mott polarimeter used in this work. It was designed and build by Hartmann in 1997 [76]. For this work the apertures have been reworked and have now a 2 mm hole.*

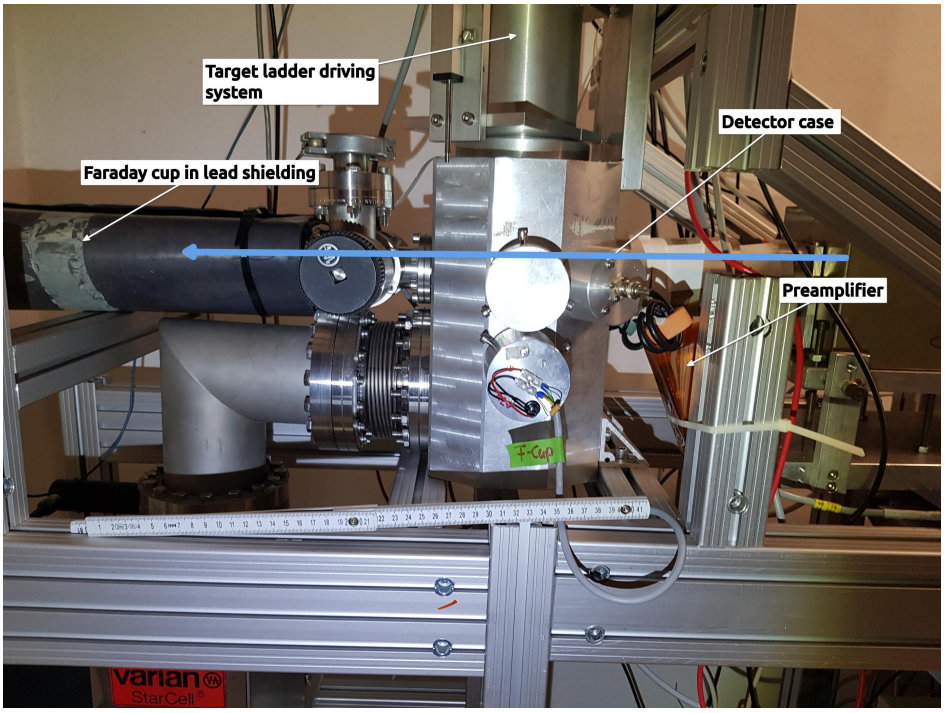

Figure 3.10.: *The picture shows a side view of the polarimeter in use. In blue the electron beam path is indicated.*

The polarimeter has the gold targets in its center and according to section 2.3 the detectors are arranged in a 120° angle from the exiting electron beam, as needed for 100 keV electron scattering. The detectors are surface barrier detectors made from silicon. A 2 mm aperture is installed in front of the detectors to reduce background from electrons scattered towards the wall of the apparatus.

If the electron beam position changes about 2.5 mm, which is one beam width, the ideal backscattering angle of 120° is missed by 0.3° which will cause a relative change of the Sherman function by 0.3 % at 100 keV. The beam does not shift more than half a millimeter which is ensured by monitoring the beam position regularly. Due to the broad curvature of the Sherman function at 100 keV as seen in fig. 2.9 the mismatch of the ideal backscattering angle and the actual angle can be as big as 2° to cause a 1 % relative change of the Sherman function. The Sherman function for 100 keV cannot, until now, be better determined as 1 % as discussed in section 2.3.

For this work the gold targets have been changed. The thickness ranges from 99.5 nm to 476.7 nm. A list of the used targets is in table 3.1 while the positions are shown in fig. 3.11. The foils are secured on aluminum frames with a 10 mm diameter hole as seen in fig. 3.11 (right). The gold foils and their holder have been loaded onto a motorized system, which was designed and build by Dombo [83].

Table 3.1.: *The different targets build into the Mott polarimeter. The grey highlighted row indicates the most used target in this work.*

Position as in fig. 3.11	Thickness measured	Thickness calculated
0	ZnS Screen	–
1	192 µg cm^{-2}	99.5 nm
2	187 µg cm^{-2}	96.9 nm
3	480 µg cm^{-2}	248.7 nm
4	920 µg cm^{-2}	476.7 nm
5	empty	–

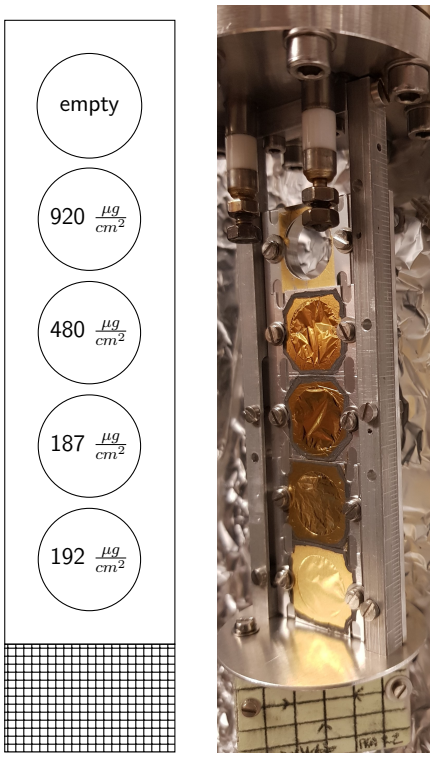

Figure 3.11.: *Sketch of the target holder on the left. The numbers inside the circles give the thickness of the gold, and the positions as in table 3.1 are from bottom to top. Photograph of the target holder on the right with the gold foils. The ladder measures 130 mm in length.*

Calibration

The positions and homogeneity of each foil inside the vacuum system of the Mott polarimeter have been measured for calibration purposes. Therefore the asymmetry was scanned across all targets and the result of the most used target (refer to table 3.1) is depicted in the contour plot in fig. 3.12. The beam position in along x (refer to fig. 3.11) was adjusted with a steerer in front of the polarimeter while the position in y was controlled via the driving mechanism of the target ladder itself both have been varied in steps of 1 mm.

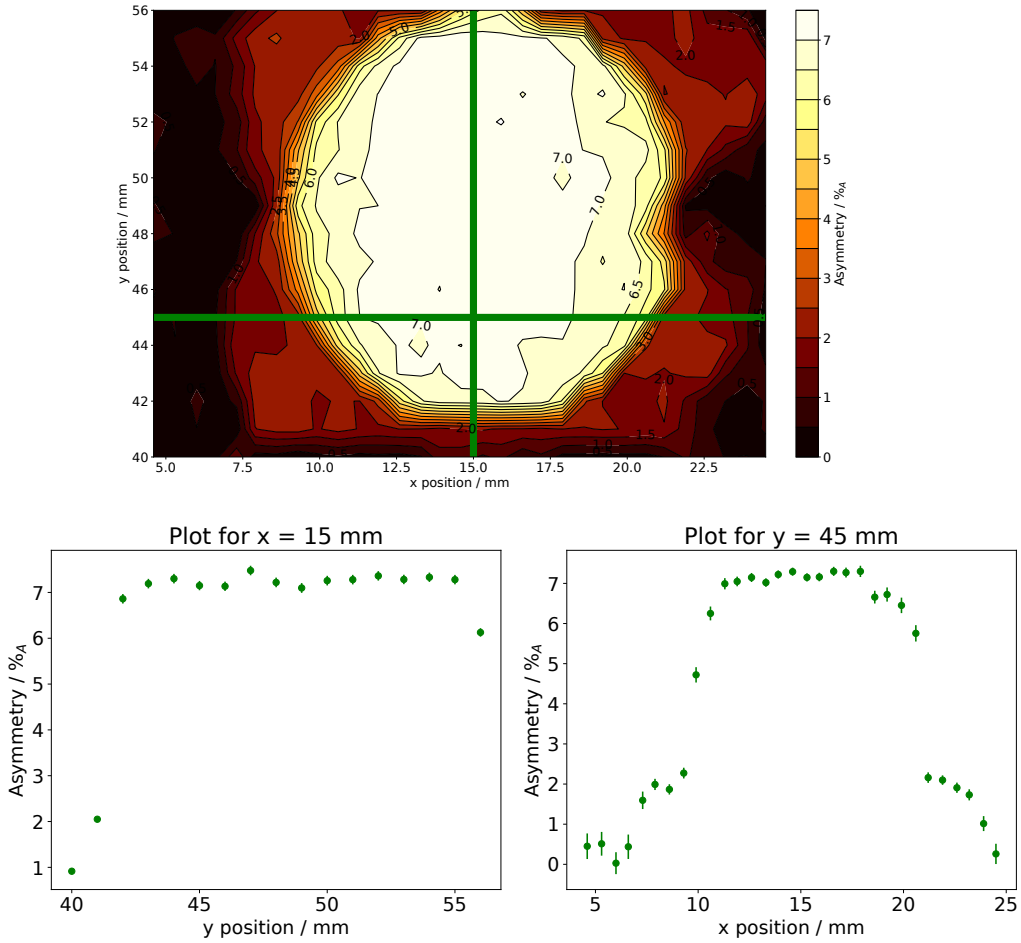

Figure 3.12.: *The resulting contour plot of the position calibration of foil number one. The round shape of the holder is clearly visible and the homogeneity is given across the surface. The green lines along $y = 45\,\text{mm}$ and $x = 15\,\text{mm}$ indicate, where the plots below are taken from. There the homogeneity of the asymmetry is shown to be good in a region of 10 mm in each direction. Each point on the foil was measured 101 times. The crossing point of both lines mark the spot where the main measurements have been performed. This point was chosen because it was easiest to identify and verify using a camera image.*

In order to take into account the multiple scattering processes a calibration with different gold target thicknesses can be made and the resulting effective Sherman function can be used to calculate the polarization according to eq. (2.6). Therefore a measurement for extrapolating this polarization of the electron beam has been performed. The asymmetry of each foil has been measured with high statistical accuracy. The combined count rate $R_L + R_D$ of each target has been plotted against the measured asymmetry, as seen in fig. 3.13. This method was suggested by Gay and Dunning and a linear fit has been performed to extrapolate the

asymmetry to zero count rate [57, 84]. This measurement lead to the conclusion, that the superlattice wafer at QE as low as 1.2×10^{-3} % at 780 nm is to be estimated > 90 %. The used S_0 for the polarization determination as described in eq. (2.6) is -0.3975 [85].

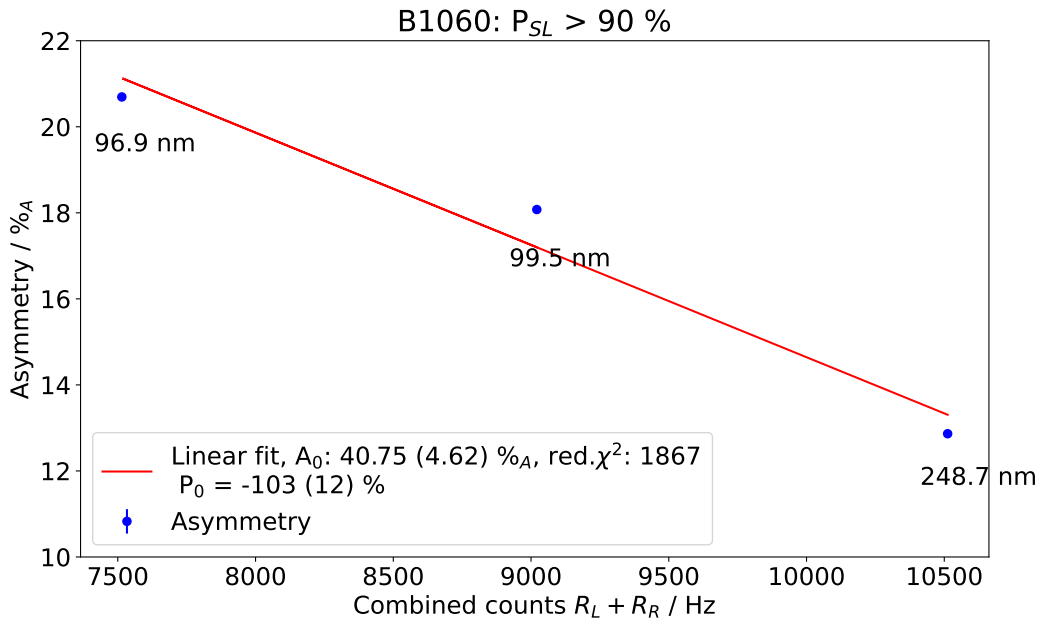

Figure 3.13.: *The measured asymmetry is shown with respect to the combined count rate. The foil thickness is written next to each data point. In order to calculate the polarization, the value for the theoretical Sherman function used, is -0.3975 [85].*

Even though the targets 1 and 2 (refer to table 3.1) are similar in thickness they produce different asymmetries. Similar issues have been reported in [86] with different targets on the same polarimeter. The linear extrapolation is justified if the targets are thin so that multiple scattering is negligible. This can be done if more gold targets are measured, preferably even thinner ones than the used one.

For a detailed discussion of errors refer to section 4.3.4. The thick gold targets are the main contributor to the large errors, which are in the magnitude of 10 % for the polarization measurement.

3.1.6. Laser system

The main laser is a laser diode (LD) emitting 808 nm light. In fig. 3.14 the layout is depicted. In a later stage of this work an additional laser diode of 780 nm was implemented which was

coupled into the laser system before the liquid crystal attenuator (LCA). The wavelength of the main laser diode is given as (808 ± 3) nm [87], while the secondary laser is given with a wavelength of (780 ± 10) nm [88]. The wavelength was measured with a wavelength meter[1] which resulted in a wavelength of (785 ± 1) nm.

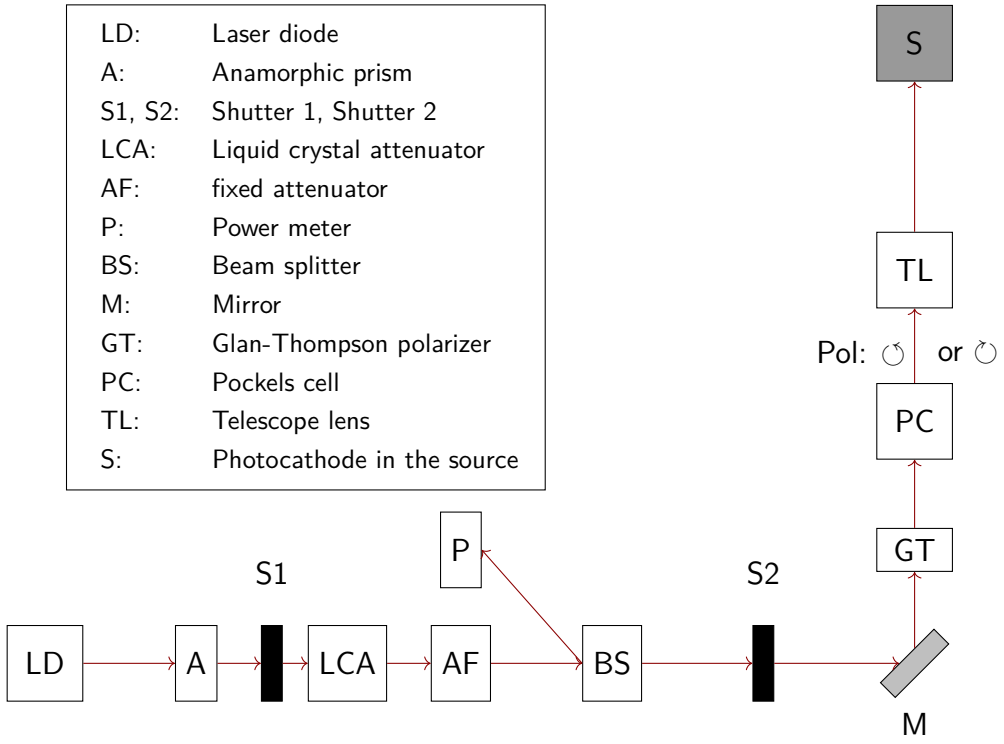

Figure 3.14.: *The laser system of the PKA2 is sketched here. The laser light passes through an anamorphic prism in order to shape the laser beam round then it passes through attenuator, beam splitter and linear polarizers. The Pockels cell transforms the linear polarized light into circular polarized light which is then transported to the source onto the cathode. This sketch is not to scale.*

The laser beam from the 808 nm diode was elliptical, therefore an anamorphic prism was used to project the beam in a round shape. Two different shutters have been introduced at different positions to have redundant safety, since only in combination with light and a photocathode, current could be extracted. The first shutter S1 is optional since it was a test setup elsewhere. Followed by the first shutter a set of attenuator have been implemented. The LCA enables a continuous attenuation down to 1:100 of the initial laser power of 150 mW. The attenuation curve is depicted in fig. 3.15. After the LCA a set of different motorized fixed attenuator could be inserted into the laser beam path. The fixed attenuator

[1] APEλ500, APE Angewandte Physik und Elektronik, Specifications: 450 nm to 950 nm, 0.1 nm resolution, 0.5 nm accuracy

are neutral density filters specified for the wavelength of the lasers used. The laser power was read by a power meter which picked up the light reflected from the beam splitter. The splitting ratio was 10.4 % including all optics and related transmission losses within the laser beam line up to the source. With that, a laser calibration curve could be measured at any time during the operation, as seen for example in fig. 3.16.

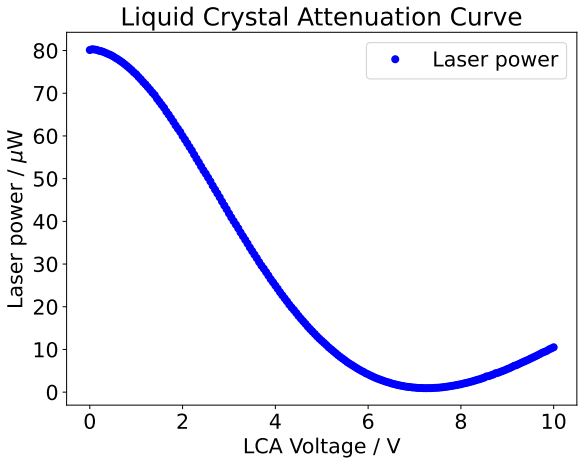

Figure 3.15.: *The seamless attenuation generated by the LCA is shown here. The laser power was plotted in respect to the input voltage of the LCA.*

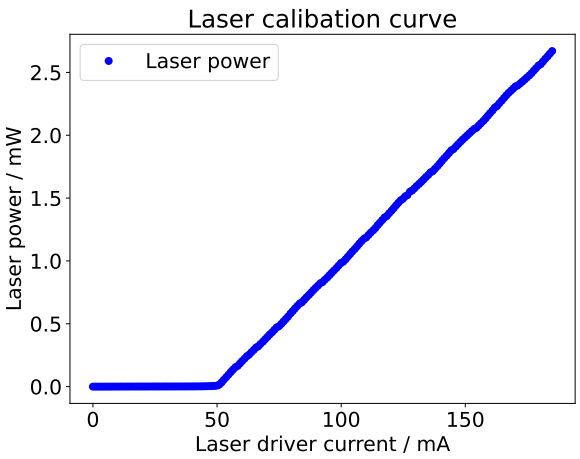

Figure 3.16.: *The laser driver current is shown with its emitted power on the cathode. The laser diode starts to emit with lasing property at 55 mA driver current.*

Three different dynamic ranges of laser power have been used for the different measurements: a low intensity region up to 50 µW for the Mott measurements, a medium intensity region up to 1 mW for the measurement of the quantum efficiency QE and the high intensity region until the maximum achievable transmitted power of 16 mW for the degradation process. The power was chosen in a way that the electron current reached certain values: for the Mott measurements an electron beam current of 300 pA was adequate (see section 3.3), while the aimed current for the QE measurement was up to 150 nA. The degradation required high currents from 1 µA to 100 µA and therefore needed higher laser power intensities, as discussed in section 3.3. For the Mott measurements and the QE measurements have been performed with the same laser current; only the variable attenuator in combination with fixed attenuators have been used. For the degradation process the laser current was changed because the exact wavelength during the degradation was not considered.

3.1.7. Preparation system

Preparation or activation, as both terms are used interchangeable, happened at a separate chamber, the preparation chamber. The preparation chamber is located next to the source chamber and their vacuum system is separated via a valve. New cathode material and the oxidizing gases, as described in section 2.2, are introduced via a load lock system. The preparation chamber is depicted in fig. 3.17 with a photograph in fig. 3.18.

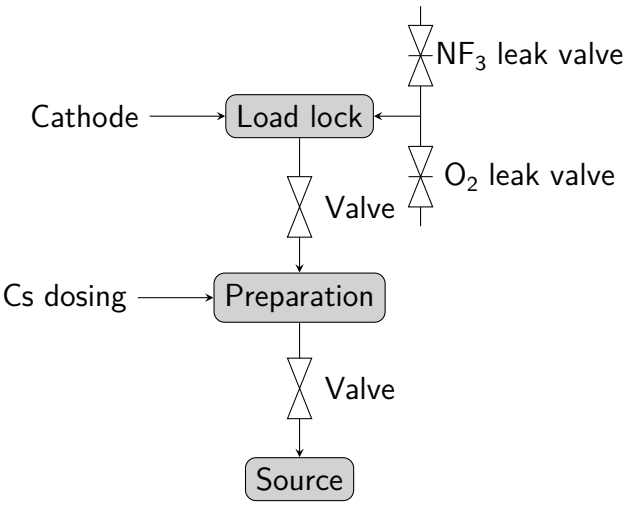

Figure 3.17.: *A sketch of the preparation chamber and the connecting infrastructure. The load lock enables the introduction of new cathode material without breaking the vacuum of the preparation chamber. The load lock and the preparation chamber are separated with valves.*

The load lock system is of small volume and baking it to good vacuum levels of 1×10^{-10} mbar takes three days, while baking the preparation chamber to a vacuum level down to 1×10^{-11} mbar takes up to two weeks. In fig. 3.19 the residual gas mass spectra are shown. On the left the clean preparation chamber is shown where the hydrogen species clearly dominate while on the right hand side the valve between the load lock and the preparation chamber is opened and the leak valve for the NF_3 reservoir is opened. The peak at a mass to charge ratio of 52 is clearly visible, which indicates the NF_2^+ fragment. The difference in partial pressures are due maturing process a vacuum chamber undergoes: the clean residual gas spectrum was taken after a bake out of the chamber while the NF_3 spectrum was taken two years after that. During that time the amount of residual gases significantly reduces if there is no venting of the chamber.

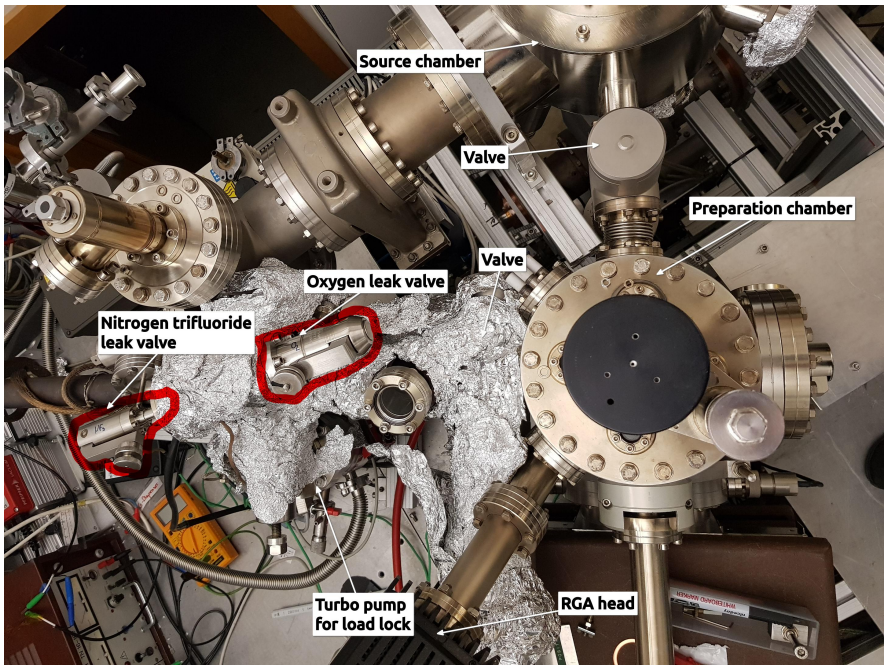

Figure 3.18.: *The photographic overview of the preparation chamber and its connecting infrastructure. Most of the load lock is covered in aluminum foils due to its frequent bake outs. The aluminum covers the heating elements and insulates the heat from the cooler laboratory. (RGA stands for rest gas analyzer.)*

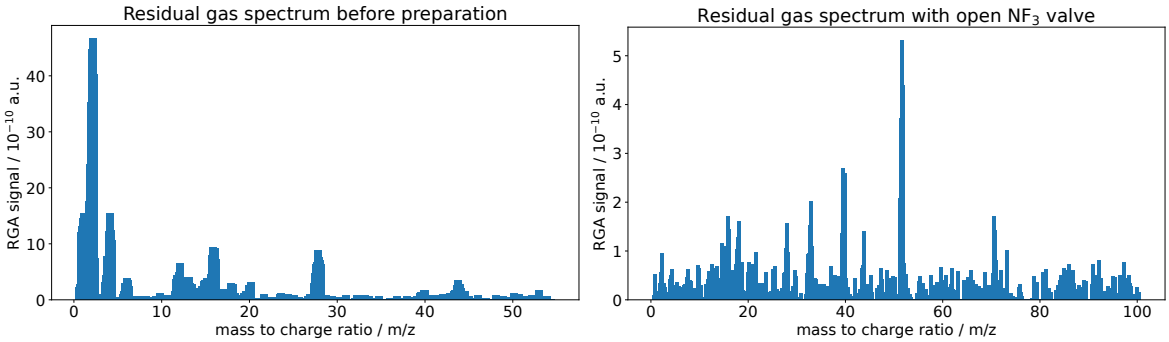

Figure 3.19.: *Residual gas mass spectra of the clean preparation chamber (left) before any preparation and with open NF_3 valve (right).*

During preparation of a photocathode the valve between the load lock and the preparation chamber is open while the gases are controlled by a manual leak valve. The pressure in the preparation chamber rises during the activation process approximately to 1×10^{-10} mbar which is recovered after finishing the process within one to two hours.

A Cs dispenser was mounted in the preparation chamber right below of a ring anode. A sketch of the preparation arrangement is shown in fig. 3.20.

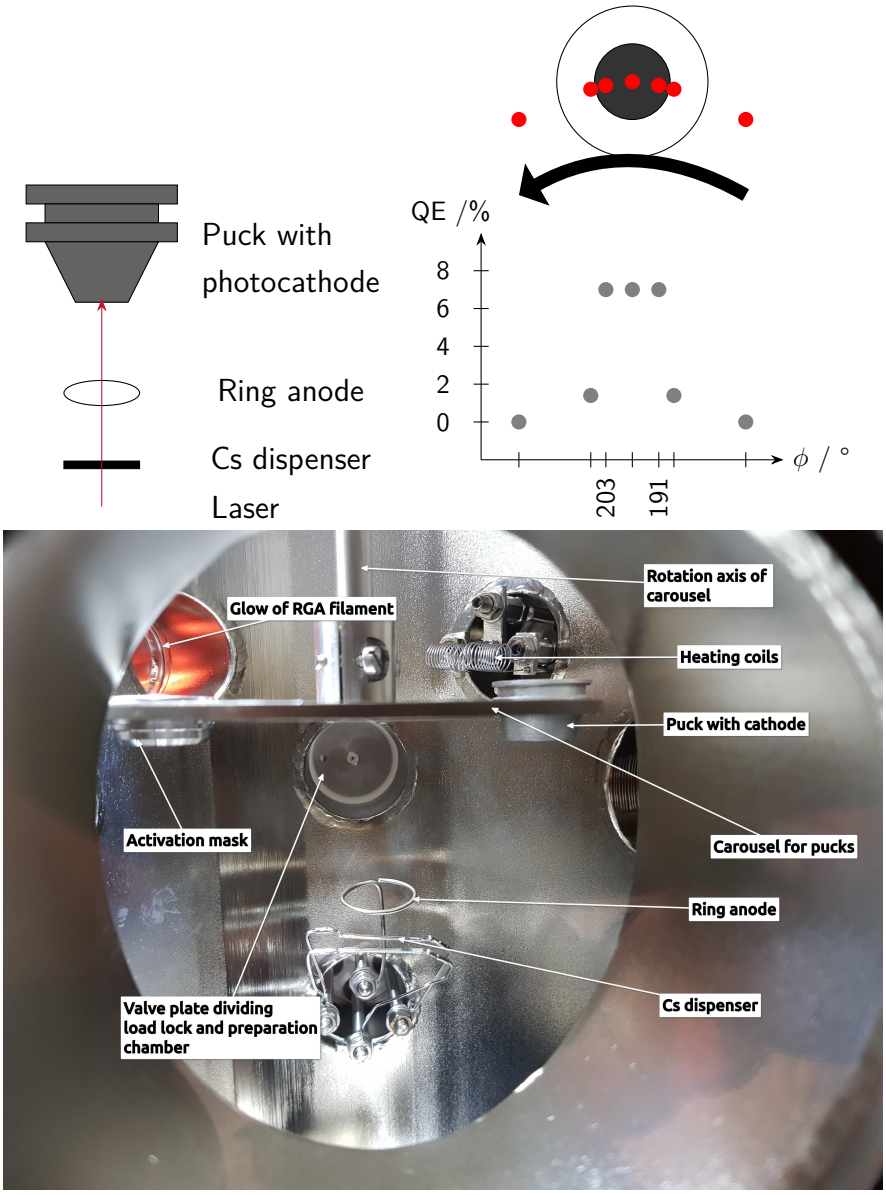

Figure 3.20.: *Sketch of the preparation arrangement is shown on the left. The molybdenum puck with the semiconductor is situated above a ring anode. The anode is set on a potential of 150 V in order to monitor the QE during activation. The Cs dispenser is below the anode, while the oxidizing gases are introduced through the load lock. On the right a bottom view of the puck is shown. The red dots indicate the laser spot position, while the cathode holder in the preparation chamber is rotated around its axis. The QE becomes maximal if the laser spot hits the freshly activated cathode. The numbers on the x axis are exemplary positions read from the manipulator used to rotate the cathode holder. Below both sketches a photograph of the inside is shown.*

With the ring anode on a potential of 150 V and a 674 nm laser diode with 150 µW photocathodes are prepared.

A further elaboration on the activation procedure is found in section 3.2. If this procedure is finished, the dispenser and anode voltage are disabled, the leak valves and the valve between load lock and preparation chamber are closed. Magnetic linear drives equipped with a fork like structure are used to grab and move the puck with the cathode to the source chamber. Therefor the valve between source chamber and preparation chamber has to be opened, and the elevator mechanism (refer to fig. 3.2) is positioned for the transport.

3.2. Preparation of photocathodes

As discussed in section 2.2 the photocathodes utilized in this study emit electrons when the surface is in the NEA state. This state is achieved through the co-deposition of caesium and an oxidizing agent (either oxygen or nitrogen trifluoride), a process outlined in this section. Figure 3.21 shows the arrangement of the leak valves on the load lock system for the preparation of photocathodes.

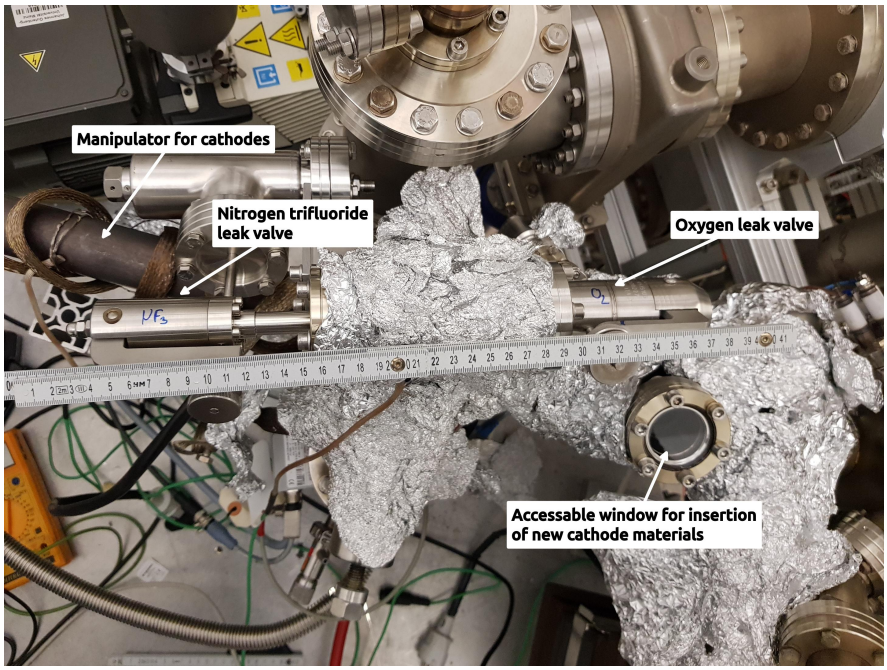

Figure 3.21.: *The photo depicts the installation of the leak valves on the load lock system. The two leak valves are connected via a CF40 tee onto an other CF40 cube.*

Initially, the puck containing the cathode is positioned beneath a heating element. Heating is conducted at 500 °C for 30 min to ensure a clean surface. Subsequently, the cathode is allowed to cool to room temperature for 45 min before being transferred into a preparation

mask. A preparation mask aids in creating a smaller active surface with a diameter of 3 mm thus enhancing the cathode's lifetime [32, 89]. A figure of the preparation mask is in fig. 3.22.

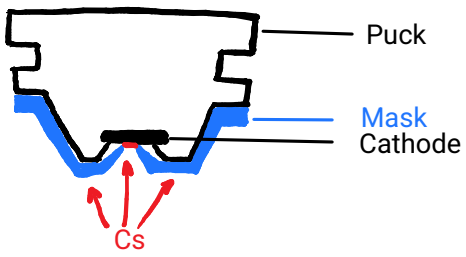

Figure 3.22.: *A sketch of the mask for preparation and its working principle. The mask (blue colored) only leaves a 3 mm diameter hole so that Cs and oxidizing agent can reach the photocathode surface through that hole. The rest sticks on the mask and does not contribute to the activation of the cathode material itself.*

Positioned above a Cs dispenser, the masked cathode [32] is illuminated by a laser with a wavelength of 674 nm and a power output of 150 µW. A ring anode placed between the cathode and the dispenser allows for voltage measurement, enabling monitoring of the preparation process. Figure 3.23 illustrates an exemplary preparation process. The blue points represent the QE, while orange line depict the signal of NF_3 in the Rest gas analyzer (RGA) in the preparation chamber during the process.

The initial peak of QE corresponds to the presence of only Cs on the surface since the activation starts typically with Cs only. If the QE begins to drop, the NF_3 valve is opened and the signal of the RGA rises up to 10^{-6}, particularly for the mass-to-charge ratio of 52, indicative of the NF_2^+ fragment. The QE gradually increases during this process, reaching 1.5 %. This activation process is called co-deposition. The short lived collapses are due to blockage of the laser beam. This blocking is done manually to verify the readings are produced by electrons emitted of the cathode. After 10 min to 20 min the QE begins to decrease which signals that the activation or preparation process concludes, and the cathode is removed from the mask and transferred into the source chamber for electron beam production.

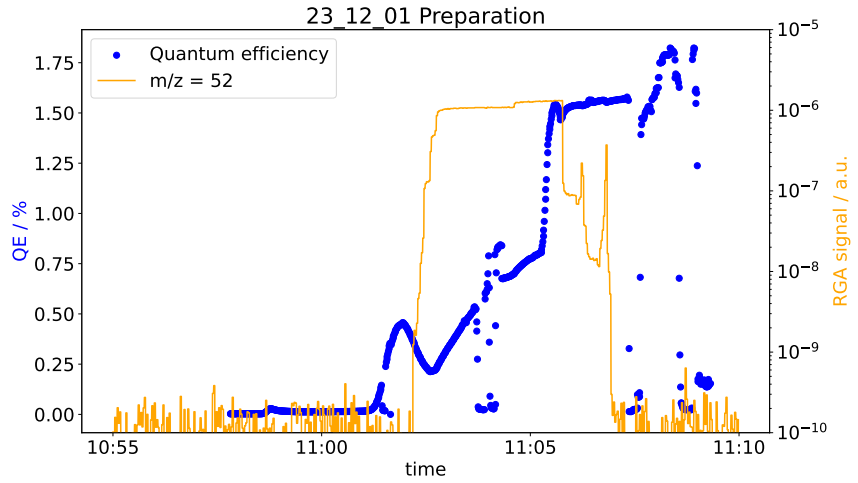

Figure 3.23.: *Exemplary preparation process of a superlattice cathode with NF_3 is shown. The blue points show the QE whereas the orange line shows the signal of NF_3 in the RGA in the preparation chamber during the preparation in arbitrary units.*

3.3. Implementation of the degradation process and its significance

During accelerator operation currents up to 20 µA at MAMI are extracted, while at MESA currents up to 150 µA are planned [3, 90]. Those high current operations significantly affect the QE and therefore the lifetime of a photocathode. It is suspected that the change of QE is correlated to the change of asymmetry, a procedure had to be implemented that ensures the QE degradation. This current is much larger then possible in the continuous Mott measurement.

The necessity for this separate step in the measurement arises from the dead time of 11 µs of the detectors and their operating point (refer to appendix A.2). The background noise left and right of the peak in the detector spectra shown in fig. 3.24 rises by one magnitude if the measurement current is risen in the same order of magnitude. In the right hand example spectrum the rise of a 200 keV peak can be observed.

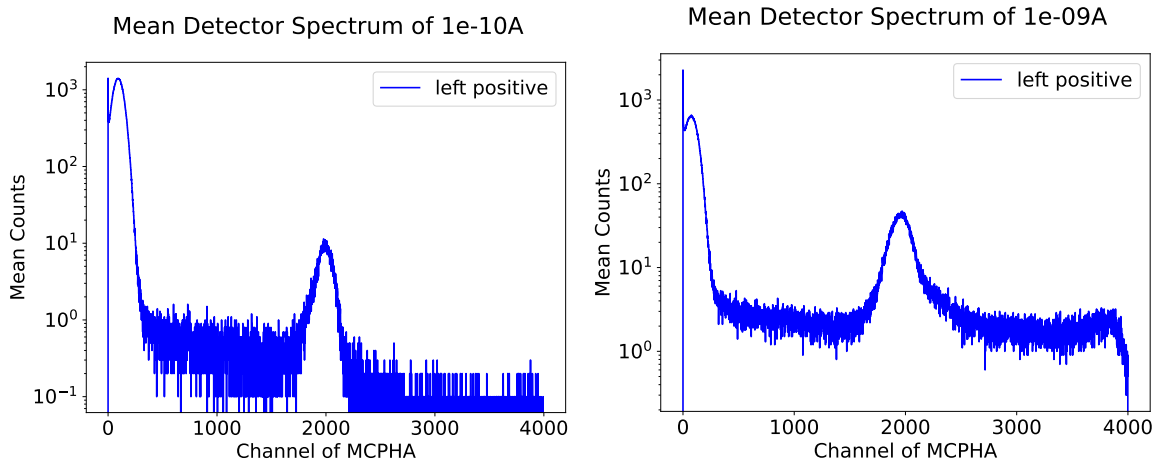

Figure 3.24.: *Two exemplary detector spectra are shown. The left spectrum is obtained with 100 pA primary current and the right one is obtained with 1000 pA. The main peak at channel centered around 2000 is the 100 keV signal of a back scattered electron. The signal of two electrons hitting the detector simultaneously is by far increased in the right spectrum.*

For Mott measurement the extracted current is constrained by the detecting system at 300 pA. At this region of current extraction, the lifetime of a cathode is dominated by the vacuum lifetime, which in the case of the PKA2 system is about 1000 h [74].

For this purpose, once every 24 h, a time frame of up to three hours is allocated to extract up to 180 mC of charge. This process, termed degradation of the photocathode, aims to replicate the conditions during accelerator operation, where Mott measurements are impossible in this specific setup.

There are two different modes of degradation: one mode with 1 µA at 300 V of source voltage, called low voltage mode and the other one, high voltage mode, with 100 keV. The difference in these two modes is the location of possible beam current losses. For the low voltage mode it was desired to loose the majority of the electron beam current in the periphery of the source, while the high voltage mode aimed to loose the beam in the Faraday cup behind the Mott polarimeter. The second mode simulates the operational conditions more closely to those in the high current operation for the accelerator. In table 3.2 the cathode and activation methods are shown with their degradation mode. Each degradation is characterized by its desired charge per day. If the QE of a cathodes is low enough that the initial degradation current could not be reached, current and extraction time have been adapted to compensate that.

Table 3.2.: *The different cathodes with their activation methods and their degradation modes are shown here. The desired degradation charge per day is shown too. The bulk cathodes have been degraded with higher currents due to their higher starting QE and therefore longer lifetime.*

Cathode	activation method	degradation mode	charge per day
bulk GaAs	Cs:NF_3	1 µA, 300 V	1.8 mC
superlattice GaAs	Cs:NF_3	1 µA, 300 V	1.8 mC
bulk GaAs	Cs:O_2	100 µA, 100 keV	180 mC
superlattice GaAs	Cs:O_2	1 µA, 100 keV	1.8 mC
bulk GaAs	Cs:O_2	100 µA, 100 keV	180 mC

The first two rows have been tests on the sensitivity of the photocathodes to the degradation process. The low voltage mode promised to create an environment in the source chamber that efficiently destroyed the NEA surface. Since the pumping speeds of the NEG modules and the ion getter pump directly attached, this effect was not observed. Instead it was decided to move to the high voltage mode for the degradation in order to be closer to real accelerator operation. The charge per day was adjusted to compensate for the order of magnitude differences in the starting QE to achieve roughly the same measurement time for each cathode.

Chapter 4

Measurement Techniques

This chapter is dedicated to the various methods the different data are acquired. It describes what parameters besides the asymmetry are observed, i.e. electron beam current, laser power and magnetic fields and where they are taken. In here the systematic errors are discussed; a discussion of each statistical error will be found in section 4.3.

4.1. Overview of the parameters tracked during measurements

During the long-term measurements, several experiment internal and external parameters have been tracked to ensure comprehensive data collection beyond just electron current and asymmetry. Internal parameters like the primary current and the electron beam currents after scattering can be tracked as well as the output power of the laser, the magnetic field in the exterior of the Mott polarimeter and the laboratory temperature. The influence of each parameter on the asymmetry is discussed as the parameter itself is discussed Figure 4.1 gives a schematic overview of the parameters and their position regarding the experimental setup.

Real-time evaluation of the incoming laser power on the cathode was facilitated using a photo diode power sensor[1] connected to an power and energy meter interface[2], which in turn is connected with Experimental Physics and Indutrial Control System (EPICS) for seamless data integration [91].

[1] S121C, Thorlabs. Specifications: 400 nm to 1100 nm wavelength range, 50 pW to 500 mW power range.
[2] PM100USB, Thorlabs. Specifications: 10 µW to 200 W measurement range.

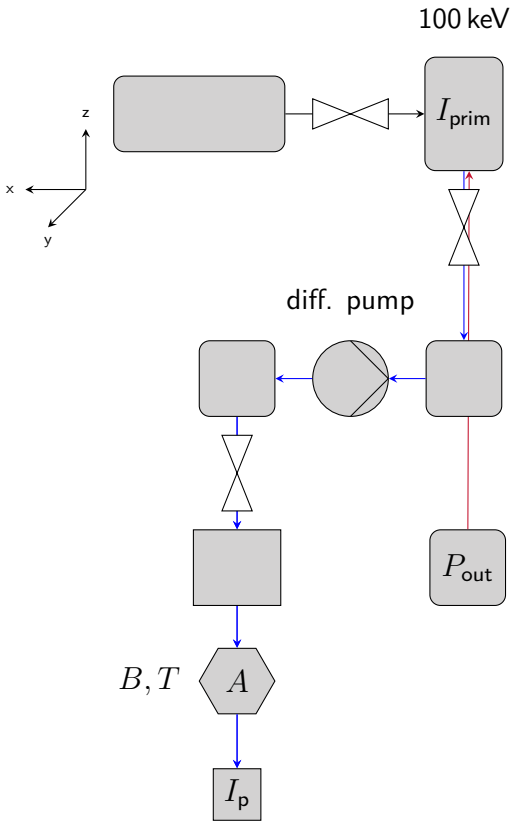

Figure 4.1.: *Overview of the tracked parameters during long term measurements. The primary current I_{prim} at the source, the laser output power P_{out} and at the Mott polarimeter the asymmetry A, the temperature and magnetic field components T, B and the parasitic current I_p are tracked. Figure analog to fig. 3.1.*

The laser power is a crucial parameter in the determination of the QE as seen in eq. (4.1). As discussed in section 3.1.6 the QE measurements are made in the medium intensity range, between 0.5 mW to 1 mW of laser power. During those measurements the laser power drifted less than 0.3 % from the initial set laser power, which one order of magnitude less than the statistical errors of laser power readout specifications [92].

Close to the Mott polarimeter, a fluxgate magnetometer[3], custom-built in-house, was positioned on top of the Mott polarimeter. This should give an idea of the changes of the magnetic field as close as possible to the gold targets. The three sensors face in all space coordinates for real-time magnetic field measurements Additionally, temperature sensors were integrated into the sensors for comprehensive environmental monitoring. These data

[3]DRV425 Fluxgate Magnetic-Field Sensor, Texas Instruments, measurement range from −2 mT to 2 mT with 50 nT resolution

have been included into the EPICS environment of the laboratory.

Magnetic fields, as discussed in section 3.1.3, influence the exact position of the electron beam spot on the target. Typically the magnetic field did fluctuate about 0.1 µT in all three dimensions. The typical values for the x, y, and z component has been 2.1 µT, 15.2 µT and 57.6 µT respectively. In order to shift the electron beam by one millimeter in either direction if the magnet is 2 m from the target one needs 0.5 mT [93]. The natural variation in the magnetic fields smaller than the required strength and therefore do not significantly influence the electron beam position, especially considering the analysis of the Mott polarimeter in section 3.1.5.

To monitor the current produced a digital voltmeter was installed in the shielding of the source. It is connected in series to the cathode via the high voltage. A camera was oriented on that digital voltmeter in order to read visually the current. This is done once a day before and after each degradation (refer to section 3.3) and the current values are stored together with the laser power information. Typical QE measurements have been performed with 150 nA in the laser power region between 0.5 mW to 1 mW as described in section 3.1.6. The values taken typically drifted in the last shown digit of the digital voltmeter, while the manufacturer gives a systematic uncertainty of 6 %.

Furthermore, the current in the Faraday cup, situated after the Mott targets, was monitored using an in-house built picoampere meter. This Faraday cup was integrated into the EPICS environment, allowing real-time data acquisition and storage. The systematic uncertainty for the picoampere meter is in the order of 3 %.

4.2. Explanation of the data collection methods and instruments used

The data acquisition process from the detectors of the Mott polarimeter has been adapted to read out the analog output signals of the detector system. Below is an explanation of how the signal is processed for evaluation with an overview of the different steps in fig. 4.2.

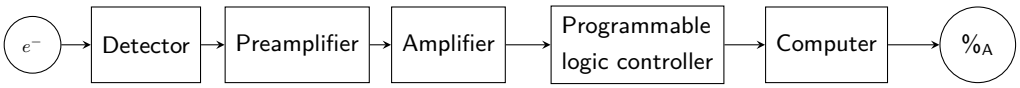

Figure 4.2.: *Scheme of the signal processing from electron to asymmetry. If an electron hits the detector, the signal gets pre-amplified and fed into an amplifier. This analog signal is fed into a programmable logic controller, which is transferred into the computer. This signal is then used for the data analysis and the asymmetry in its unit $\%_A$ is calculated.*

A backscattered electron hitting the semiconductor generates an electric pulse. This signal was pre-amplified within 5 cm behind the detector. Subsequently, another amplification step was implemented and this analog signal was read by a programmable logic controller. This was realized with a RedPitaya[4], a Field Programmable Gate Array (FPGA) based platform. This device was modified and used as a multi channel pulse height analyzer (MCPHA) for the purpose of detecting and processing signals [94]. The digital output of this detection and processing is a histogram of counts in different channels. Each detector produced its own histogram as each detector had its own input and output.

The resulting binary files contained the detector spectra of both detectors simultaneously, with an exemplary spectrum shown in an earlier section (refer to fig. 3.24). In order to obtain asymmetries this setup was able to switch the polarity of the Pockels cell voltage, thereby changing the helicity sign of the photons. The timing between switching the Pockels cell and the measurement is done with a Python script. Figure 4.3 illustrates a schematic of the script's working principle.

The script triggered the Pockels cell to switch to positive polarity and waits 0.2 s to be equilibrated [21, p.127]. After this delay the script triggers the MCPHA to histogram both detector events for one second and save the data. After that one second long measurement the script triggers the Pockels cell again but now to switch to negative polarity, wait the 0.2 s delay and start the histogramming with the MCPHA for one second again. If no interruption of this script has occurred the loop will continue by triggering again the positive polarity of the Pockels cell and the run would be completed while the new one has begun. There are two conditions where the stop flag is raised which would lead to a halt of the loop: either the desired run numbers are reached or the user stops the script with the appropriate method.

[4]RedPitaya, STEMlab 125-14, RedPitaya, 2016. Specifications: 10-bit ADCs, up to 125 MS/s, dual-channel, open-source platform.

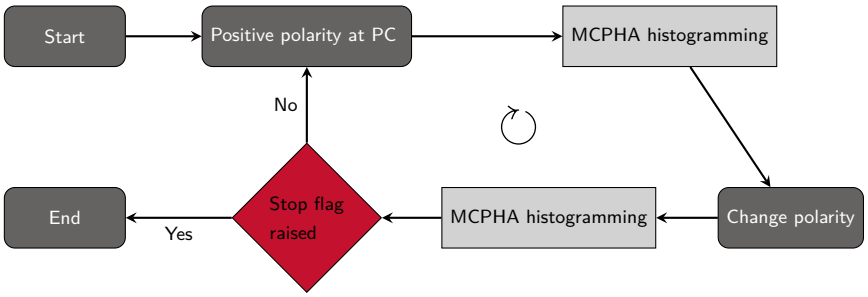

Figure 4.3.: *Basic steps of the measurement logic. The process begins by setting the Pockels cell (PC) to a positive voltage, initiating histograming of the MCPHA, switching the polarity, and histograming again. Subsequently, the process either ends if a stop flag is raised or continues with another iteration. The stop flag is raised if one interrupts the program manually or if the run number maximum is reached. Each completion of this cycle is referred as "run".*

The binary files produced have been analyzed by a separate Python script. In this program the histograms have been extracted, a peak finding algorithm marked the peaks and added these counts within a window. This number would be used to calculate the asymmetry as described in section 2.3. In fig. 4.4 the spectra of both detectors and the integration window in grey are shown. After that measurement has finished the Pockels cell is switched again and the same procedure follows for the negative voltage.

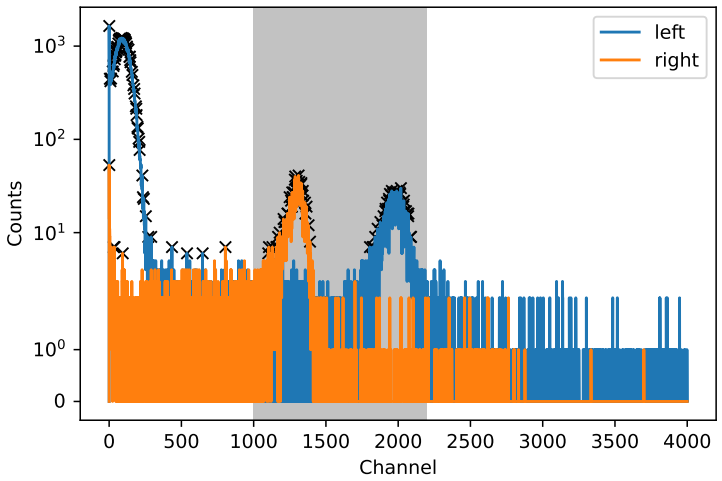

Figure 4.4.: *Spectra of both detectors are shown. The grey highlighted area represents the single integration window from channels 1000 to 2200, and the black markings denote the peaks identified by the peak-finding algorithm.*

Due to slight variations in gain, the peaks of both detectors on the MCPHA were not aligned in the same channels. This shift - since the main peak can only come from 100 keV

electrons - is negligible because the linearity of the detectors still is given. In section 4.3 fig. 4.8 a more detailed analysis of the influence of the integration window width is given. The influence of a smaller integration window is to be estimated as small as $1 \times 10^{-3}\,\%_{\mathrm{A}}$.

An analysis of the background and the signal itself shows a signal-to-noise ratio (SNR) of 21 for the low energy part ($<$ 100 keV) and an SNR of 33 in the higher energy part ($>$ 100 keV) as seen in fig. 4.5. The possibilities for electron energies higher than 100 keV in the experiment can only stem from two electrons hitting the detectors at the same time or noise from the detection system. Then the energy would be at 200 keV for two times 100 keV electrons. This process is viable at higher beam currents of 1 nA and upwards (refer to fig. 3.24 right side.) For the low energy part physics like electron-electron scattering and or inelastic interactions of the electrons can occur [84]. That leads to the conclusion that the SNR on the low energy part is lower due to physics while the broadening of the signal peak into the high energy part is due to noise and dead time effects. The dead time of the detectors is discussed in appendix A.2. Therefore the result for the SNR is in agreement with the expectation for the higher energies only being possible if multiple electrons hit the detector at the exact same time and therefore to be lower in noise and higher in the SNR.

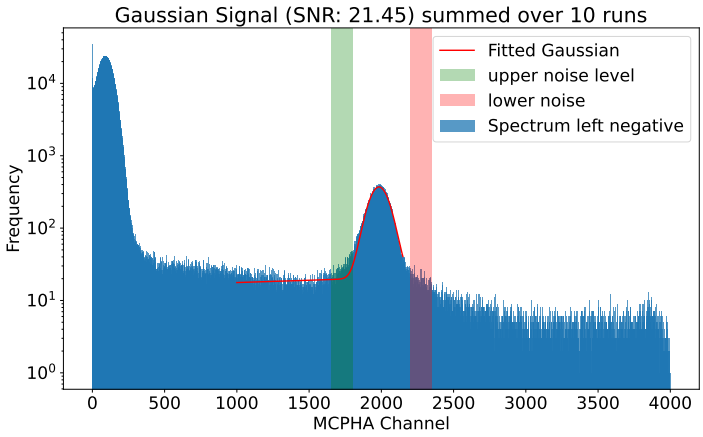

Figure 4.5.: *Exemplary SNR for the left positive detector setup. The signal to noise ratio is 21 for a Gaussian fitted peak on the low energy side (green) while the SNR for the high energy region (red) is 33. The green region contains noise from physics while the red region is noise due to electronics and dead time effects of the detectors.*

The red and green regions in fig. 4.5 indicate the regions where the SNR was determined from; if no electrons are directed into the Mott targets and therefore no backscattered electrons reach the detectors the events in the region of interest are as low as one or two events. Such empty spectra can be found exemplary in the appendix A.2.

4.3. Addressing limitations

Here statistical sources of uncertainties are discussed and an estimate of the gravity on the data will be given.

4.3.1. Experimental Setup

Beam positions have been checked once every day during the degrading process. The usage of zinc sulfide screen is widely accepted but it does not allow for high precision position determination as ZnS tends to overglow the actual electron beam spot. That gives an estimate on the beam diameter of 2 mm with no temporal information. Short lived changes of the position would not influence the measured asymmetry as much if those changes in beam position is within a range up to 2.5 mm from the initial center point (refer to fig. 3.12). In fig. 4.6 a typical beam spot is shown, which is moved to the far left of the screen.

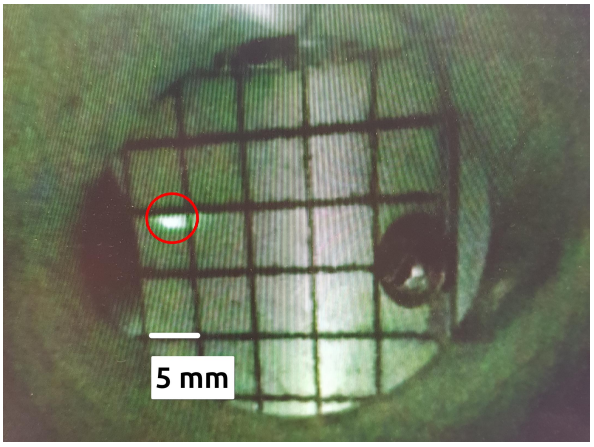

Figure 4.6.: *This image shows a photograph of the typical beam spot size on the ZnS screen in the Mott polarimeter. The grid has a lattice constant of 5 mm. The beam spot is circled in red and moved to the very left of the screen.*

4.3.2. Statistical measurement uncertainties

The uncertainty of the primary current is to be determined with 5 % as for the QE measurements high currents up to 150 nA are used in a short time of 5 s. During the asymmetry measurement the current is about 300 pA which is not within the accurate detection range of the current readout.

The laser power readout uncertainty is specified to be 3 % while the systematic intensity control is as accurate as 10 % [92]. Since the quantum efficiency is calculated according to eq. (4.1), the error propagation will result in an error of 5 %.

$$QE = \left(\frac{1.24I}{\lambda P_L}\right) \cdot 100 \tag{4.1}$$

with:

QE : QE in $\%_{\mathrm{QE}}$
I : current in nA
λ : wavelength of the laser in nm
P_L : Laser power in µW.

The uncertainties of the escape probability are propagated from the uncertainties of the QE since the material constants of the electron diffusion length l (eq. (2.4)) and the absorption coefficient α are systematic uncertainties. As those uncertainties are quite large (refer to section 2.1.2), they do not interfere with the aim of this work. As described in eq. (6.3) the QE is directly proportional to the P_{esc} and therefore the uncertainty of P_{esc} is 5 %.

The uncertainties of the asymmetries are mainly determined by the counting statistics of the detectors. With a mean count rate m of 4500 s^{-1} the uncertainty Δm can be described with Poisson statistic in eq. (4.2):

$$\Delta m = \sqrt{m} \approx 65.57\,\mathrm{s}^{-1} \tag{4.2}$$

By using the Gaussian error propagation eq. (5.4) one can calculate the error of one single asymmetry to 0.79 % as described in section 5.1.2. In the very same chapter is was described that the asymmetries have been grouped together, therefore one can weigh the uncertainty of each group with g as the number of measurements within each group with (according to [95]) eq. (4.3):

$$\sigma_{A,w} = \frac{\sigma_A}{\sqrt{g}} \approx 6 \times 10^{-3}\,\%_{\mathrm{A}}. \tag{4.3}$$

That means that one group containing from 16 000 to 60 000 single asymmetries it can be achieved a statistical accuracy of $6 \times 10^{-3}\,\%_{\mathrm{A}}$.

4.3.3. Data analysis uncertainties

In all fits the errors are given from the covariance matrix as the squared of the diagonal elements. As goodness of fit the reduced chi squared (χ^2_{red}) as introduced in eq. (5.3) was used, where only the errors on the y axis is regarded.

The usage of a large integration window allows for robustness regarding the peak maximum of the 100 keV backscattered electrons. In fig. 4.7 an example of the peak maximum channel position (CH) during a long term run is shown. The peak maximum mean is made for each group and the relative change is calculated according to $(\overline{CH} - CH_i)/CH_i$ while X is a measured value and $\overline{CH}$ is the mean value. For each detector count rate N_i the relative changes are shown.

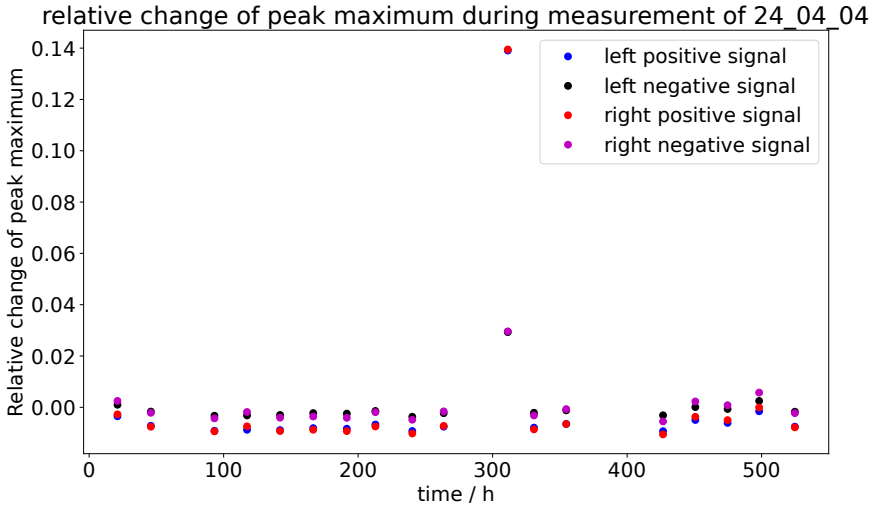

Figure 4.7.: *The relative channel position change of the 100 keV peak maximum over time is shown. A significant shift in peak position at around 300 h resulted from an error in the measurement restart protocol. Once corrected, the data returned to the expected values.*

The variances are small with respect to the width of the peaks. The peak full width half maximum will be shown to be at 114 channels for a σ of 50 channels when fitting a Gaussian on the peak (see e.g. fig. 4.5).

The difference in using one large integration window versus two smaller integration windows does influence the calculated asymmetries in the third decimal. In fig. 4.8 histograms for both integration methods are shown. The mean value for the double window method is 6.5198 $\%_A$ while for the single window the mean value of the asymmetry is 6.5171 $\%_A$ in this specific test scenario. The relative difference is approximately 0.04 %, whereby this error belongs to the systematic errors and not to the statistical errors.

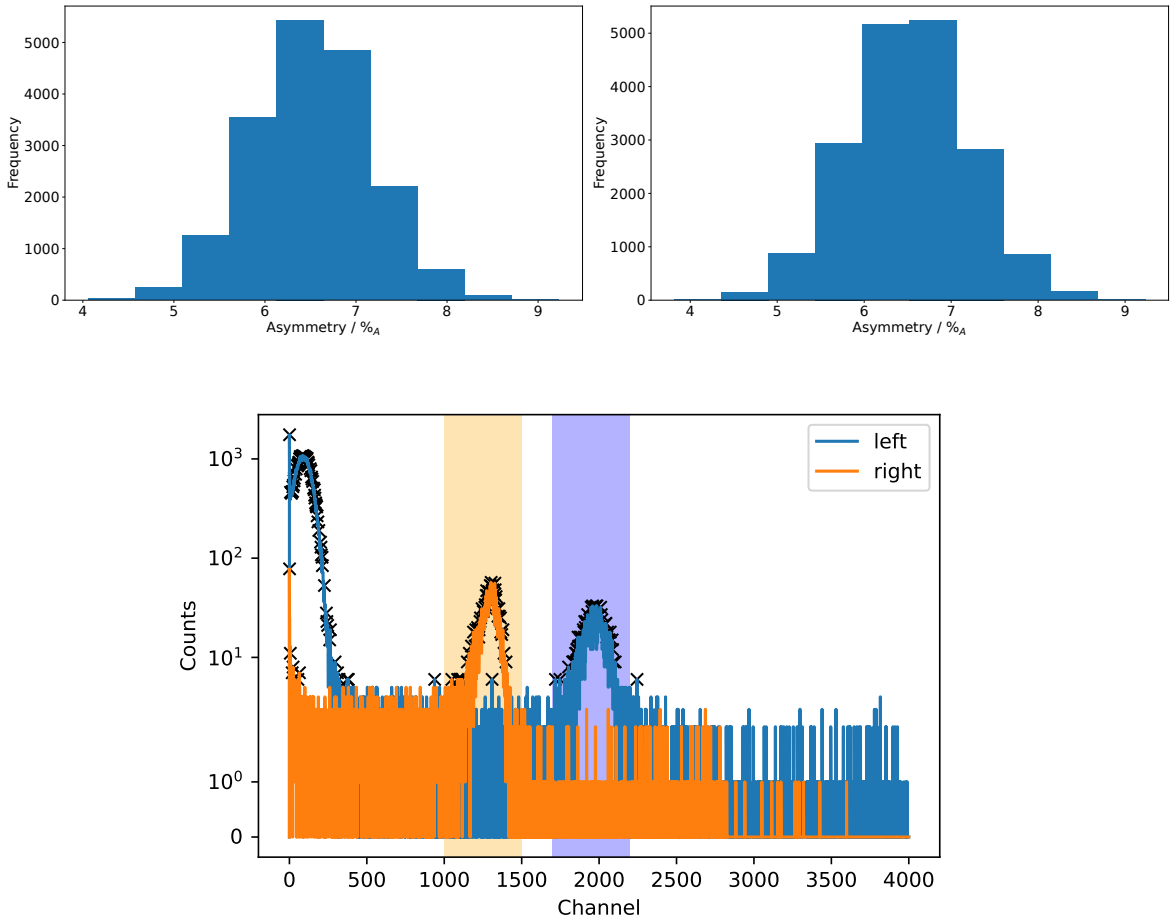

Figure 4.8.: *Histograms of the asymmetries calculated with one single integration window (left) and two separate integration windows (right). The mean asymmetry is to be found for both integration methods at 6.51 $\%_A$. See fig. 4.4 for the single window reference and the lowest figure for the double integration window, the regions are marked in the same color as the spectra.*

In order to save computational power of this specific implementation the integration of the 100 keV peak is made by add up all events within the integration window. A benchmark with a Gaussian fit for each peak found the same area to a 3×10^{-2} % difference level. The peak position monitoring was performed by a peak finding algorithm which was adjusted to find the peaks of the 100 keV electron within the integration window.

An analysis of the integration window width is shown in fig. 4.9. The obtained asymmetries are plotted versus the window width given in channel numbers. This analysis was made specifically for the double integration window case and shows that the asymmetries stabilize at a window width of 1470 channels. The double window width in fig. 4.8 is 500 channels wide, while the peak centers are around 250 away from the integration borders. The standard

deviation of the asymmetries is shown as bars in fig. 4.9 and stabilizes at 570 channels of integration window width. Example detector spectra with their respective integration windows are to be found in the appendix A.3. The single integration window is 1200 channels wide and spanned from channel 1000 to 2200, which avoided the region of the 200 keV peak around channel 2500.

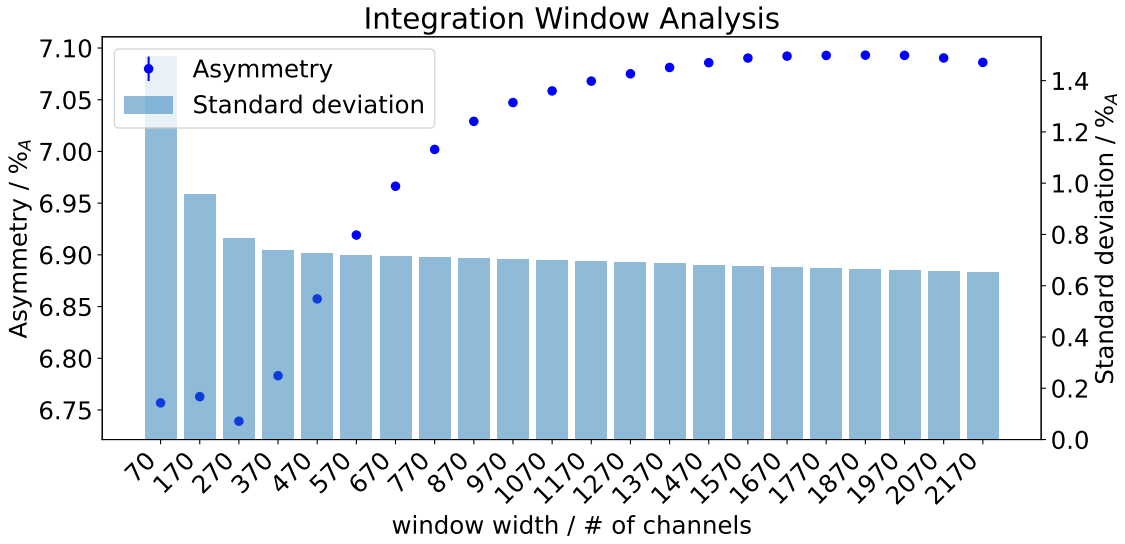

Figure 4.9.: *The asymmetry is plotted in respect to the double integration window width. It stabilizes at a width of 1470 channels. The standard deviation is also shown as bars for each asymmetry. The standard deviation stabilizes already at 570 channels.*

Since the integration window was kept constant throughout every measurement this also accounts only to systematic errors rather than the statistical errors.

4.3.4. Polarization measurements

As described in section 3.1.5 a polarization calibration was attempted. Therefor the different targets have been used to measure the asymmetry. In fig. 4.10 the asymmetry is plotted versus the target thickness. Even with an estimate of 5 % error for the thicknesses, the difference in asymmetry between the target position 1 and 2 cannot be explained.

Regarding the asymmetry it was concluded that target 2 has to be much thinner than given. As explained the combined count rate was therefore used in order to extrapolate to zero. The targets used are thick so that multiple scattering of electrons within the targets are possible. The error for the polarization is calculated according to Gaussian error propagation by using

the eq. (2.6) rearranged to the polarization and use A_0 as the asymmetry extrapolated to zero thickness and S_{th} the theoretical Sherman function for eq. (4.4):

$$\Delta P = \sqrt{\left(\left(\frac{1}{A_0}\right)\cdot \Delta A_0\right)^2 + \left(\left(-\left(\frac{{A_0}^2}{S_{th}}\right)\right)\cdot \Delta S_{th}\right)^2} = 10\,\% \tag{4.4}$$

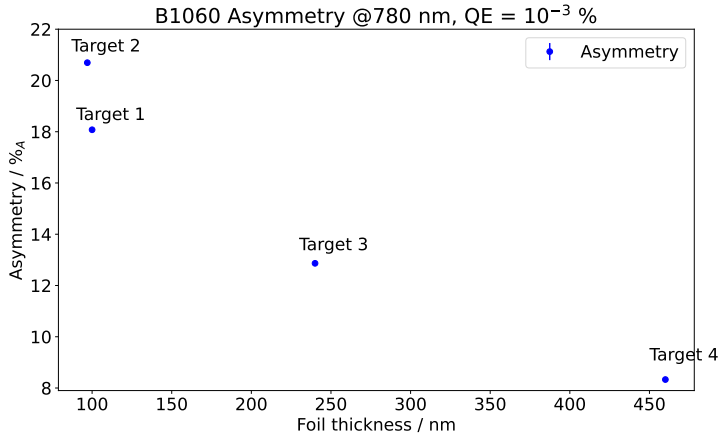

Figure 4.10.: *The measured asymmetries are shown for each target thickness. The asymmetries for the 99.5 nm and 96.9 nm are too different for a difference in thickness of 2.6 nm. Therefore a different approach has been conducted in order to obtain the polarization. The target number equals the numbering in table 3.1.*

The theoretical Sherman function for 100 keV is 0.3975 with a precision of 1 %[85]. With an estimated error for A_0 of 4.6 $\%_A$ the overall error of the polarization is in the order of 10 % for the three point fitting in fig. 3.13.

4.3.5. Cathode materials

Both cathodes examined in this work have very different histories prior to the work. The bulk cathode has been used with oxygen activation numerous times while the superlattice cathode has been native before. It is known that especially oxygen will react with the surface of the semiconductor so that the initial QE of each activation goes down [56]. Nitrogen trifluoride is commonly used in semiconductor industry in order to clean the surface of wafer materials [96, 97].

Chapter 5

Data Analysis

In this chapter the data analysis is described. For the sake of clarity all steps are shown on one particular data sets, that has no extra ordinary features but shows the most relevant feature, the change of asymmetry over time. For the results see section 6.3.

5.1. Data processing and workflow

In section 4.2 a description has been presented of how the electrons produce the signal that is then converted into the asymmetry as described in section 2.3. For the analysis Python 3.8.17 has been used with the libraries NumPy 1.24.3 and Pandas 1.5.3 for handling the data, Matplotlib 3.6.3 and Seaborn 0.12.2 for plotting and SciPy 1.10.1 for fitting the data.

5.1.1. Linear and Gaussian Fit

Two main mathematical functions have been defined: a linear regression following the equation eq. (5.1)

$$f(x) = mx + b \tag{5.1}$$

where:

m : slope of linear function
b : y-axis intercept

and a Gaussian function following the equation eq. (5.2):

$$f(x) = A \exp\left(-\frac{(x-\mu)^2}{2\sigma^2}\right) \tag{5.2}$$

where:

A : scaling factor, e.g. amplitude
μ : mean or expected value
σ^2 : variance.

The statistical method of a χ^2_{red} has been defined as follows:

$$\chi^2_{\text{red}} = \frac{1}{N - n_{\text{free}}} \sum \left(\frac{f(x)_{\text{fit}} - y_{\text{data}}}{y_{\text{err}}} \right)^2 \tag{5.3}$$

where:

N : the number of datapoints
n_{free} : number of free parameters, neglegible if N is big
$f(x)_{\text{fit}}$: value found by the fit
y_{data} : actual measured value
y_{err} : error of measured value.

If the error values are not given then the equation eq. (5.3) is simplified by setting the error equal to one and is only the χ^2. The χ^2_{red} gives an approximation to the goodness or a reasonableness of a fit. The closer the value to one the better the fit and its underlying hypothesis [95, p.82-83].

5.1.2. Reading the asymmetries

As explained in section 3.3 every 15 h to 24 h the degradation has been done. Therefore groups of runs are formed consisting between 16 000 to 60 000 single asymmetries. A run is as defined in fig. 4.3 and yields both detector spectra for both polarization states of the Pockels cell. To save some computational power for this specific implementation, after each group the count rates are collected and the asymmetries according to eq. (2.8) are calculated. For each asymmetry the error is calculated with error propagation eq. (5.4):

$$\sigma_A = \sqrt{\sum_{i=1}^{4} \left(\frac{\partial A}{\partial N_i} \Delta N_i \right)} = \frac{\sqrt{Q}}{(1+\sqrt{Q})^2} \left(\sum_{i=1}^{4} \frac{1}{N_i} \right)^{1/2} \tag{5.4}$$

where:

σ_A : error of asymmetry
$\frac{\partial A}{\partial N_i}$: derivative of A with respect to each detector count
N_i : count rate of i th detector, e.g. count rate of left detector with positive Pockels cell voltage etc.

These data are used to compute a histogram where the bins are calculated with the Freedman Diaconis Estimator [98]. The bin centers are used as data point for a Gaussian fit (refer to eq. (5.2)). The fitting method is a least squares algorithm and provides the covariance matrices for error estimation on the fit. The Gaussian fit provides the mean value for the zeroth order approximation which states a constant asymmetry over time. A histogram and the fit function is plotted for a group of runs and is shown in fig. 5.1.

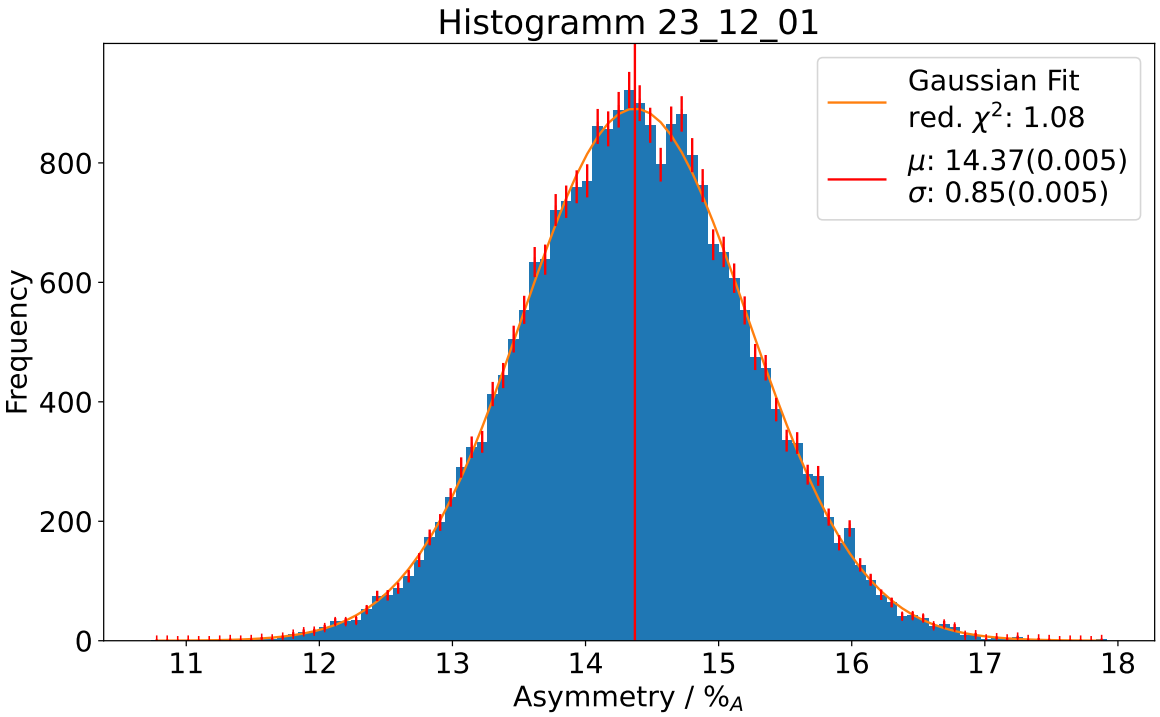

Figure 5.1.: *Example histogram in blue of a group (in this case a 23 h measurement without interventions, i.e. a period without any asymmetry drifts) of superlattice GaAs with fitted Gaussian distribution in orange. The red vertical line indicates the mean value of this fit. The red stripes on top of the histogram bars are the error bars of each bin. The goodness of the fit was determined as χ^2_{red} in eq. (5.3). The σ parameter of this Gaussian distribution corresponds to the error of a single asymmetry, which is in the order of 0.8 $\%_A$.*

5.1.3. Time dependent plotting

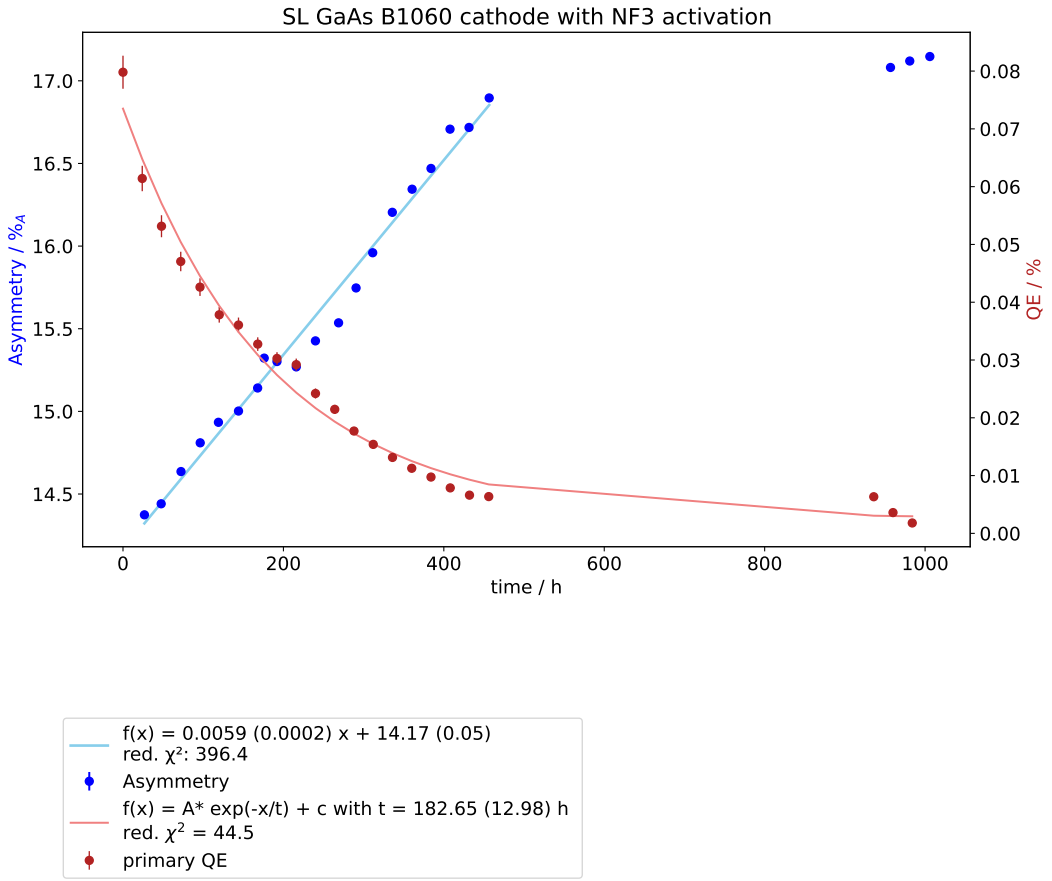

Figure 5.2.: *The time dependent plot of asymmetry and QE. The blue dots indicate the measured asymmetry of each group with error bars significant smaller than the dots used as representation. In light blue a linear regression to the data have been fitted. The red dots are the QE, many of them also have an error bar smaller than the dot. The gap in these data between 500 h to 900 h are a break of measurement. No high voltage was applied and all the valves have been closed during this break. The QE and asymmetry did not change significantly during this break. The systematic errors of the QE are not included in this graph.*

The subsequent phase involves plotting the time-dependent effects on asymmetry and the quantum efficiency against time. The aforementioned groups have been averaged and a linear regression as described in eq. (5.1) has been performed, while the QE has been fitted exponentially and both are plotted as shown in fig. 5.2. Additionally the QE was calculated from a file that contained the primary current and the laser power and the QE was plotted alongside the asymmetry.

5.1.4. Correlation analysis

With the time dependent data at hand a statistical test has been performed which is presented in this section. For clarity the same data set as before is used to show how the data have been evaluated. The in depth discussion is found in section 6.1.

Together with the environmental data as described in section 4.1 a simple correlation analysis has been performed. It was chosen to perform a Spearman´s Rank correlation. The advantage of the Spearman's Rank is that it is nondirectional, i.e. it does not assume which variable is the dependent one [99]. The result is a matrix in which each entry represents the correlation coefficient. It is generally accepted that a significance larger than 0.5 corresponds to a large effect strength [100]. In fig. 5.3 the lower half of the correlation matrix is shown. Since those matrices are diagonal one could focus only on one half.

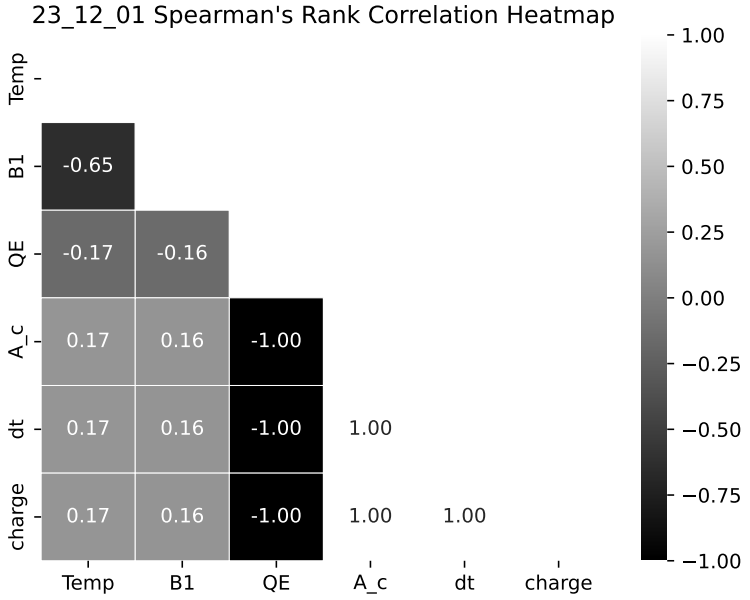

Figure 5.3.: *The exemplary Spearman's Rank correlation matrix from a dataset of a 20 d long time run is shown. The gray scale signifies the different signs in correlation: the darker the color the more negative correlated are the variables; the lighter the color the more positive correlated. A grey color signifies a very weak correlation.*

The strong anti correlation between temperature and magnetic field is surprising since the used device is stated to have fluxgate sensors. According to [101] those sensors are reported to be quite temperature independent with $0.1\,\mathrm{nT}\,^{\circ}\mathrm{C}^{-1}$.

Chapter 6

Discussion

Here the findings are discussed and all concepts previously explained are used in order to verify these findings. In this chapter the discussion of the hypothesis, the results and their interpretation can be found.

6.1. Review of existing hypotheses of the correlation of asymmetry and quantum efficiency

The literature does discuss two possible explanations for the asymmetry dependence on the QE. Those are summarized by Saez [102] as follows:

The first mechanism can be describes as **filtering mechanism**. The mobility of the electrons is heavily influenced by the doping concentration as seen in eq. (6.1) [103]. Higher doping concentrations will lead to lower mobility of the electrons [20, p.40]. The mobility of any charged particle in a semiconductor can be approximated as:

$$\mu_i \propto \frac{T^{3/2}}{\sqrt{m^*} D_i} \tag{6.1}$$

with:

μ_i : Mobility of charged particle due to impurities
m^* : effective electron mass
D_i : ionic impurity density
T : temperature.

Factors like temperature, lattice scattering, and for heavy doped GaAs the scatting on optical phonons, are influencing the mobility of the electrons [16, 20]. For bulk cathodes the absorption length of the light is much larger than the electron diffusion length, therefore the excitation of electrons from energetically deeper bands is more prevalent, especially since the used laser of 808 nm provides an excess of excitation energy of 110 meV. The same does not hold true for superlattice cathodes as their absorption length is much larger than

their active zone as described in fig. 2.4. Also since the band gap is different from the bulk cathode there is no excess in photon energy.

With high QE the energy level of the vacuum lies relatively low so that electrons can be emitted even if they loose a bit energy on their way to the semiconductors surface. The energy got lost during the different scattering paths like BAP or DP. The EY depolarization mechanism, which also involves scattering on phonons, is largely suppressed in the cathode materials used (refer to section 2.4). If those electrons are emitted the polarization is lower if the QE is high. The energy level of the vacuum is rising, if the QE decays and electrons with lower energy now are trapped in the band bending region. They have to recombine with the conduction band and cannot contribute to the polarization. This effect is briefly sketched in fig. 6.1 a) and b).

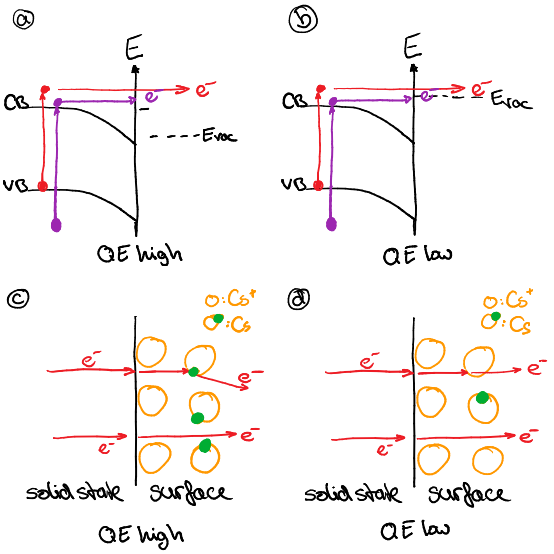

Figure 6.1.: *A visual summary of the two main processes that contribute to the depolarization while the quantum efficiency degrades.*

The second discussed effect can be described as **surface scattering**. Here the scattering of the electrons also takes place at the surface of the semiconductor. Electrons interact with the adsorbed atoms that constitute the NEA surface, leading to scattering events [104]. Additionally, electrons originating from the semiconductor may undergo scattering at the nucleus of the adsorbed atom. It is postulated that the polarization P is dependent on the amount of scatterer n on the surface via eq. (6.2):

$$P(n) = P_{\text{bulk}} \exp(-\sigma n) \tag{6.2}$$

where:

P_{bulk} : polarization from photo emission
σ : exchange scattering cross section
n : amount of scatterer on the surface in cm^{-2}

This hypothesis is supported by the argumentation that caesium compounds have high ionic character and therefore caesium is willingly giving its single electron in the out most orbital [22]. A graphical representation is found in fig. 6.1 c) and d).

6.2. Anticipated trends - Hypothesis

Following these two different explanations one can anticipate the following trends from the measured data:

If the filtering mechanism is dominating, the dependency on the different cathode materials should be prominent. That is because in bulk-GaAs the mobility is much lower due to the high doping concentration of $1 \times 10^{19}\,\text{cm}^{-2}$ Zinc as doping atom [42]. As for superlattice one wants to make the band bending zone as small as possible, by creating a thin (typically 5 nm) but very high doped ($1 \times 10^{19}\,\text{cm}^{-2}$) layer on top. Following the eq. (6.1) one finds that the mobility of electrons in the superlattice material is about a factor of five higher than in the bulk material because the active zone is low in doping concentration ($1 \times 10^{17}\,\text{cm}^{-2}$ with beryllium atoms [29]).

This mechanism was favoured by Saez and also Liu et al. [102, 105]. The first author argued that because the effect of higher polarization is higher in strained material, it is to be concluded that the filtering effect has to be stronger. In the second work it is also concluded that the filtering effect is stronger since during the activation process they found a saturation of polarization dependency. They suspect that the band bending zone is more likely to cause the change in polarization than the activation layer.

As for the surface scattering effect, the different oxidizing agents could be expected. In Liu et al. and Erbudak and Reihl [104] it has been discussed weather the thickness of the activation layer has an influence on the ESP. While Erbudak and Reihl argues that the valence electron of the second caesium layer does influence the polarization, in Liu et al. this is only supported by the Cs-only activation. If one would expect an effect it would show

to some degree in the usage of the different oxidizing agents. Since caesium and oxygen will react to some extend on the surface, the electron of the Cs will be taken by the oxygen. On the other hand NF_3 will not react with the Cs and therefore will not take the valence electron. This is supported by the studies of Liu et al. in which a similar decay constant of nitrogen and fluorine was detected but not for caesium [52]. They conclude from their photo electron emission spectroscopy that nitrogen trifluoride does not react with the surface.

Overall the surface scattering effect should be very small for thermal drift velocities. Even though the differential cross sections for Cs in the low energy region up to 2 eV is large, the asymmetry parameter for the elastic scattering process on the nucleus is near zero up to opening angles of 50° [106].

6.3. Results

Both cathodes, the bulk and the superlattice cathodes have been activated with Cs:NF_3 and Cs:O_2 and measured for at least 250 h. Each long term measurement was analyzed as described in section 5.1. The initial suspected parameter that influences the asymmetry was the QE, which was confirmed by analyzing the correlation matrices. In figs. 6.2 and 6.3 the time depended plots for the bulk cathodes and superlattice cathodes are shown. In fig. 6.2 right side the effect of an overdose of caesium during the preparation. The QE dropped rapidly within the first roughly 75 h and after that it rises again to the initial QE and a bit higher. After a 75 h period of stable QE it begins to decay as expected. This behaviour of photocathodes has been observed in other accelerators as well [107].

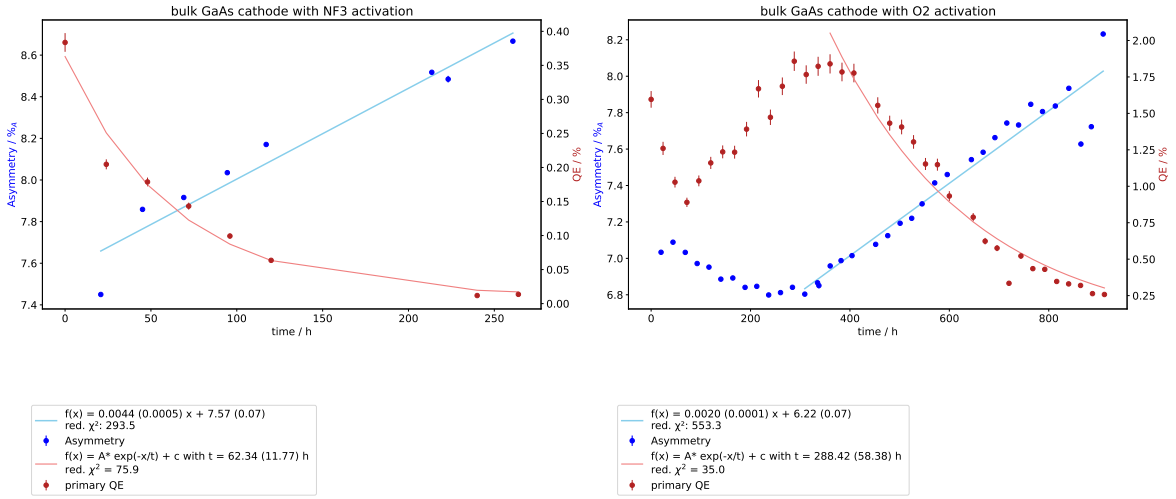

Figure 6.2.: *The time dependent plots of the bulk GaAs cathodes with NF_3 (left) and oxygen preparation (right). The red curve and points describe the QE while the blue curve and points describe the asymmetry. The curves indicate fits that have been attempted in order to describe the time dependent evolution. The large error bar in the left figure first QE point is a result of reading error. On the right hand side the cathode was overcesiated and therefore the QE dropped and rose before it finally decayed at around 350 h mark.*

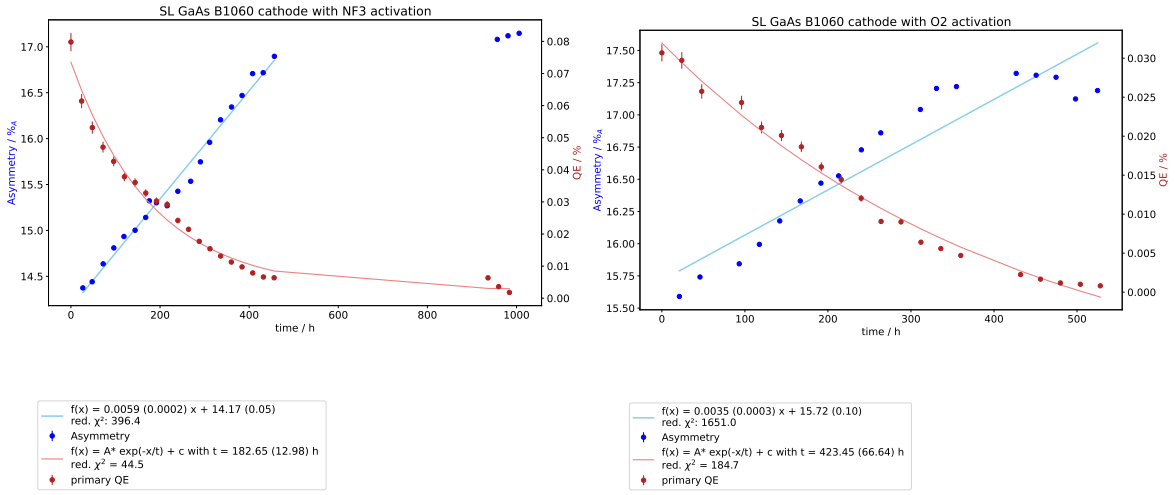

Figure 6.3.: *The time depended plots of the superlattice GaAs cathodes with NF_3 (left) and oxygen preparation (right). The red curve and points describe the QE while the blue curve and points describe the asymmetry. The curves indicate fits that have been attempted in order to describe the time dependent evolution. The gap in the left figure is due to a break in measurement while the high voltage was off and the valves have been closed. During this break time no significant changes in either QE nor asymmetry have been observes which indicates a long vacuum lifetime.*

The correlation matrix was calculated with Spearman´s Rank which does not infer a linear relationship between variables, and it was found that the magnetic field correlated to all tracked parameter very weakly (found correlation coefficient between -0.28 to 0.69), also the temperature did not correlate with other parameters. On the other hand the quantum efficiency, asymmetry and extracted charge strongly correlated (found correlation values of -1 for QE and asymmetry while 1 for asymmetry and charge). Since the QE does give an estimate on the photocathode NEA condition it was recalculated in to the dimensionless property of P_{esc} according to eq. (6.3):[105]

$$P_{\text{esc}} = \left(1 + \frac{1}{\alpha l}\right) \frac{QE}{1 - R} \tag{6.3}$$

with

α : absorption coefficient
l : electron diffusion length
QE : quantum efficiency
R : reflectivity.

In section 2.1.2 a detailed discussion about the parameters influencing the P_{esc} has been done. The two examined cathode materials, bulk GaAs and the GaAs based superlattice, mainly differ in their respective electron diffusion length. While for the bulk cathode the diffusion length is in the order of 400 nm, the superlattice cathode is limited by its structural parameters of the active zone. The low doping concentration in the active zone leads to higher electron mobility and hence to higher electron diffusion length (in the order of micrometers). But the structural parameters of the superlattice is in the order of 100 nm thus confining the electron diffusion length to that number. Therefore every electron that gets excited in the superlattice cathode can travel to the surface and has one chance to escape the semiconductor. This makes the QE equivalent to the probability of photon absorption $W_{\text{abs}} = \alpha l$. Recalling that the escape probability can simplified to $P_{\text{ecs}} = QE/\alpha l$, because $1/\alpha l \approx 10$ which is much larger than one.

The errors are calculated with the known Gaussian error propagation formula.

To make comparisons between the different cathodes and activation methods more readable the asymmetries have been converted into their relative changes according with the minimal measured asymmetry A_{min} (eq. (6.4)):

$$\frac{\Delta A}{A} = \frac{A - A_{\text{min}}}{A_{\text{min}}} \tag{6.4}$$

The resulting fig. 6.4 is shown with two different fitting models supporting the filtering effect, because the change of asymmetry is more pronounced in the superlattice material than in the bulk cathode. The two modeling approaches provide a starting point in the investigation of the asymmetry behaviour, given the sparse literature description.

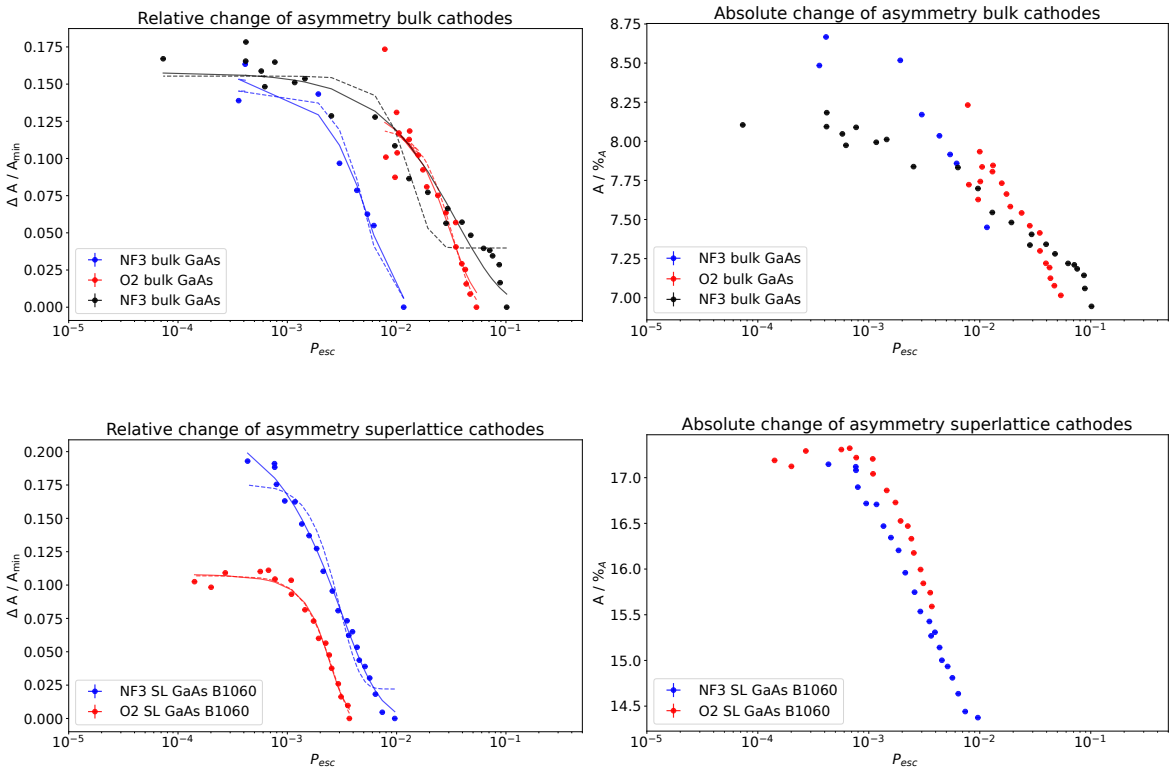

Figure 6.4.: *The relative change of asymmetry is plotted versus the escape probability (P_{esc}) is presented for the bulk cathodes (top) and for the superlattice (bottom). For each data set two fits are shown: the Fermi-Dirac statistic (solid line) and the Boltzmann CDF (dashed line). On the left hand side the relative changes of the asymmetries are shown while on the right hand side the absolute asymmetries are shown for each cathode material.*

The work of Orlov et al. suggest two energy states within the band bending zone found the derivative spectra of photo emitted electrons near the band gap [108]. Those two energy states can act as trapping states for electrons to relax into. If the electrons relax they will scatter which will result in polarization losses. If the NEA is lower than those states and hence the escape probability is higher, electrons still could tunnel through the barrier and contribute to the overall lower measured asymmetry. If the NEA is changing towards positive electron affinity (PEA) (lower escape probability) the electrons cannot tunnel through the barrier and therefore do not contribute to the overall measured asymmetry. This will result in a rising measured asymmetry. This concept is visualized in fig. 6.5

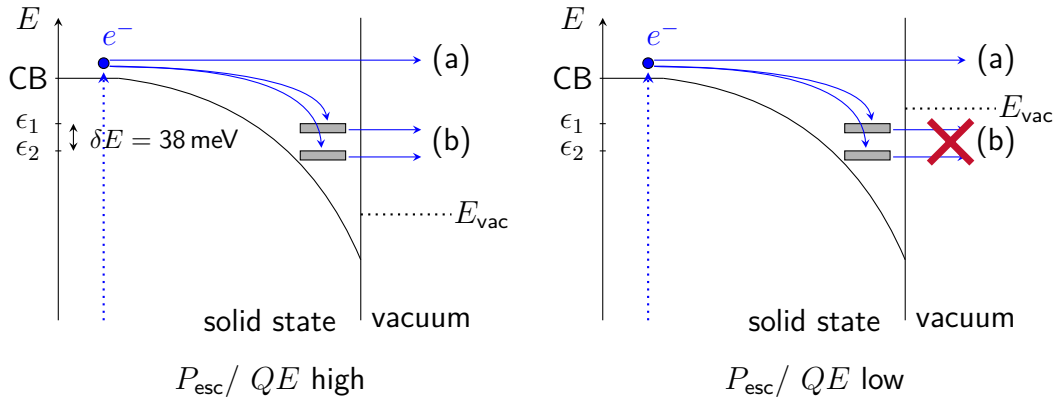

Figure 6.5.: *A schematic visualization of the filtering effect. Within the band bending zone two energy states with 38 meV difference from the conduction band each, are postulated which can act as traps for electrons which are to be emitted. If the NEA is more pronounced than electrons in those states still can escape while if the transition towards PEA happens, it is not feasible anymore. On the left hand side P_{esc} is high so hot electrons (a) and thermalized electrons (b) can be emitted, while on the right hand side the P_{esc} is low and only hot electrons (a) can be emitted. Thermalized electrons are captured in the band bending zone.*

In fig. 6.4 one can see that there seems to be a saturation of the relative change of asymmetry, beginning at escape probabilities around 1×10^{-3}. For higher P_{esc} a rapid change of asymmetry is observed. In order to describe that behavior, two mathematical models have been fitted to those data: a Boltzmann like distribution and a Fermi-Dirac statistic. Both are capable to describe such curve progression and are presented in the following.

For the Boltzmann like distribution the Maxwell-Boltzmann distribution, which is a result of the kinetic gas theory, initially describes the velocities in an ideal gas with free moving particles [109]. From those distributions the derivation towards the energy distribution via the momentum space can be done. The measured asymmetry in this work are to be thought to be influence by the energy distribution of the photo emitted electrons considering all the energy states in which depolarization can happen. The measurement of asymmetry by varying the QE can be expressed as the measurement of the integral of said distribution because the lower integral boundary, the energy level of the vacuum, shifts towards higher energies. Therefore instead of taking the probability density function of the Maxwell-Boltzmann distribution the cumulative distribution function (CDF) is used as fit function as the CDF is the integral of the probability density function [110, p.85]. This distribution especially the CDF which is defined according to eq. (6.5):

$$CDF(x) = \mathrm{erf}\left(\frac{x}{\sqrt{(2)}k_BT}\right) - \sqrt{\left(\frac{2}{\pi}\right)}\frac{x}{k_BT}\exp\left(\frac{-x^2}{2(k_BT)^2}\right) \tag{6.5}$$

with

erf : the error function.

The eq. (6.6) gives the fit function based on eq. (6.5) where the variable x is the QE and the $CFD(x)$ is the measured asymmetry A:

$$A(QE) = b\left(\mathrm{erf}\left(\frac{QE}{\sqrt{2}a(k_BT)}\right) - \sqrt{\left(\frac{2}{\pi}\right)}\frac{QE}{a(k_BT)}\exp\left(\frac{-(QE)^2}{2(a\cdot k_BT)^2}\right)\right) + c \tag{6.6}$$

where a, b and c are free fit parameters.

Due to unit considerations, it must be assumed that the QE is proportional to an energy scale in order to move from eq. (6.5) to eq. (6.6). In a first approximation, this energy scale might be the electron affinity, for instance. The Boltzmann CDF is considered suitable in this context due to the nature of the experimental setup and the observed data trends. As the measurement continuously decreases the escape probability, the asymmetry is observed to change in a manner that can be described by the integral of a distribution. In this case, the proposed distribution is the Boltzmann distribution. This is because, if one were to take the derivative of the Boltzmann CDF, it would yield a Boltzmann (probability) distribution, which is characterized by its ability to describe the probabilistic distribution of states in a system [110]. This mathematical framework aligns well with the experimental data, where the asymmetry changes gradually, reflecting the underlying statistical mechanics of the system.

Boltzmann describes the system in a classical way, where temperatures are in the region of room temperature unlike the sigmoidal distribution which could be linked to the Fermi-Dirac statistic. The Fermi-Dirac statistic is defined in eq. (6.7) [111, 112]:

$$n_i = \frac{g_i}{\exp\left([\epsilon_i - \mu]/k_BT\right) + 1} \tag{6.7}$$

where

n_i : average number of fermions in state i
g_i : degeneracy of states
ϵ_i : energy of state i
μ : total chemical potential.

This distribution gives the average numbers of fermions (e.g. electrons) in a single particle state and assumes that the fermions are not interacting. The Fermi-Dirac statistic leads to an energy distribution which can be translated to measured asymmetry as explained in the Boltzmann CDF. A density of states can be expressed if the function is rewritten with the Fermi function [113]. All of these lead to a continuous function for the asymmetry in respect to the QE ($A(QE)$) which is used a fit function as in eq. (6.8):

$$A(QE) = \frac{a}{\exp\left(\frac{b\cdot[QE-c]}{k_B\cdot T}\right)+1} \tag{6.8}$$

where

a, b, c : free fit parameter
k_B : Boltzmann constant
T : absolute temperature, fixed at 300 K.

The temperature was fixed at 300 K because all measurements are made at room temperature. The total chemical potential μ was substituted with the QE in order to go from eq. (6.7) to eq. (6.8). It is assumed that the QE is proportional to an energy scale, as it has been done with the Boltzmann CDF. This time the energy scale has to be combined with the Fermi energy plus the potential energy of an electron. The parameter c in eq. (6.8) which substitutes the energy of the state i in eq. (6.7) is only known for bulk GaAs; the definitions of the states ϵ_1 and ϵ_2 from fig. 6.5 are made in respect to the energy level of the conduction band in the bulk [108]. Until now such measurements have not been done to superlattice cathodes. The Fermi-Dirac statistic approaches the Maxwell-Boltzmann statistic (which describes the overall assumption behind Maxwell-Boltzmann distributions) in (a) the case of low particle density and (b) the high temperature region. The Fermi-Dirac statistic typically is better suited to describe semiconductors at room temperature and at high doping concentrations [113, p.246-248]. The Fermi-Dirac distribution explains a more quantum mechanical behaviour, i.e it is based on Pauli's exclusion principle and catches sharp transitions, transitions with a steep gradient over a narrow P_{esc} range, at lower temperatures much better. The Boltzmann CDF covers a smoother and broader

transition, without considering the exclusion principle. The transition in question would be, in first order approximation, from NEA to PEA which would reflect on the overall measured asymmetry.

As Erbudak and Reihl stated, PEA cathodes would not suffer from drastic changes in polarisation (i.e. measured asymmetry in the context of this work) and therefore one should better operate spin polarized electron sources in the PEA region [104]. For bulk GaAs cathodes it is claimed that the PEA surface condition is reached at quantum efficiencies of 0.1 % [114] which would agree with a escape probability of 10^{-3}. This can be found as a saturation effect in the data for the bulk cathodes with good agreement.

For the superlattice cathodes it is not reported so far at which point the NEA turns into PEA. Regarding the data acquired a threshold of escape probability of up to 10^{-4} can be made. But in terms of QE this would correspond to 0.01 %. Since superlattice photocathodes are much thinner than the bulk material the diffusion length from eq. (6.3) corresponds to the thickness of the active zone of those materials. For superlattice this length is 100 nm while for bulk GaAs it is in the order of half a micrometer [25].

Both models have additional parameters a, b, c for optimization. It is important to note that both models cannot represent their original interpretation since they are used in the context of escape probability and asymmetry change; they are used to find a mathematical description.

The interpretation which model fits better regarding fig. 6.4, can only be done in a qualitative way until now. For the superlattice cathode the Fermi-Dirac approach (solid line) seems to match the curve progression better, especially at the high QE region. The bulk cathode is much broader in the distribution of the data point but the nitrogen trifluoride preparation also seem to better fit with the Fermi-Dirac approach. The wider scatter of the bulk cathode data is supported when the absolute values of the asymmetry values are plotted against the escape probability (right side of fig. 6.4).

These differences in the sharpness of the transitions can be explained because the superlattice cathodes are much thinner than the bulk cathodes and therefore the depolarizing effects of the BAP process are very much suppressed. That leaves only the DP process as the main contributor to the depolarizing mechanism. Going to lower P_{esc} will lead to maximum polarization as seen in fig. 6.6.

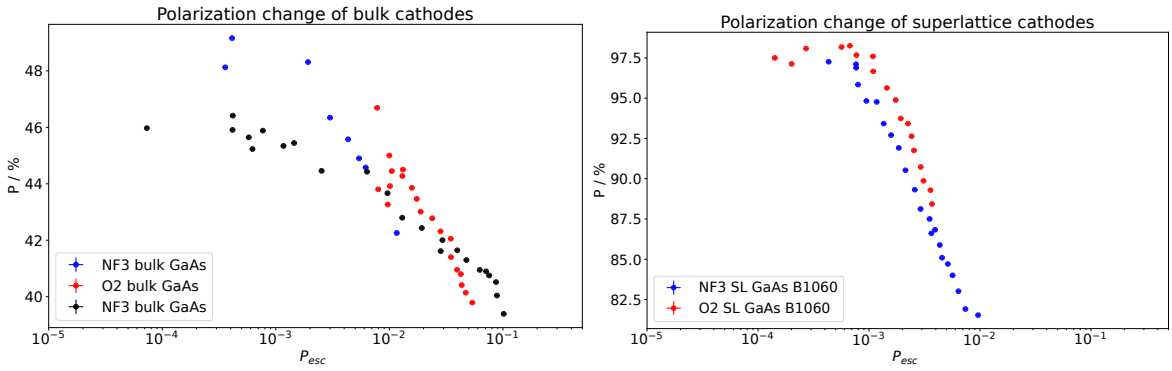

Figure 6.6.: *Polarization is calculated with the obtained polarization value from fig. 3.13. The calculated effective Sherman function obtained is 0.1763. The left side show the polarization of bulk cathodes and on the right side the polarization is shown for the superlattice cathodes.*

The bulk cathodes reach very near their theoretical polarization maximum of 50 %. If the P_{esc} is low the surface will reach the PEA state, where the energy level of the vacuum is just above the conduction band level (refer to fig. 2.7). Due to the long absorption length of up to 1 µm [115], the electrons which are excited deep in the crystal will not reach the surface and are depolarized by the processes DP and BAP. In order to still be emitted the electrons need to be excited at the very near of the surface so that the excess energy provided by the laser is sufficient. Since these near surface electrons experience a very low diffusion they also experience less depolarization and therefore are nearly undisturbed if they leave the semiconductor. The low P_{esc} will lead to a virtual thin bulk photocathode, allowing for maximum polarization of 50 %.

The superlattice cathode is already a thin photocathode in respect to the absorption length which is one, but not the sole reason, why the polarization is inherently larger than for bulk cathode. By lowering the P_{esc} to the PEA state of the surface the DP, as the remaining depolarization process, is suppressed to a level that electrons now can be emitted nearly undisturbed. This will lead to the theoretical polarization maximum of 100 %. The cost for such yield is very low QE of 10^{-2} % which will not provide high intensity electron beams without powerful laser systems.

Chapter 7

Conclusion and Outlook

This work aimed to provide an understanding in the long term behavior of electron spin polarized photocathodes and tried to find explanations for any observed behavior. Therefore the asymmetry which is directly proportional to the ESP was measured over the course of 250 h at least for each activation and each photocathode. This research is important to enhance the high precision experiments of P2 at the new accelerator MESA which aims to measure the weak mixing angle.

To measure the asymmetry, an existing independent photo electron source was equipped with a Mott polarimeter. Operating at 100 keV, this setup reduced the complexity of the machine compared to a full-grown accelerator while containing all the necessary components for precise asymmetry measurements. A load lock system enabled the use of two different cathodes and two different oxidizing agents for preparation in a dedicated vacuum chamber. This setup, a proven concept from the MAMI accelerator, is now also implemented at MESA.

This setup was used to investigate bulk GaAs photocathodes and superlattice photocathodes with two different oxidizing agents NF_3 and O_2 in order to find a possible relationship between the measured change of asymmetry and the activation process. Each cathode was investigated for long term stability especially looking into the changes of asymmetry if the quantum efficiency changed. In order to replicate accelerator conditions the cathodes underwent a degradation process that extracted typically 3.6 mC to 180 mC each 24 h block. With these data correlation between QE and asymmetry was found and further investigated. By using the escape probability as a more generally interpretable size of the QE the relationship between the relative change of asymmetry and the P_{esc} is discussed.

A significant contribution of this work is the development and testing of two models to describe the relationship between asymmetry and P_{esc}. The first model employs a Boltzmann cumulative distribution function (CDF), which fits better for the bulk system and suggests a classical behavior of the ESP. The second model uses a Fermi-Dirac statistic which molds better to the superlattice system, indicating a steeper gradient from NEA surface state to PEA surface state. The modeling approach is a new effort in the field, providing the first mathematical framework to describe these behaviors quantitatively.

The two possible explanation for the increase of asymmetry in respect to P_{esc} have been a surface scattering effect and a filtering effect. The surface scattering effect assumed that emitting electrons interact with the surface atoms respectively with their electrons and therefor loose polarization. As this cross section is quite large, other parameter determining the scattering probability are very close to zero. Therefore one could exclude the surface scattering effect as a large contributor to the initial polarization loss.

On the other hand the filtering effect, which is mainly supported by the idea of having electronic states in the band bending zone, was found to be good candidate. As elaborated those states can trap electrons where they undergo depolarization processes. If the P_{esc} is high those electrons still can escape the solid state and contribute to a decreased measured asymmetry. As the degradation goes on the P_{esc} decreases and trapped electrons cannot tunnel through the barrier anymore, hence the increase of measured asymmetry. The measurements provide a hint that with sufficient low QE the depolarizing effects on the surface vanish and the eq. (2.9) simplifies to:

$$P_{\text{exp}} = P_{\text{abs}} \cdot P_{\text{trans}} \cdot P_{\text{theo}} \tag{7.1}$$

where the effects of the absorption P_{abs} and transport P_{trans} influence the experimentally measured polarization P_{exp}. As those influences tend to be in the region of a few percent [116], the measured polarization in fig. 6.6 are reasonable.

Valuable information, like the actual order of the atoms on the GaAs surface, can be acquired if in situ use of surface characterization can be implemented. A candidate for such analysis would be a scanning tunneling microscope (STM) as it is very sensitive to the surface with atomic resolution. The tunneling current can give information not only on the spatial chemical composition, it would also give information about the energy of the surface once calibrated. Such work has been started by Biswas et al. in order to look at the NEA surface of GaAs while heat cleaning the surface from Cs adsorbed atoms [117]. Other groups also used the STM to investigate the surface during activation of photocathodes and measured the local work function on the surface, while investigating which ordering of the Cs atoms provide the best reduction of the work function for electron emission [118, 119]. Such work can provide a more precise statement as to when the surface transitions from the NEA state to the PEA state.

This works made it clear that the change of asymmetry is directly linked to the change of QE which makes it very important to have online polarization measurement of the electron beam at high precision in order to perform successful experiments at MESA for P2.

Chapter 7

Bibliography

[1] E. Curie, *Madame Curie : A Biography* (Bermann-Fischer, 1937).

[2] W. Gerlach and O. Stern, "Der experimentelle Nachweis der Richtungsquantelung im Magnetfeld", Z. Med. Phys. **9**, 349–352 (1922).

[3] D. Becker, R. Bucoveanu, C. Grzesik, et al., "The P2 experiment: A future high-precision measurement of the weak mixing angle at low momentum transfer", Eur. Phys. J. A **54**, 1–61 (2018).

[4] D. Simon, "Gesamtkonzept für den MESA-Teilchenbeschleuniger unter besonderer Berücksichtigung von Strahloptik und Kryogenik", PhD thesis (Johannes Gutenberg Universität, 2021).

[5] S. Schlimme, K. Aulenbacher, S. Baunack, et al., "The MESA physics program", (2024).

[6] K. Wille, *Physik der Teilchenbeschleuniger und Synchrotronstrahlungsquellen* (Vieweg+Teubner Verlag, 1992).

[7] M. Tigner, "A possible apparatus for electron clashing-beam experiments", Il Nuovo Cimento **37**, 1228–1231 (1965).

[8] J. Kessler, *Polarized Electrons*, 2nd ed. (Springer-Verlag, 1985).

[9] P. Souder and K. D. Paschke, "Parity violation in electron scattering", Frontiers of Physics **11**, 111301 (2016).

[10] D. Griffiths, *Introduction to elementary particles* (John Wiley & Sons, 2008).

[11] H. V. Klapdor-Kleingrothaus and A. Staudt, *Teilchenphysik ohne Beschleuniger* (Vieweg+Teubner Verlag, 1995).

[12] R. L. Workman et al., "Review of Particle Physics", PTEP **2022**, 083C01 (2022).

[13] J. Reinhold, *Quantentheorie der Moleküle* (Springer Fachmedien Wiesbaden, 2015).

[14] S. H. Simon, *The Oxford Solid State Basics*, 1st ed. (Oxford University Press, 2013).

[15] K. Momma and F. Izumi, *VESTA 3 for three-dimensional visualization of crystal, volumetric and morphology data*, Dec. 2011.

[16] H. Ehrenreich, "Band Structure and Electron Transport of GaAs", Phys. Rev. **120**, 1951–1963 (1960).

[17] D. J. Erskine, A. J. Taylor, and C. L. Tang, "Femtosecond studies of intraband relaxation in GaAs, AlGaAs, and GaAs/AlGaAs multiple quantum well structures", Applied Physics Letters **45**, 54–56 (1984).

[18] M. Walter, H. Häkkinen, L. Lehtovaara, et al., "Time-dependent density-functional theory in the projector augmented-wave method", J. Chem. Phys. **128**, 244101 (2008).

[19] J. J. Mortensen, L. B. Hansen, and K. W. Jacobsen, "Real-space grid implementation of the projector augmented wave method", Phys. Rev. B **71**, 35109 (2005).

[20] S. Sze and K. K. Ng, *Physics of Semiconductor Devices* (Wiley, Oct. 1969).

[21] K. Aulenbacher, "Erzeugung intensiver hochpolarisierter Elektronenstrahlen mit hoher Symmetrie unter Helizitätswechsel", Habilitation (Johannes Gutenberg-Universität, 2007).

[22] W. Gasteyer, "Untersuchung zum Elektronenemissionsprozeß von III-V-Halbleiter-Photokathoden mit negativer Elektronenaffinität", PhD thesis (Johannes Gutenberg-Universität, 1988).

[23] M. B. Panish and H. C. Casey, "Temperature Dependence of the Energy Gap in GaAs and GaP", Journal of Applied Physics **40**, 163–167 (1969).

[24] K. Aulenbacher, "Eine Quelle longitudinal polarisierter Elektronen für das MAMI-Beschleunigersystem", PhD thesis (Johannes Gutenberg-Universität, 1994).

[25] N. Scahill, "Self-modulation of photoemitted bunches at the picosecond timescale", PhD thesis (Johannes Gutenberg-Universität Mainz, 2022).

[26] H. Asai and K. Oe, "Energy band-gap shift with elastic strain in $Ga_xIn_{1-x}P$ epitaxial layers on (001) GaAs substrates", J. Appl. Phys. **54**, 2052–2056 (1983).

[27] Y. A. Mamaev, A. V. Subashiev, Y. P. Yashin, H. J. Drouhin, and G. Lampel, "Energy resolved spin-polarized electron photoemission from strained GaAs/GaAsP heterostructure", Solid State Commun. **114**, 401–405 (2000).

[28] T. Saka, T. Kato, T. Nakanishi, et al., "Spin-polarized electron sources with GaAs–GaAsP superlattices for surface analyses", Surface Science **454-456**, 1042–1045 (2000).

[29] T. Maruyama, D. A. Luh, A. Brachmann, et al., "Systematic study of polarized electron emission from strained GaAs/GaAsP superlattice photocathodes", Appl. Phys. Lett. **85**, 2640–2642 (2004).

[30] M. Fox and R. Ispasoiu, "Quantum Wells, Superlattices, and Band-Gap Engineering", in (Springer US, 2006).

[31] H. S. Im, C. S. Jung, K. Park, et al., "Band Gap Tuning of Twinned GaAsP Ternary Nanowires", The Journal of Physical Chemistry C **118**, 4546–4552 (2014).

[32] K. Aulenbacher, V. Tioukine, M. Wiessner, and K. Winkler, "Status of the polarized source at MAMI", AIP Conf. Proc. **675**, 1088 (2003).

[33] T. Maruyama, A. Brachmann, J. Clendenin, et al., "A very high charge, high polarization gradient-doped strained GaAs photocathode", Nucl. Instrum. Methods Phys. Res., Sect. A **492**, 199–211 (2002).

[34] E. O. Kane, "Thomas-Fermi Approach to Impure Semiconductor Band Structure", Phys. Rev. **131**, 79–88 (1963).

[35] E. F. Schubert, *Doping in III-V Semiconductors* (Cambridge University Press, Sept. 1993).

[36] U. Weigel, D. Orlov, S. Kosolobov, et al., "Cold intense electron beams from LN2 -cooled GaAs-photocathodes", Nucl. Instrum. Methods Phys. Res., Sect. A **536**, 323–328 (2005).

[37] J. Schaber, R. Xiang, and N. Gaponik, "Review of photocathodes for electron beam sources in particle accelerators", J. Mater. Chem. C **11**, 3162–3179 (2023).

[38] W. E. Spicer and A. Herrera-Gomez, "Modern theory and applications of photocathodes", in Spie´s 1993 international symposium on optics, imaging and instrumentation, edited by K. J. Kaufmann (Oct. 1993), p. 18.

[39] H. R. Philipp and H. Ehrenreich, "Optical Properties of Semiconductors", Phys. Rev. **129**, 1550–1560 (1963).

[40] S. Sze and J. Irvin, "Resistivity, mobility and impurity levels in GaAs, Ge, and Si at 300°K", Solid-State Electronics **11**, 599–602 (1968).

[41] H. C. Casey and F. Stern, "Concentration-dependent absorption and spontaneous emission of heavily doped GaAs", Journal of Applied Physics **47**, 631–643 (1976).

[42] Wafer Technology Ltd., *Gallium-Arsenide*, 2024.

[43] W. E. Spicer, "Photoemissive, Photoconductive, and Optical Absorption Studies of Alkali-Antimony Compounds", Phys. Rev. **112**, 114 (1958).

[44] S. Friederich, "Entwicklung einer hochbrillanten Photoemissionsquelle für spinpolarisierte Strahlen", PhD thesis (Johannes Gutenberg-Univeristät Mainz, 2019).

[45] H. J. Drouhin, C. Hermann, and G. Lampel, "Photoemission from activated gallium arsenide. I. Very-high-resolution energy distribution curves", Phys. Rev. B **31**, 3859 (1985).

[46] T. Wada, T. Nitta, T. Nomura, M. Miyao, and M. Hagino, "Influence of Exposure to CO, CO2and H2O on the Stability of GaAs Photocathodes", Jpn. J. Appl. Phys. **29**, 2087–2091 (1990).

[47] N. Chanlek, J. D. Herbert, R. M. Jones, et al., "The degradation of quantum efficiency in negative electron affinity GaAs photocathodes under gas exposure", Journal of Physics D: Applied Physics **47**, 055110 (2014).

[48] W. Liu, "Study of Advanced Photocathodes for Highly Polarized Electron Source Polarized electron source", PhD thesis (University of Chinese Acadamy of Sciences, 2017).

[49] P. B. Henderson and A. J. Woytek, "Fluorine Compounds, Inorganic, Nitrogen", in *Kirk-othmer encyclopedia of chemical technology* (Wiley, Dec. 2000).

[50] A. Holleman and E. Wiberg, *Lehrbuch der anorganischen Chemie / Holleman-Wiberg*, 34th ed., Vol. 101 (1995).

[51] C. Y. Su, W. E. Spicer, and I. Lindau, "Photoelectron spectroscopic determination of the structure of (Cs,O) activated GaAs (110) surfaces", J. Appl. Phys. **54**, 1413–1422 (1983).

[52] Z. Liu, Y. Sun, S. Peterson, and P. Pianetta, "Photoemission study of Cs-NF3 activated GaAs(100) negative electron affinity photocathodes", Appl. Phys. Lett. **92**, 241107 (2008).

[53] N. Chanlek, J. D. Herbert, R. M. Jones, et al., "High stability of negative electron affinity gallium arsenide photocathodes activated with Cs and NF3", J. Phys. D: Appl. Phys. **48**, 375102 (2015).

[54] M. Gussoni, M. Rui, and G. Zerbi, "Electronic and relaxation contribution to linear molecular polarizability. An analysis of the experimental values", Journal of Molecular Structure **447**, 163–215 (1998).

[55] T. M. Miller and B. Bederson, "Atomic and Molecular Polarizabilities-A Review of Recent Advances", in (1978), pp. 1–55.

[56] N. Chanlek, "Quantum Efficiency Lifetime Studies using the Photocathode Preparation Experimental Facility Developed for the ALICE Accelerator", PhD thesis (University of Manchester, 2011).

[57] T. J. Gay and F. B. Dunning, "Mott electron polarimetry", Rev. Sci. Instrum. **63**, 1635–1651 (1992).

[58] E. Rutherford, "The scattering of α and β particles by matter and the structure of the atom", London Edinburgh Philos. Mag. & J. Sci. **21**, 669–688 (1911).

[59] N. F. Mott, "The scattering of electrons by atoms", Proceedings of the Royal Society of London. Series A, Containing Papers of a Mathematical and Physical Character **127**, 658–665 (1930).

[60] N. Sherman, "Coulomb Scattering of Relativistic Electrons by Point Nuclei", Phys. Rev. **103**, 1601–1607 (1956).

[61] G. Holzwarth and H. Meister, "Elastic scattering of relativistic electrons by screened gold and mercury nuclei", Nuclear Physics **59**, 56–64 (1964).

[62] G. Feinberg, "Polarized electron-nucleus scattering and parity-violating neutral-current interactions", Phys. Rev. D **12**, 3575–3582 (1975).

[63] W. Han, Y. Otani, and S. Maekawa, "Quantum materials for spin and charge conversion", npj Quantum Mater. **3**, 27 (2018).

[64] X. Gu, L. Guo, Y. Qin, et al., "Challenges and Prospects of Molecular Spintronics", Precis. Chem. **2**, 1–13 (2024).

[65] M. Dyakonov and V. Perel, "Current-induced spin orientation of electrons in semiconductors", Phys. Lett. A **35**, 459–460 (1971).

[66] R. J. Elliott, "Theory of the Effect of Spin-Orbit Coupling on Magnetic Resonance in Some Semiconductors", Phys. Rev. **96**, 266–279 (1954).

[67] Y. Yafet, "g Factors and Spin-Lattice Relaxation of Conduction Electrons", in *Solid state physics - advances in research and applications*, Vol. 14 (Academic Press, Jan. 1963), pp. 1–98.

[68] G. L. Bir, A. G. Aronov, and G. E. Pikus, "Spin relaxation of electrons due to scattering by holes", J. Exp. Theor. Phys. **42**, 42 (1976).

[69] G. Fishman and G. Lampel, "Spin relaxation of photoelectrons in p -type gallium arsenide", Phys. Rev. B **16**, 820–831 (1977).

[70] A. G. Aronov, G. E. Pikus, and A. N. Titkov, *Spin relaxation of conduction electrons in p-type III-V compounds*, 1983.

[71] G. Pikus and A. Titkov, "Spin Relaxation under Optical Orientation in Semiconductors", in *Modern problems in condensed matter sciences*, Vol. 8 (1984) Chap. 3, pp. 73–131.

[72] K. Aulenbacher, J. Schuler, D. v. Harrach, et al., "Pulse response of thin III/V semiconductor photocathodes", Journal of Applied Physics **92**, 7536–7543 (2002).

[73] V. Tyukin and K. Aulenbacher, "Polarized Atomic Hydrogen Target at MESA", in Pstp2019 (Sept. 2020), pp. 1–10.

[74] R. Barday, "Untersuchungen zur Lebensdauer von NEA-Photokathoden bei der Extraktion sehr hoher mittlerer Ströme", PhD thesis (Johannes Gutenberg-Universität Mainz, 2007).

[75] I. Alexander, "Experimental investigation of the beam dynamics of the MESA photoinjector", PhD thesis (Johannes Gutenberg-Universität, 2018).

[76] P. Hartmann, "Aufbau einer gepulsten Quelle polarisierter Elektronen", PhD thesis (Johannes Gutenberg-Universität Mainz, 1997).

[77] C. Nachtigall, "Entwicklung eines hochpolarisierten Elektronenstrahls für MAMI unter Ausnutzung der Photoemission von uniaxial deformierten III-V-Halbleitern", PhD thesis (Johannes Gutenberg-Universität Mainz, 1996).

[78] K. Aulenbacher, C. Nachtigall, H. G. Andresen, et al., "The MAMI source of polarized electrons", Nuclear Instruments and Methods in Physics Research, Section A: Accelerators, Spectrometers, Detectors and Associated Equipment **391**, 498–506 (1997).

[79] M. Molitor, "Präzisionspolarimetrie mit Hilfe doppelter Mott-Streuung", PhD thesis (Johannes Gutenberg-Universität Mainz, 2020).

[80] L. Thomas, "I. The kinematics of an electron with an axis", London, Edinburgh Dublin Philos. Mag. J. Sci **3**, 1–22 (1927).

[81] V. Tioukine and K. Aulenbacher, "Operation of the MAMI accelerator with a Wien filter based spin rotation system", Nucl. Instrum. Methods Phys. Res., Sect. A **568**, 537–542 (2006).

[82] E. Riehn, "Photokathoden mit internem DBR–Reflektor als Quellen hochintensiver spinpolarisierter Elektronenstrahlen", PhD thesis (Johannes Gutenberg-Universität, 2011).

[83] D. Thorsten, "Das neue Linearscannersystem zur Strahldiagnose in der 100 keV - Beamline polarisierter Elektronen", Diploma (Johannes Gutenberg-Universität, 1992).

[84] G. D. Fletcher, T. J. Gay, and M. S. Lubell, "New insights into Mott-scattering electron polarimetry", Phys. Rev. A **34**, 911 (1986).

[85] M. Steigerwald, "Polarisationsanalyse des Elektronenstrahls der MAMI - Quelle polarisierter Elektronen mittels Mott - Streuung", PhD thesis (Johannes Gutenberg-Universität, 1997).

[86] R. Bolenz, "Verbesserung der Effizienz eines Mottpolarimeters im Hinblick auf zeitaufgelöste Polarisationsmessungen an Superlattice-Kathoden", Diploma (Johannes Gutenberg-Univeristät, 2005).

[87] SANYO Electric Co, *Laser Diode*, Nov. 2007.

[88] Thorlabs GmbH, *Laser diode L780P010*, Feb. 2010.

[89] K. Aulenbacher, I. Alexander, E. Riehn, and V. Tioukine, "High average photocurrent research at MAMI", in Journal of physics: conference series, Vol. 298 (May 2011), p. 012019.

[90] T. Brecelj, S. J. Paul, T. Kolar, et al. (A1 Collaboration), "Polarization transfer to bound protons measured by quasielastic electron scattering on C 12 ", Phys. Rev. C **101**, 064615 (2020).

[91] L. R. Dalesio, A. Kozubal, and M. R. Kraimer, "EPICS Architecture", in International conference on accelerator and large experimental physics control systems (Nov. 1991).

[92] Thorlabs, *S121C - Standard Photodiode Power Sensor, Si, 400 - 1100 nm, 500 nW - 500 mW*, English, Thorlabs (Feb. 11, 2009).

[93] K.-H. Steffens, "Konzeption und Optimierung eines 100keV-Injektionssystems zur Erzeugung eines longitudinal polarisierten Elektronenstrahls an MAMI", PhD thesis (Johannes Gutenberg-Universtät Mainz, 1993).

[94] P. Denim, *MCPHA: Multi-Channel Pulse Height Analyzer for RedPitaya*, `https://pavel-demin.github.io/red-pitaya-notes/mcpha/`, Accessed: 16.09.2024, 2016.

[95] W. R. Leo, *Techniques for nuclear and particle physics experiments : a how-to approach* (Springer-Verlag, 1987).

[96] V. Fthenakis, D. O. Clark, M. Moalem, et al., "Life - Cycle Nitrogen Trifluoride Emissions from Photovoltaics", Environ. Sci. Technol. **44**, 8750–8757 (2010).

[97] H. Reichardt, A. Frenzel, and K. Schober, "Environmentally friendly wafer production: NF3 remote microwave plasma for chamber cleaning", Microelectron. Eng. **56**, 73–76 (2001).

[98] D. Freedman and P. Diaconis, "On the histogram as a density estimator:L2 theory", Zeitschrift für Wahrscheinlichkeitstheorie und Verwandte Gebiete **57**, 453–476 (1981).

[99] C. Spearman, "The Proof and Measurement of Association between Two Things", Am. J. Psychol. **15**, 72–101 (1904).

[100] J. Cohen, "Statistical Power Analysis", Curr. Dir. Psychol. Sci. **1**, 98–101 (1992).

[101] P. Ripka, "Review of fluxgate sensors", Sens. Actuators, A **33**, 129–141 (1992).

[102] P. Saez, "Polarization and charge limit studies of strained GaAs photocathodes", PhD thesis (Stanford Linear Accelerator Center (SLAC), Mar. 1997).

[103] E. Conwell and V. F. Weisskopf, "Theory of Impurity Scattering in Semiconductors", Phys. Rev. **77**, 388–390 (1950).

[104] M. Erbudak and B. Reihl, "Depolarization of photoelectrons emitted from optically pumped GaAs", Appl. Phys. Lett. **33**, 584–585 (1978).

[105] W. Liu, M. Poelker, X. Peng, S. Zhang, and M. Stutzman, "A comprehensive evaluation of factors that influence the spin polarization of electrons emitted from bulk GaAs photocathodes", J. Appl. Phys. **122**, 035703 (2017).

[106] R. K. Gangwar, A. N. Tripathi, L. Sharma, and R. Srivastava, "Elastic scattering of electrons from Rb, Cs and Fr atoms", J. Phys. B: At., Mol. Opt. Phys. **43**, 085205 (2010).

[107] M. Herbert, T. Eggert, J. Enders, et al., "Cs-O_2-Li as enhanced NEA surface layer with increased lifetime for GaAs photocathodes", (2024).

[108] D. A. Orlov, V. E. Andreev, and A. S. Terekhov, "Elastic and inelastic tunneling of photoelectrons from the dimensional quantization band at a p +-GaAs-(Cs,O) interface into vacuum", JETP Lett. **71**, 151–154 (2000).

[109] J. Maxwell, "Illustrations of the dynamical theory of gases", Philos Mag **19**, 19–32 (1867).

[110] K. I. Park, *Fundamentals of Probability and Stochastic Processes with Applications to Communications* (Springer International Publishing, 2018).

[111] E. Fermi, "Sulla quantizzazione del gas perfetto monoatomico", Rendiconti Lincei **145** (1926).

[112] P. A. M. Dirac, "On the theory of quantum mechanics", Proc. R. Soc. London, Ser. A **112**, 661–677 (1926).

[113] F. Reif, *Fundamentals of statistical and thermal physics* (Waveland Press, 2009).

[114] A. G. Zhuravlev, V. S. Khoroshilov, and V. L. Alperovich, "Electron emission from GaAs(Cs,O): Transition from negative to positive effective affinity", Appl. Surf. Sci. **483**, 895–900 (2019).

[115] D. T. Pierce and F. Meier, "Photoemission of spin-polarized electrons from GaAs", Physical Review B **13**, 5484–5500 (1976).

[116] A. Subashiev, "Manifestations of the electron kinectis in bbr region in polarized electron emission", in Le98 proceedings, edited by Y. Mamev, S. Starovoitov, T. Vorobyeva, and A. Ambrazhei (Sept. 1998), pp. 125–132.

[117] J. Biswas, J. Cen, M. Gaowei, et al., " Revisiting heat treatment and surface activation of GaAs photocathodes: In situ studies using scanning tunneling microscopy and photoelectron spectroscopy ", J. Appl. Phys. **128**, 045308 (2020).

[118] R. Fukuzoe, M. Hirao, D. Yamanaka, et al., "Preparation of Ga-terminated negative electron affinity-GaAs (100) surface by HCl-isopropanol treatment for nanoanalysis by scanning tunneling microscopy", J. Vac. Sci. Technol., B **36**, 06JK01 (2018).

[119] T. Yamada, J. Fujii, and T. Mizoguchi, "STM, STS, and local work function study of Cs/p-GaAs(1 1 0)", Surf. Sci. **479**, 33–42 (2001).

[120] G. F. Knoll, *Radiation detection and measurement*, 3. ed. (Wiley, 2000).

Glossary

Appendix

A.1. Additional data

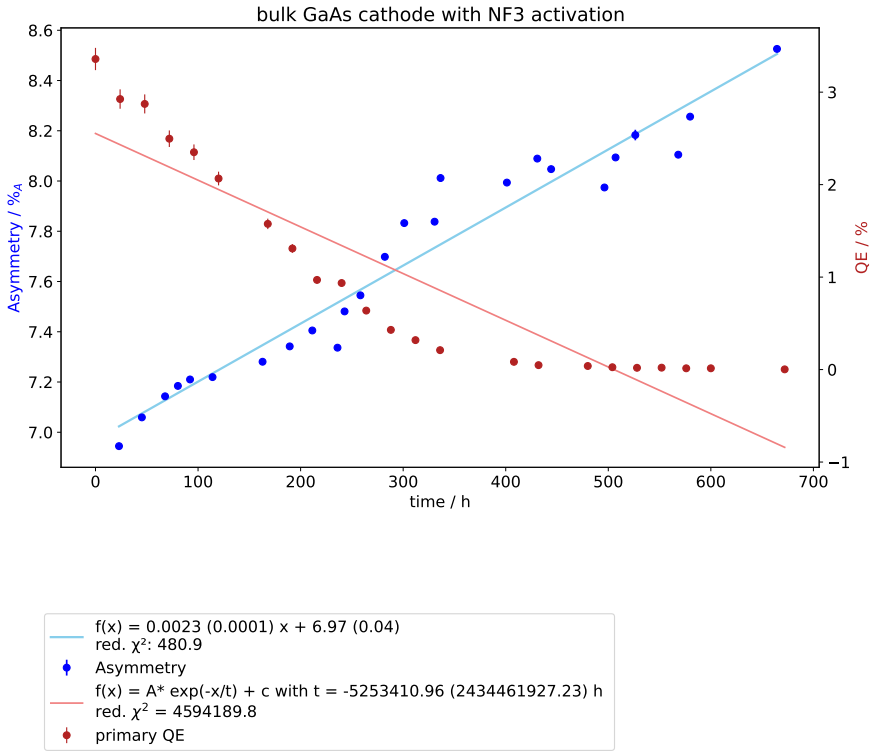

Figure A.1.: *Additional long term run of bulk GaAs with oxygen preparation. Several instabilities during this measurement lead to a stepwise increase of the asymmetries.*

A.2. Detector dead time

With higher currents the possibility for two electrons hitting the detector at once rises and thus make a 200 keV peak. This phenomenon is due to the dead time of the detection system. In fig. A.2 the detectors dead time have been measured. Therefore the count rate was determined at different electron beam currents. A Taylor expansion was used in order to calculate the dead time of the whole detection system.[120]

The dead time of the detecting system is calculated to be $(11.10 \pm 0.33)\,\mu s$. In fig. A.3 a zoom into the low current region is shown. The linearity of the dead time and count rate is signified by an additional linear fit.

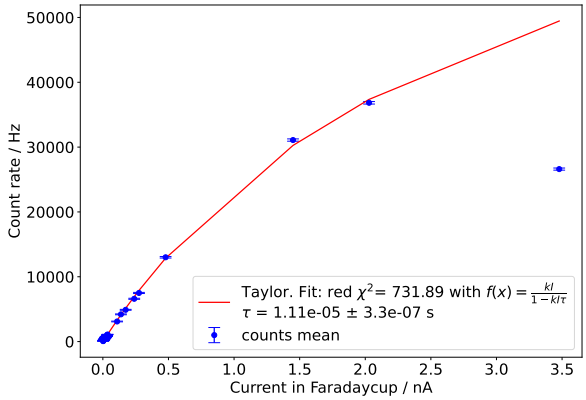

Figure A.2.: *The dead time of the detecting system was obtained through a Taylor expansion.*

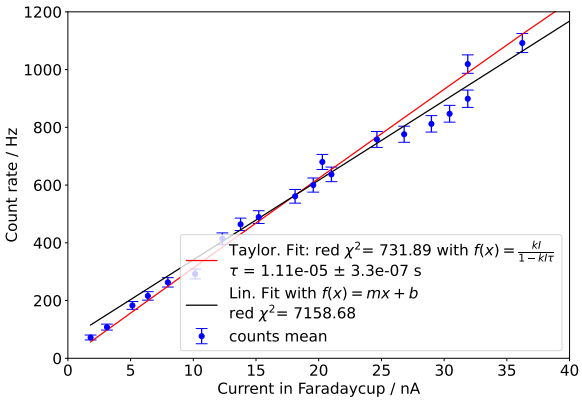

Figure A.3.: *Zoom into the picoampere region. The difference between a linear fit and the Taylor expansion fit is negligible.*

As indicated in section 4.2 in the discussion of the signal to noise ratio (SNR), the detector spectra show no significant signal if no electron beam hits the target. As an example fig. A.4 is shown where 1 nA of beam current are transported to the Faraday cup without any target to interact with.

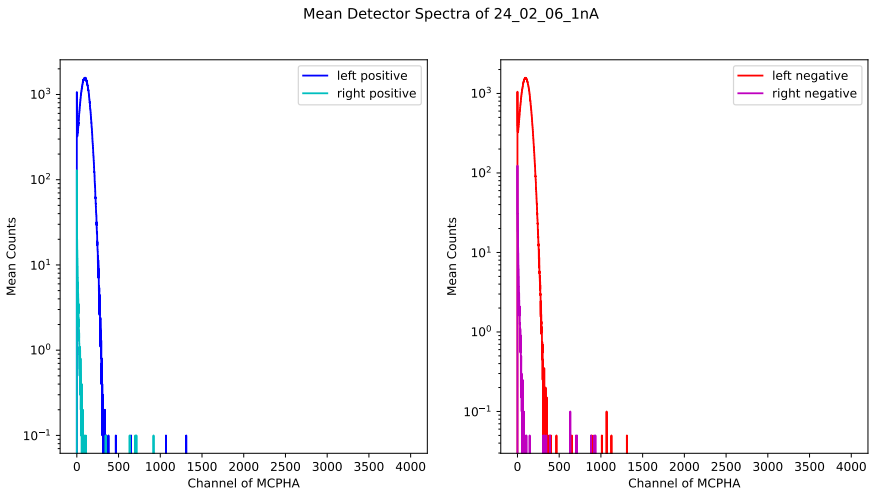

Figure A.4.: *The mean detector spectra of both Pockels cell voltages are shown. All detectors have been measured ten times each for one second and from those ten spectra the arithmetic mean has been calculated. The region of interest for back scattered electrons is between channel number 1000 to 2200.*

Since the electron beam current during Mott measurements is 300 pA the count rates without any targets are zero in the region of interest (channel number 1000 to 2200). This strengthens the argument that the count rate comes solely from the back scattered electrons.

A.3. Integration window dependency of the asymmetry

As discussed in fig. 4.9 for the integration window width the following figures show exemplary different values for the asymmetry in respect to their integration window width. The statistical accuracy for all asymmetry values is in the order of $10^{-5}\,\%_A$ because the test data set contained roughly 18000 measured detector spectra.

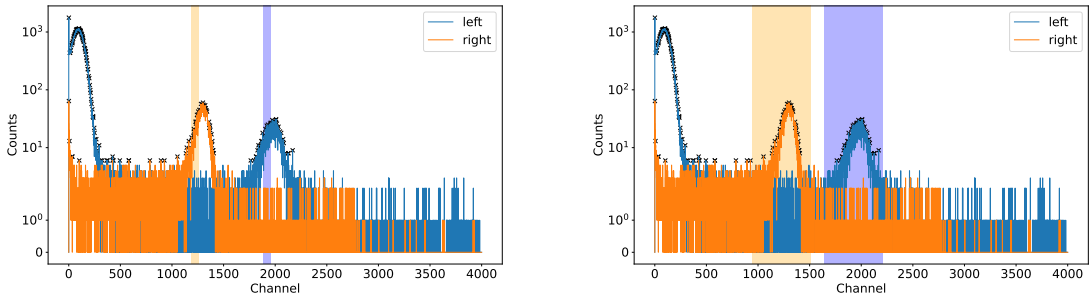

Figure A.5.: *Integration window width of 70 channels, $A = 6.75\,\%_A$ on the left and on the right the integration window width of 570 channels, $A = 6.91\,\%_A$.*

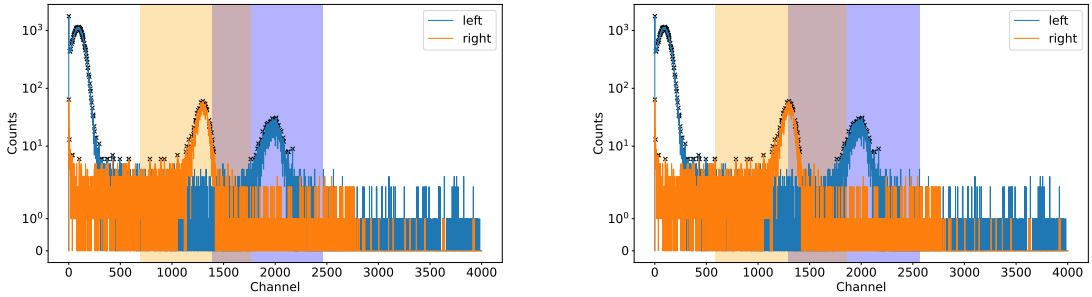

Figure A.6.: *Integration window width of 1070 channels, $A = 7.05\,\%_A$ on the left and on the right the integration window width of 1270 channels, $A = 7.07\,\%_A$.*

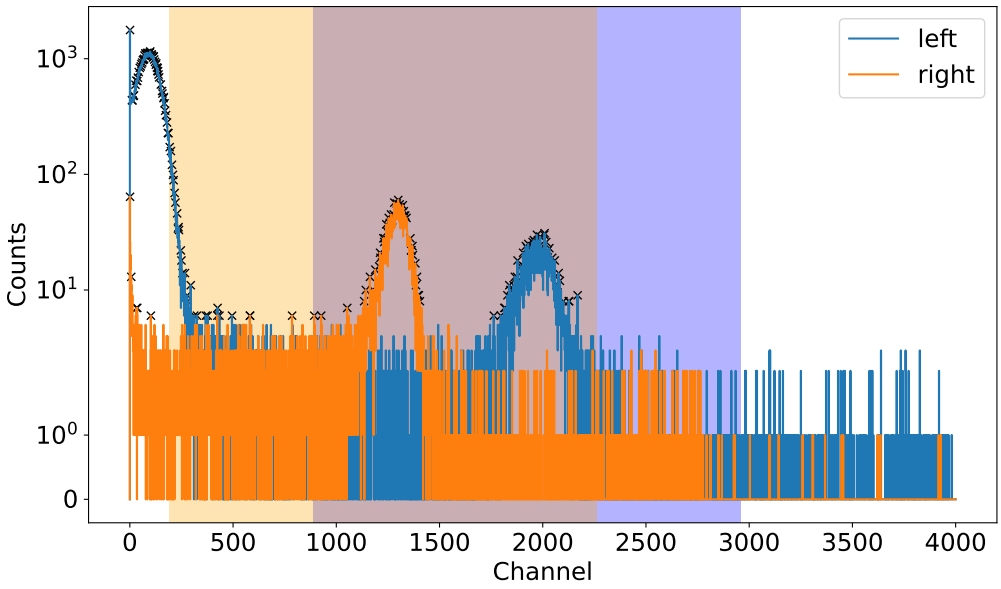

Figure A.7.: *Integration window width of 2070 channels, $A = 7.09\,\%_A$.*